Design and Assembly of Hybrid Nanomaterial Systems for Energy Storage and Conversion

By

Yingwen Cheng

Department of Chemistry
Duke University

Date: ________________________
Approved:

____
Jie Liu, Supervisor

____
Richard A. MacPhail

____
Michael J. Therien

____
Benjamin J. Wiley

Dissertation submitted in partial fulfillment of
the requirements for the degree of Doctor
of Philosophy in the Department of
Chemistry in the Graduate School
of Duke University

2013

ABSTRACT

Design and Assembly of Hybrid Nanomaterial Systems for Energy Storage and Conversion

by

Yingwen Cheng

Department of Chemistry
Duke University

Date: ________________________
Approved:

____
Jie Liu, Supervisor

____
Richard A. MacPhail

____
Michael J. Therien

____
Benjamin J. Wiley

An abstract of a dissertation submitted in partial
fulfillment of the requirements for the degree
of Doctor of Philosophy in the Department of
Chemistry in the Graduate School of
Duke University

2013

Abstract

Energy storage systems are critically important for many areas in modern society including consumer electronics, transportation and renewable energy production. This dissertation summarizes our efforts on improving the performance metrics of energy storage and conversion devices through rational design and fabrication of hybrid nanomaterial systems.

This dissertation is divided into five sections. The first section (chapter 2) describes comparison of graphene and carbon nanotubes (CNTs) on improving the specific capacitance of MnO_2. We show that CNTs provided better performance when used as ultrathin electrodes but they both show similar performance with rapid MnO_2 specific capacitance decrease as electrodes become thicker. We further designed ternary composite electrodes consisting of CNTs, graphene and MnO_2 to improve thick electrode performance (chapter 3). We demonstrate that these electrodes were flexible and mechanically strong, had high electrical conductivity and delivered much higher capacity than electrodes made without CNTs.

Chapter 4 describes assembly of flexible asymmetric supercapacitors using a graphene/MnO_2/CNTs flexible film as the positive electrode and an activated carbon/CNTs flexible film as the negative electrode. The devices were assembled using roll-up approach and can operate safely with 2 V in aqueous electrolytes. The major

advantage of these devices is that they can deliver much higher energy under high power conditions compared with those designed by previous studies, reaching a specific energy of 24 Wh/kg at a power density of 7.8 kW/kg.

Chapter 5 describes our approach to improve the energy and power densities of nickel hydroxides for supercapacitors. This was done by assembling CNTs with Co-Ni hydroxides/graphene nanohybrids as freestanding electrodes. The assembled electrodes have dramatically improved performance metrics under practically relevant mass loading densities (~6 mg/cm^2), reaching a specific capacitance of 2360 F/g at 0.5 A/g and 2030 F/g even at 20 A/g (~86% retention).

Finally, we discuss our efforts on designing highly active electrocatalysts based on winged nanotubes for oxygen reduction reactions (ORR). The winged nanotubes were prepared through controlled oxidization and exfoliation of stacked-cup nanotubes. When doped with nitrogen, they exhibited strong activity toward catalyzing ORR through the four-electron pathway with excellent stability and methanol/carbon monoxide tolerance owning to their unique carbon structure.

Contents

List of Tables

List of Figures

List of Abbreviations

CNTs	carbon nanotubes
1D	one-dimensional
2D	two-dimensional
3D	three-dimensional
MWNTs	multi-walled carbon nanotubes
HRTEM	high resolution transmission electron microscopy
SWNTs	single-walled carbon nanotubes
FWNTs	few-walled carbon nanotubes
fFWNTs	functionalized few-walled carbon nanotubes
CVD	chemical vapor deposition
SEM	scanning electron microscope
TEM	transmission electron microscope
TGA	thermo gravimetric analysis
XRD	X-ray diffraction
XPS	X-ray photoelectron spectroscopy
SC	specific capacitance
EC	electrochemical capacitor
ASC	asymmetric supercapacitor
PTFE	polytetrafluoroethylene

CV	cyclic voltammogram
IR	internal resistance
GO	graphene oxide
RGO	reduced graphene oxide
EES	electrochemical energy storage
EDLC	electric double layer capacitor
ESR	equivalent series resistance
AC	activated carbon
EDS	energy-dispersive X-ray spectroscopy
PVDF	polyvinylidene fluoride
ORR	oxygen reduction reaction
wNT	winged carbon nanotubes

Acknowledgements

First and most importantly, I would like to express my sincere gratitude to my advisor, Prof. Jie Liu. I thank him for everything that he has been devoting to help me grow as a researcher. It is him who brought me to Duke and let me into the field of nanotechnology. Without his inspiration and encouragement, none of the research presented in this dissertation could have been done.

I would like to thank Prof. Richard A. MacPhail, Prof. Michael Therien and Prof. Benjamin Wiley, for their interests in my research and being my committee member, for spending their time reading and commenting my preliminary examination writing, annual research summaries and dissertation and also for their guidance over the years.

I would like to thank all my colleagues at the Liu research group who have given me invaluable assistance during my graduate study, including Prof. Chakrapani Varanasi, Hongbo Zhang, Dr. Ye Hou, Dr. Dongning Yuan, Songtao Lu, Dr. Thomas P. McNicholas, Dr. Sungwoo Yang, Dr. Lei Ding, Dr. Weiwei Zhou, Jay G. Simmons, Jinhyun Cho, Dr. Anmiao Wang, Dr. Xin Lv, Yue Cai, Jinghua, Li, Dr. Pan Li and Gyeong Hee Lee.

I would like to thank some of the participates of the Center of the Environmental Implications of Nanotechnology (CEINT), including Prof. Mark R. Wiesner, Prof. Emily Bernhardt, Dr. Benjamin P. Coleman, Dr. Liyan Yin and Dr. Shihong Lin, for their valuable suggestions and comments to my research.

I would also like to acknowledge Shared Material Instrumentation Facility (SMIF) at Duke for instrumentation assistance. In particular, I want to thank Dr. Mark Walters and Michelle Gignac for their assistance with sample characterization.

I would also like to thank financial support from Duke University through a GPNANO (Graduate Program in Nanoscience) Fellowship.

Finally, I am grateful to my parents and my wife for their limitless love, encouragement, patience and wisdom. They are my strongest support all the time.

Chapter 1: Introduction[*]

1.1 Electrochemical energy storage and conversion: overview

Energy is critically important for many activities in modern society including agriculture, transportation, waste collection and purification, information technology and communication.[1] Currently most of the energy is derived from fossil fuels (~68%): coal (42%), natural gas (21%) and oil (5%). The rest comes from nuclear (14%) and hydro (15%) with the remaining 3% from renewable energies.[2-4] Even with aggressive conservation, the worldwide energy demand is predicted to double by the middle of the century and triple by the end of the century. The increasing uses of fossil fuels, however, have brought a number of serious problems including global warming and environmental pollution that could potentially be risky for the world.[5] At the same time, oil and natural gas production is predicted to peak over the next few decades.[6] The environmental concerns over the use of fossil fuels and their limited resources, together with increasing energy security concerns,[7] have inspired considerable interest in harvesting energy from renewable sources. Solar and wind energies are among the most abundant and readily available. However, they are not constant and reliable sources as they are generally intermittent and geographically limited. The variable nature of these

---

[*] Part of this chapter has been published in Cheng et al. ***Material Research Letters***, 2013, 1-18.

renewable sources cause significant challenges for electric grid operation because other power plants must be used to compensate for the variability. In other words, electrical energy storage systems that store and release energy efficiently are necessary to smooth out the intermittency of renewable energy production.[1] In addition, efficient energy storage systems are also required for developing hybrid, plug-in hybrids and all-electric vehicles.[8] As a matter of fact, energy storage systems are of critical importance for the development of renewable and clean energies both for industrial and residential applications as illustrated in Figure 1.1. Overall, these applications require energy storage systems with desired energy and power characteristics, long cycle life, high efficiency and low cost.[9]

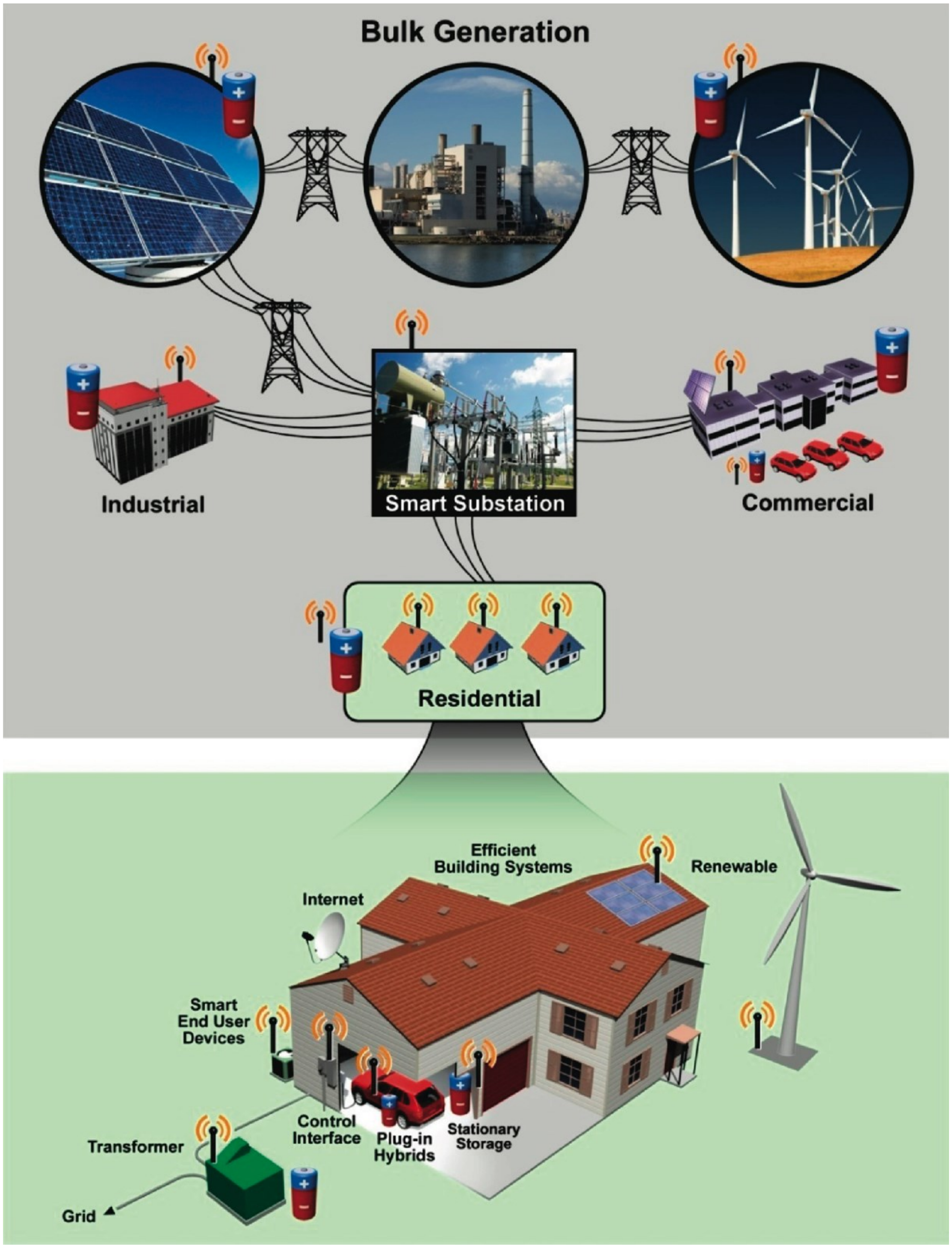

Figure 1.1: Schematic illustration of applications of electrical energy storage for the generation, transportation, distribution and end customers. The graph is adapter from ref. [2]

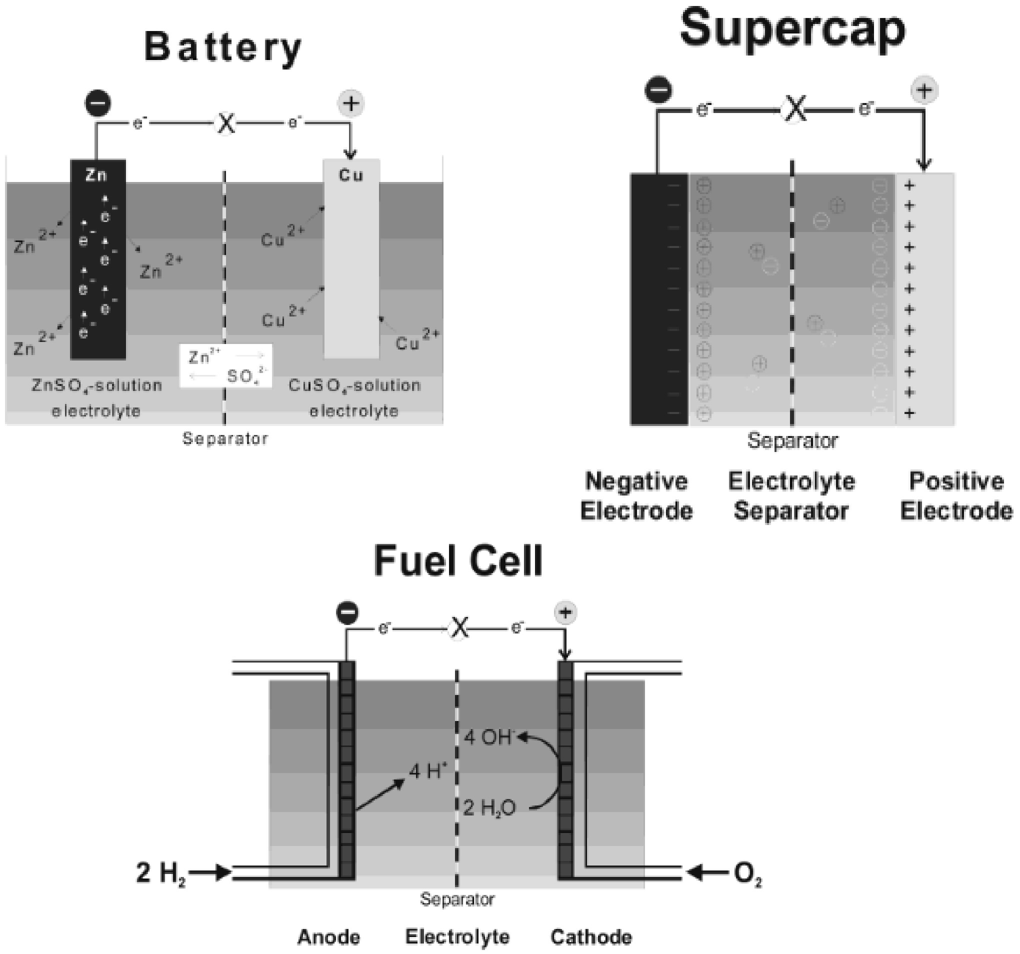

Figure 1.2: Representation of a battery (Daniell cell), an electrochemical supercapacitor that illustrates the energy storage electric double layers at the electrode/electrolyte interface and a fuel cell that shows the follow of reactant and redox reactions in the cell. This figure is adapted from ref. [10]

Electrochemical energy storage (EES) systems are particularly important among all of the energy storage techniques for renewable energy and utility applications. Systems for EES and conversion include batteries, fuel cells and electrochemical capacitors (EC, also known as supercapacitor). Although the operating mechanisms of these devices are different as illustrated in Figure 1.2, they are similar in that energy conversion takes place at the electrode/electrolyte interface and electron and ion transport are separated. In batteries, pseudocapacitors (one type of EC) and fuel cells, electrical energy is stored&released by conversion of chemical energy via redox reactions at the anode and cathode. In electrochemical double layer capacitors (EDLC, another type of EC) energy is stored by a different mechanism, namely through orientation of electrolyte ions at the electrolyte/electrode interface. The ability of these EES systems to store energy can be compared as shown in the Ragone plot (Figure 1.3) on the basis of their energy densities (expressed in watt-hour per kilogram) and power densities (in watts per kilogram). Energy density corresponds to how much energy can be stored while power density corresponds to how fast energy can be delivered, both per unit weight or volume. In principle, they are calculated using the following equations:

$$E = \frac{1}{2} CV^2 \tag{1.1}$$

and

$$P = \frac{E}{t} \tag{1.2}$$

where E, C, V, P and t refer to energy density, specific capacitance, operational voltage, power density and discharge time, respectively. As can be seen in Figure 1.3, EC have orders of magnitude higher power densities than batteries but their energy densities are lower, whereas batteries have much higher energy densities with lower power densities. In general, however, with current technologies neither EC nor batteries alone are able to provide efficient energy storage solutions for transportation, commercial and residential applications.[1] A possible approach to this problem is to develop various types of EES and conversion devices with increased energy and power output characteristics through fundamental studies of their operation principles and rational design of advanced materials with enhanced performances, and the energy requirements could be met through a rational combination of these devices (for example, using EC to provide high power and battery to provide high energy).

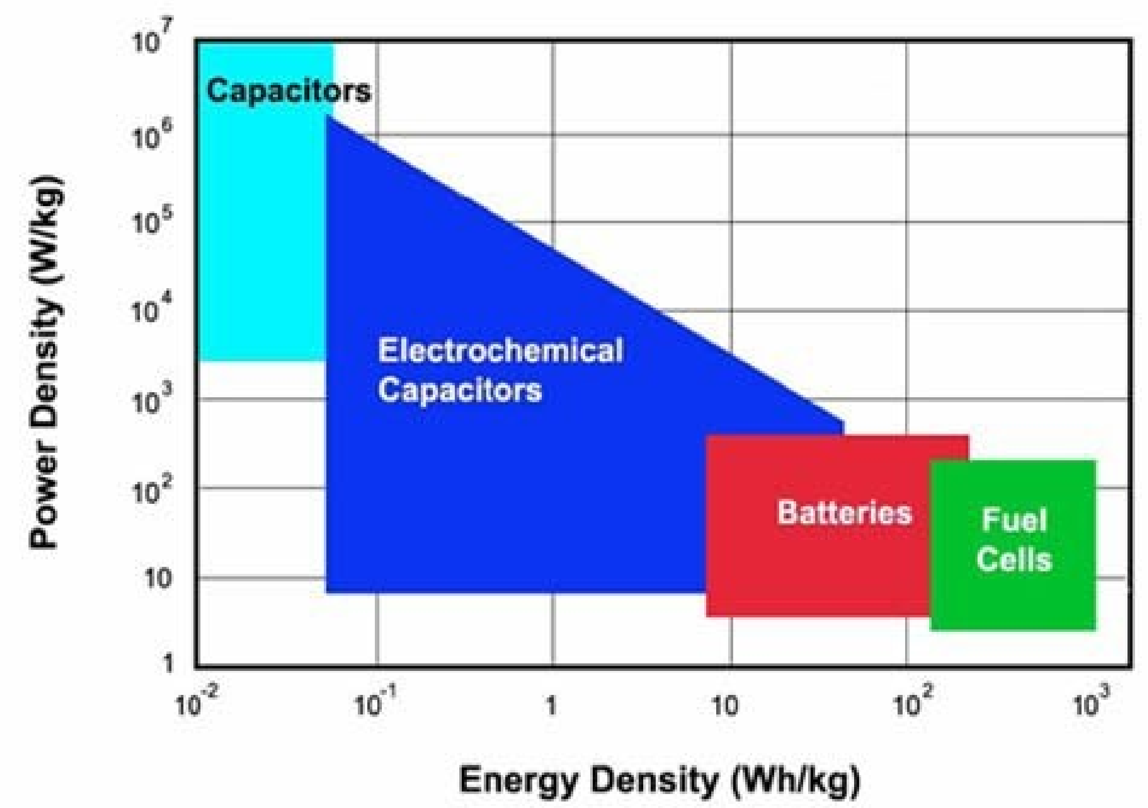

Figure 1.3 Ragone plot that comparing power density against energy density for various electrical energy storage devices. This figure is adapted from ref [11]

1.2 Carbon nanotubes and graphene: structure, synthesis and properties

Carbon nanotubes (CNTs) and graphene are unique types of carbon nanomaterials with many attractive properties including high mechanical strength, high surface area and superior electrical conductivity, which therefore made them very promising for use in advanced energy storage and conversion systems.[12, 13] In this dissertation, they are selected as fundamental building blocks for the design of advanced electrodes. In this section, we aim at providing an introduction of these nanomaterials, with a particular emphasis on their structure, synthesis and properties that are important for energy-related applications.

1.2.1 Carbon nanotubes

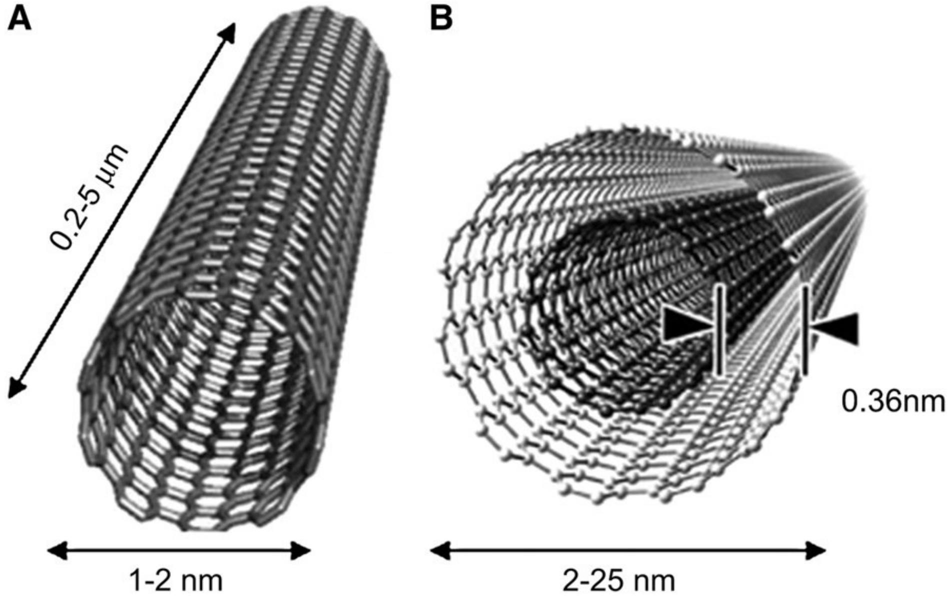

Figure 1.4: Schematic illustration of (A) SWNT and (B) MWNT. Image adapted from ref. [14]

CNTs are allotropes of carbon with a hollow interior and cylindrical structure. They were first discovered by Iijima in 1991 and have significantly advanced the science and engineering of carbon materials since then.[15] CNTs are typically one to several nanometers in diameter and tens of microns in length. In terms of physical structure, CNTs can be visualized by imagining a sheet of graphite that has been rolled into a tube. Depending on the number of graphene layer, they can be classified as singled walled CNTs (SWNTs) and multi-walled CNTs (MWNTs) and their structures are illustrated in Figure 1.4.[16] Owning to the unique arrangement of carbon atoms, CNTs have outstanding structural, mechanical and electronic properties.[17-19] In particular, it was found that CNTs have mechanical strength of up to ~100 GPa [20], making them one of the stiffest and strongest materials. Electrically, CNTs are capable of ballistic transport of electrons and can carry very high current densities ($4\text{x}10^9$ A/cm).[21] CNTs are also very stable at high temperatures and have very high thermal conductivities (~ 3500 W/m·K).[22] In fact, beyond being the best and most easily available 1D system, CNTs have strong potential for use in electronics, scanning probing microscopy, chemical and biological sensing, reinforced composite materials, and in many more areas.

1.2.1.1 Carbon nanotubes synthesis

Depending on the method of production, CNTs can have different diameter, chirality, length, and quality, and therefore properties. Over the past decades, many synthetic methods have been developed to obtain desired CNTs for various scientific and technological applications. Arc discharge[23], laser ablation[24] and chemical vapor deposition (CVD)[25] are the three major methods. Several other methods, including flame synthesis[26], plasma-enhanced CVD[27] and hydrothermal method are also sometimes used.

Arc discharge and laser ablation methods have the advantage of synthesizing CNTs with very high degree of graphitic perfection. Both methods involve condensation of gaseous carbon generated by the evaporation of solid carbon precursors.[28] With both methods, however, only powdered samples with CNTs tangled into bundles can be formed and these bundles are difficult to individualize for practical applications owning to the strong van der Walls interaction between individual nanotubes. Additionally, the expensive equipment cost and high power consumption make these methods less favorable for nanotube productions.

The CVD method is probably the most widely used for the production of nanotubes nowadays. In this method, metallic nanoparticles are used to catalyze decomposition of a carbon compound and initiate growth of CNTs by working as nucleation sites. Synthesis of many forms of CNTs, including MWNTs and SWNTs, have been well developed using CVD. One important advantage of CVD methods is that they allow better control over the morphology, structure and quality of the synthesized CNTs. Besides, with CVD method one can produce well-separated tubes either supported on flat substrate (surface growth) or on powdered catalysts (bulk growth) that can be readily processed for various applications.

1.2.1.2 Carbon nanotube purification and functionalization

The raw CNTs products, when prepared using methods described above, usually contain amorphous carbon, catalysts, catalyst supports, carbon nanoparticles and undesired CNTs as impurities. Consequently, an effective purification of the nanotubes is required before their processing for applications. During decades of research, many methods have been developed toward efficient purification of raw CNT produces. In general, these methods can be divided into two types: dry method and wet method.[29]

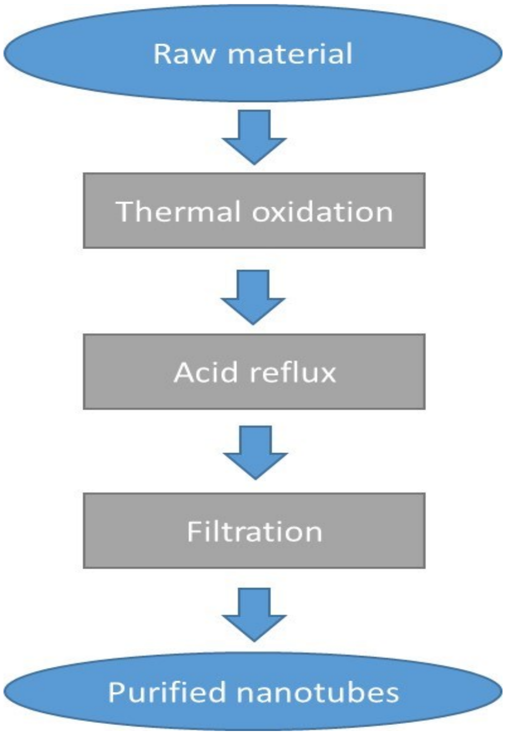

Figure 1.5: Typical purification steps for CNTs

The dry method refers to purification of nanotubes through gas-phase oxidation to selectively remove amorphous carbon species due to their higher reactivity compared with CNTs, whereas wet method refers to purification using solution-based processes (such as nitric acid). In dry methods, the oxidizing gas can be either air or a mixture of air and other gases to improve the selectivity. In operation, usually the dry purification is followed by a wet step as illustrated in Figure 1.5. In the first step, the amorphous carbon is removed by oxidation upon heating to a controlled temperature in either air or mixture gases. Then the exposed metallic impurities are removed by refluxing in a non-oxidizing acid solution (usually HCl). Finally, purified nanotubes can be collected using a simple vacuum filtration process.

Usually, the as-produced pristine CNTs are in the form of agglomerated bundles and these bundles are not soluble in most solvents. To make nanotubes more dispersible, it is necessary to physically or chemically modify their external surface through functionalization. This is an important step for processing CNTs and could significantly extend their application spectrum since functionalization, particularly covalent modification schemes, allows alternation of the electronic properties of CNTs and/or chemically tailor the surface properties of CNTs, whereby new functions can be implemented that cannot otherwise be acquired by pristine nanotubes.

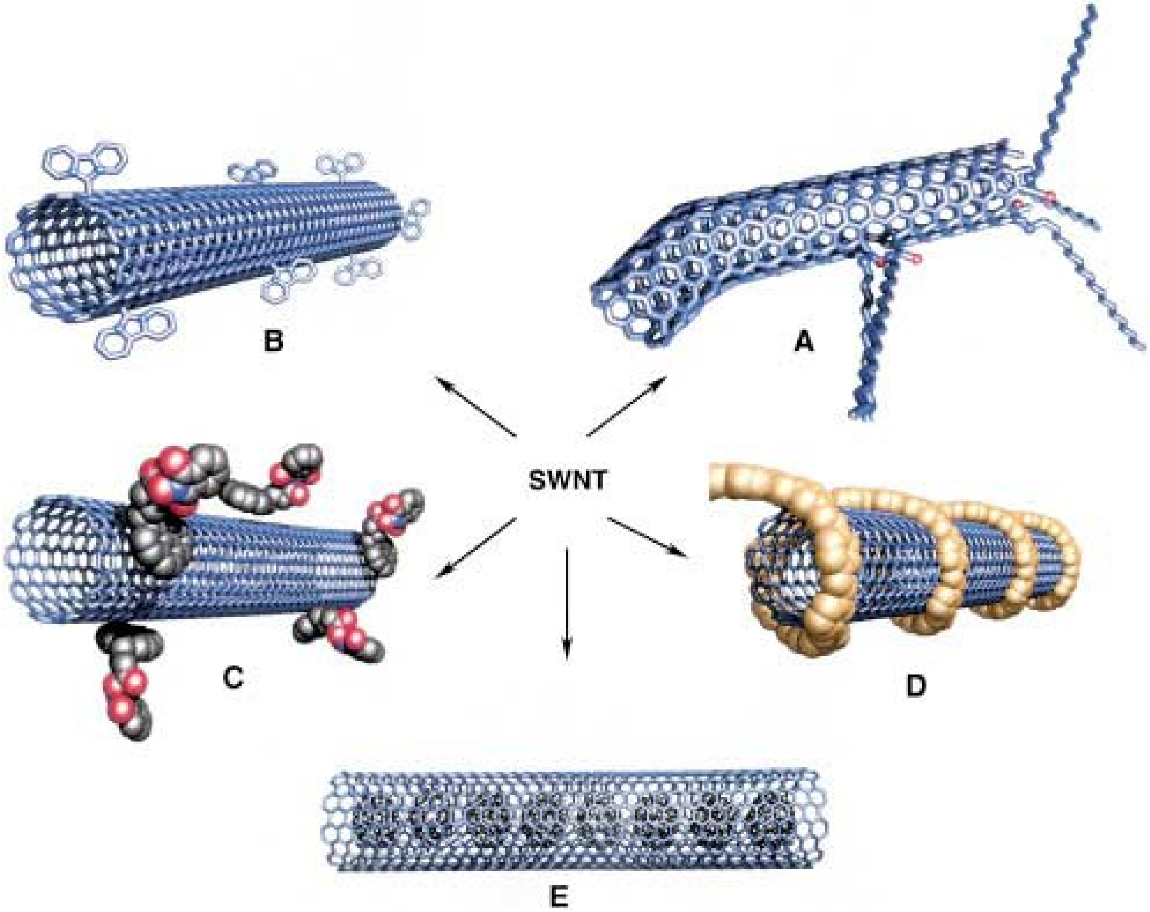

Figure 1.6: Methods for carbon nanotube functionalization: (A) defective group functionalization B): covalent sidewall functionalization; C) non-covalent exohedral functionalization with surfactants; D) noncovalent functionalization with polymers; E): endohedral functionalization, as shown in the picture using C60 for example. This figure is shown using SWNT as an example but the overall idea is similar for other types of nanotubes.[30]

Several approaches have been developed in recent years to functionalize CNTs and they are summarized in Figure 1.6. Usually, CNTs are functionalized by a harsh oxidation process, such as refluxing in the mixed acids of HNO_3 and H_2SO_4, to generate defects on their sidewalls and tips. These defects can serve as anchor groups for functionalization as shown in Figure 1.6 A and B. However, such methods reduce the electrical conductivity and corrosion resistance of CNTs due to damage of graphitic structure. Alternatively, CNTs can be functionalized through noncovalent methods through adsorption or wrapping of various functional surfactants or polymers on their external surfaces (Figure 1.6 C and D).This latter method can preserve the integrity and electronic structure of nanotubes and afford nanotube suspensions with remarkable stability.

1.2.2 Graphene

Graphene is a one-atomic thick layer of graphite comprising sp^2 carbon with delocalized π-electrons. It has very large theoretical specific surface area (2630 m^2 g^{-1}), high intrinsic mobility (200 000 $cm^2v^{-1}s^{-1}$), high Young's modulus (1.0 TPa) and remarkable thermal conductivity (~5000 W $m^{-1}K^{-1}$).[31] Due to these unique properties, graphene is speculated to have remarkable applications that will out-perform CNTs, graphite, metals and semiconductors by working either as an individual material or as substrate toward composite materials.

There are several ways to prepare graphene with either a single or a few layers. The first method reported is through mechanical exfoliation of highly oriented pyrolitic graphite (HOPG) using Scotch tape. Graphene prepared using this method has high structural perfection and electrical conductance and therefore is suitable for fundamental scientific research. However, it suffers from low yields and consequently is not suitable for large scale productions. A second method is epitaxial growth of graphene on SiC or metallic single crystal substrate at high temperature and in ultrahigh vacuum. Graphene synthesized using this method can be large in size and very high in quality, but the manufacturing process requires high vacuum and the facilities are prohibitively expensive. Similar to the mechanical exfoliation method, this method also suffers from the low yield problem. A third method is CVD from catalytic decomposition of hydrocarbons at high temperature on metallic or metal oxide substrates. This method allows for fast, uniform, large area and high quality graphene production and therefore has been under intense research during the past years.

The most frequently used process to prepare graphene for large scale applications, such as energy storage, is through chemical conversion of graphene oxide (GO) because this method allows large quantities of graphene-like material to be produced with high yield and low cost. In this method, GO is first prepared through exfoliation of oxidized graphite and afterwards chemically converted into reduced graphene oxide (RGO) through a reducing process that is able to remove oxygen functionalities and restore their electrical conductivity. In contrast to the other two methods, this method produces a large amount of graphene homogeneously suspended in a solvent and therefore can be readily used for synthesizing graphene hybrid materials with well controlled morphology, structure and properties through numerous solution-phase reactions. The major steps involved in this method for the synthesis of graphene are oxidation, intercalation, exfoliation and/or reduction as illustrated in Figure 1.7.

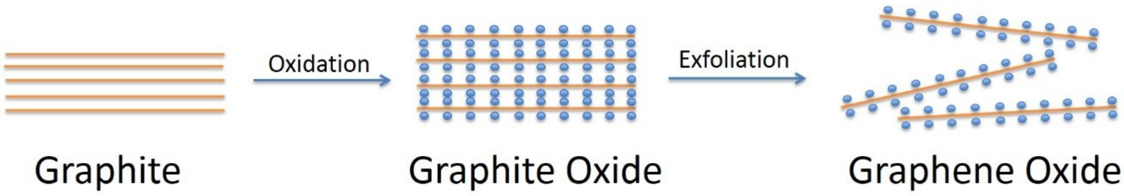

Figure 1.7: Schematic illustration of the processes for the synthesis of GO.

In general, GO can be synthesized using either the Brodie, Staudenmaier or Hummer method or their variations.[32] All these methods involve oxidization of graphite using different oxidizing reagents. The Brodie and Staudenmaier methods both use nitric acid (usually fuming) and potassium chlorate. Nitric acid is very reactive with aromatic carbon surfaces and the reaction leads to liberation of gaseous NO_2 and/or N_2O_4. Likewise, potassium chlorate is also a strong oxidizing agent. The Hummers method uses a combination of potassium permanganate and concentrated sulfuric acid and is the most widely used method in the production of graphene. In this method, well-stacked graphite is used as the precursor and is first oxidized to graphite oxide. In this step, the oxidization results in an increase of the d-spacing and intercalation between adjacent graphene layers and therefore weekens their interactions. Afterwards, the graphite oxides were exfoliated (mostly using sonication) that leads to their delamination into single layer GO in aqueous solution.

Figure 1.8 shows a structure of GO proposed on the basis of solid-state nuclear magnetic resonance experiments. The oxygen groups make GO highly hydrophilic and readily dispersible in several solvents. The C/O atomic ratio in GO is usually around 10, depending on the oxidation conditions. In Raman spectra, GO shows strong D-band that is indicative of highly defective structure. Single layer GO sheets deposited on a SiO_2 substrate show thicknesses of ~ 1 nm as measured by atomic force microscopy. This thickness is larger than the 0.6~0.8 nm for pristine graphene sheets prepared by mechanical cleavage due to interaction of the functional groups with the SiO_2 substrate.

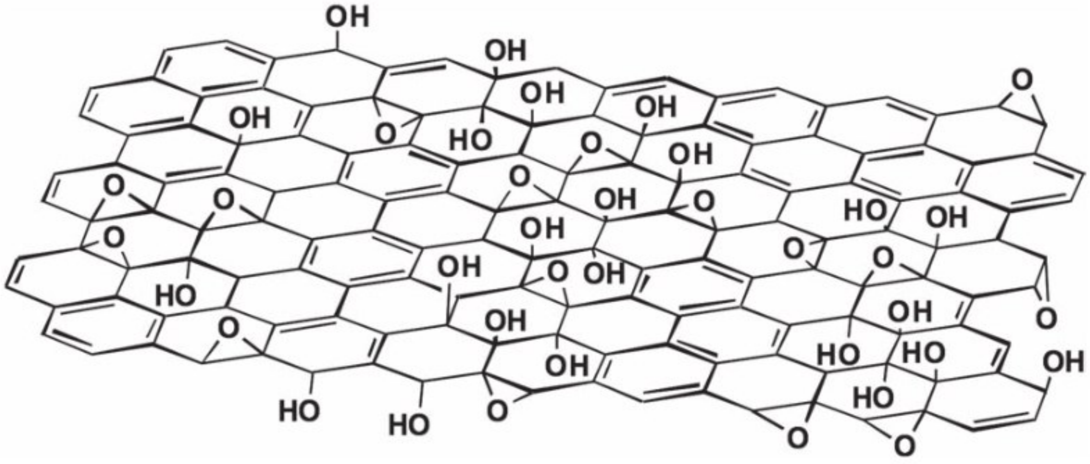

Figure 1.8: A proposed schematic (Lerf-Klinowski model) of GO structure. The figure is adapted from ref. [33]

GO is electrochemically insulating due to disrupted sp^2 bonding networks, and therefore is not well-suited for applications in energy storage and conversions. Consequently, one important reaction of GO is its reduction to recover electrical conductivity by restoring the π-network. The product of this reaction has been called by different names: RGO, chemically derived graphene oxide and graphene. In this dissertation, we use the name of RGO for consistency. The reduction of graphene can be achieved through means of chemical, thermal and electrochemical pathways, all of which lead to products that resemble pristine graphene to varying degrees.

Chemical reduction of GO is the most widely used method by far in the production of RGO. When dispersed in a solvent (typically water), a variety of reducing chemicals can be used to reduce GO and the most commonly used chemical is hydrazine monohydrate. In a typical experiment, hydrazine is added to a GO dispersion and the mixture is heated to evaluated temperatures (typically 80~100^{0}C). During this process the color of the solution changes from brownish (color of GO) to black. After reduction, the C:O ratio is greatly increased to 10.3: 1 from the 2.7:1 for GO.[34] RGO has a much higher conductivity than GO (higher than 100 s cm^{-1} when prepared as bulk films). In addition to chemical reduction, GO can also be reduced by thermal annealing in inert gases such as nitrogen or argon.

1.3 Electrochemical capacitors (EC)

EC are one type of promising energy storage system for the twenty-first century. Currently, EC are widely used in consumer electronics, memory back-up systems and industrial power and energy managements. In particular, EC have promising applications in electric vehicles when combined with primary high-energy density batteries to serve as a temporary energy storage device with high-power capability to store energy when braking and release energy when accelerating. Therefore, for future energy storage systems EC are likely be as important as batteries.

As discussed in section 1.1, the primary advantage of EC is ultra-high power densities. EC also have the advantages of long cycle life (x1000 times higher than batteries), highly efficient (close to 100%) and low maintenance cost. They typically can be discharged in a short period of time (e.g. a few seconds). As such, they are used for power management and are of particular promise for pulse power supply and storage. However, a major drawback of EC is that they have very energy densities compared with other systems. Hence, tremendous research efforts have been devoted to design EC with both high power and high energy densities. In this dissertation, we mainly focus on improving the performance of EC, and in this section we aim at introducing types of EC, materials, as well as reviewing common approaches toward the fabrication of high performance electrodes.

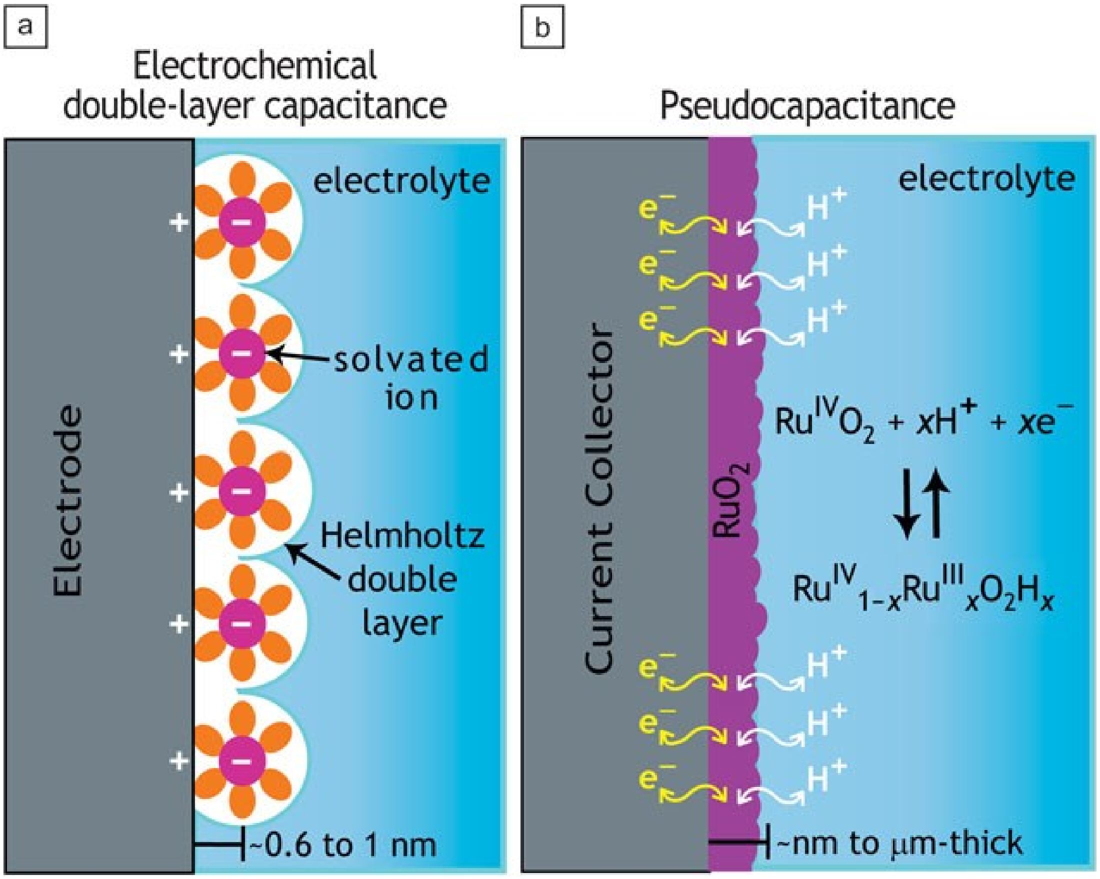

Figure 1.9: Schematic of charge storage via (a) electrochemical double layer capacitance or (b) pseudocapacitance, adapted from ref.[35]

On the basis of their energy storage mechanisms, EC can be classified as electrochemical double layer capacitor (EDLC) and pseudocapacitors.[36] In EDLC, energy is stored via pure electrostatic charge accumulation at the interface between electrode and electrolyte, therefore it is strongly dependent on the surface area of the active material that is accessible to the electrolyte ions. In contrast, in pseudocapacitors energy is stored via fast and reversible surface redox reactions (Figure 1.9). These two mechanisms can take place simultaneously depending on the properties of the electrode material.

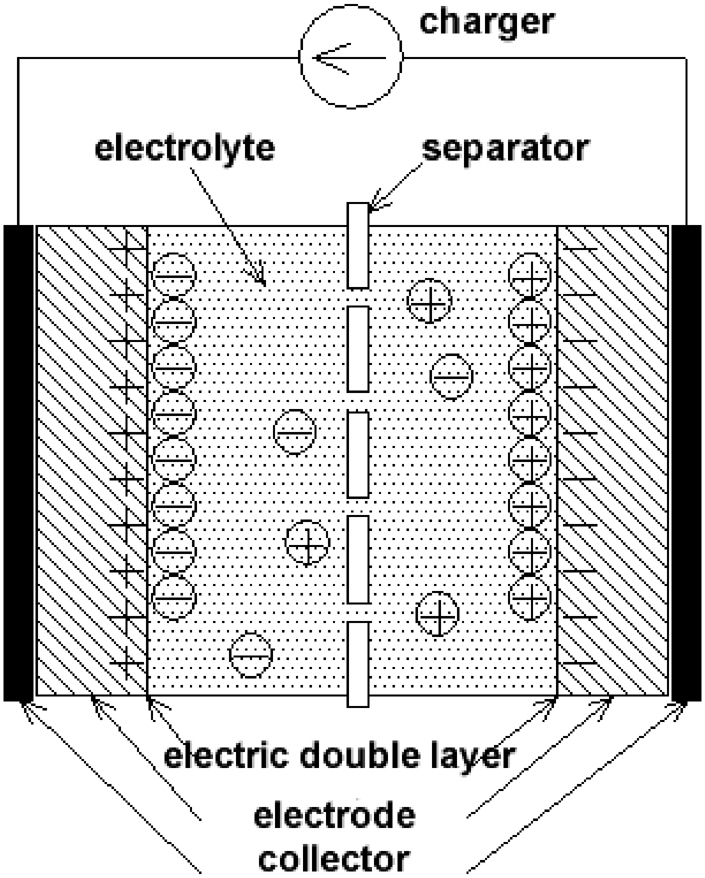

Figure 1.10: Basis structure of a working electrochemical capacitor.

The main components of a single EC include anode, cathode, current collector, separator and electrolyte as illustrated in Figure 1.10. The basic operation of an EC is illustrated in Figure 1.11 in a simple equivalent RC circuit representation. In this figure, C_a and C_c are the capacity of the anode and cathode, R_s is the equivalent series resistance (ESR) of the cell, R_f is the self-discharge resistance of a single electrode. The total capacity of the cell is calculated according to the following equation:

$$\frac{1}{C_T} = \frac{1}{C_a} + \frac{1}{C_c} \qquad (1.3)$$

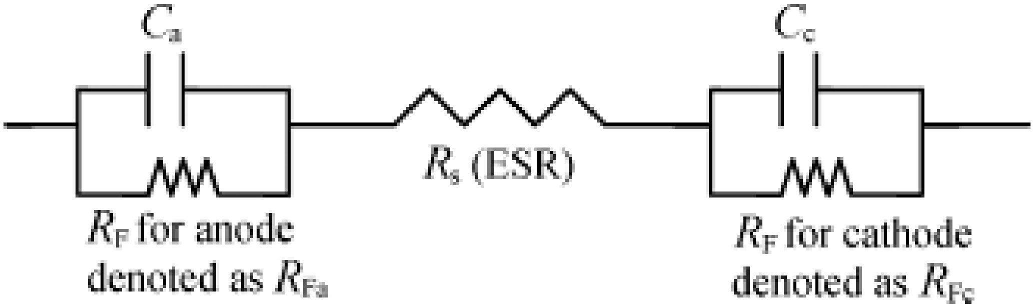

Figure 1.11: A simple RC equivalent circuit representation illustrates the basis operation of a single cell EC. This figure is adapted from ref. [4]

1.3.1 Electrical double layer capacitor (EDLC)

EDLC was invented by the Standard Oil Company of Ohio in 1966.[37] Given the nature of the charge storage process, the amount of charge that can be stored in EDLC depends strongly on the surface area of electrode materials, with effective capacitances in the range of 10~40 μF cm^{-2}.[35] Materials for EDLC are generally carbon nanomaterials with high surface area, including activated carbon,[38] CNTs,[39] graphene[40] and mesoporous carbon because of their desired physical and chemical properties including low cost, variety of forms (powders, fibers, aerogels, monoliths, etc.), ease of processing, relatively inert chemistry and controllable porosity. In developing EDLC with both high power and energy densities, proper control over the specific surface area and pore size distribution of the electrode materials is crucial. In general, activated carbon is most widely used for EDLC because of its high surface area (1000~2000 m^2 g^{-1}) and controllable pore size (to some degree), depending on the method of activation (chemical or physical). However, the power density of AC-based EDLC is low because of the high overall electrical resistance. Therefore, the high specific capacitances (~150 F/g) obtained under low power conditions decrease rapidly as the power density is increased. In recent years, significant progress has been made in EDLC by applying CNTs and graphene as the active materials or supports for active materials. Their combined advantages of high conductivity and reasonably high specific surface area ensure EDLCs with high specific energy and much higher specific power. For example, Niu et al. reported that a MWNT-based supercapacitor electrodes showing a specific capacitance of 102 F/g and a power density of 8 kW/kg.[41] Table 1.1 summarizes some typical experimental results obtained from these materials.

Table 1-1: Properties and characteristics of various carbon materials for supercapacitor, adapted from ref.[4]

			Aqueous electrolyte		Organic electrolyte	
Materials	Specific surface area/$m^2\ g^{-1}$	Density/$g\ cm^{-3}$	/$F\ g^{-1}$	/$F\ cm^{-3}$	/$F\ g^{-1}$	/$F\ cm^{-3}$
Carbon materials						
Commercial activated carbons (ACs)	1000–3500	0.4–0.7	< 200	< 80	< 100	< 50
Particulate carbon from SiC/TiC	1000–2000	0.5–0.7	170–220	< 120	100–120	< 70
Functionalized porous carbons	300–2200	0.5–0.9	150–300	< 180	100–150	< 90
Carbon nanotube (CNT)	120–500	0.6	50–100	< 60	< 60	< 30
Templated porous carbons (TC)	500–3000	0.5–1	120–350	< 200	60–140	< 100
Activated carbon fibers (ACF)	1000–3000	0.3–0.8	120–370	< 150	80–200	< 120
Carbon cloth	2500	0.4	100–200	40–80	60–100	24–40
Carbon aerogels	400–1000	0.5–0.7	100–125	< 80	< 80	< 40

Given the energy storage mechanism of charge separation at the interface between the electrode and electrolyte, EDLC can work both in aqueous and nonaqueous (i.e. organic) electrolytes and therefore its performance can be adjusted by changing the nature of electrolytes. Aqueous electrolytes, such as H_2SO_4 and KOH, generally have lower ESR and lower minimum pore size requirements compared to organic electrolyte. As a result, EDLC generally has higher capacity and power capabilities in aqueous electrolytes (Table

1.1). Additionally, they also have safety and environmental compatibility advantages. EDLC with aqueous electrolytes, however, has a major disadvantage in that its operational voltage is limited to ~ 1.0 V because of the thermodynamic instability of water. As revealed by equation 1.1, the energy that an EC can store is proportional to V^2. As a consequence, EDLC operating in aqueous electrolytes usually has low energy densities. In contrast, nonaqueous electrolytes have a wider stability window (usually > 3.0 V, such as for an acetonitrile-based electrolyte) and thus are able to support EDLC with significantly higher energy densities but their power capability is lower for several reasons including larger ions, lower ionic concentration, and lower mobility as compared to aqueous electrolytes (typical results are shown in Table 1-1).

Significant progress has been made in improving EDLC in recent years owning to the intense research efforts focused at the fundamental and applied level, particularly with regard to new electrode and electrolyte materials.[42] Despite the advancements, the ultimate energy that can be stored in EDLCs is fundamentally limited by the reliance on the double-layer mechanism to store electricity. This necessitates electrode materials with increased specific surface area, but the surface area cannot be increased without limit.

1.3.2 Pseudocapacitors

The limitations of storing energy through EDLC can be resolved by introducing active materials that are capable of storing energy via the pseudocapacitance mechanism (Figure 1.9). The main difference between pseudocapacitance and EDLC is that pseudocapacitance is faradic in origin, involving fast and reversible redox reactions between the electrolyte and active materials at or near the interface of electrode and electrolyte. Such active materials often exhibit broad and symmetric charge-discharge profiles that are similar with the characteristics of EDLC but with significantly higher specific capacitance. The most commonly known active materials are metal oxides[43], metal nitrides[44] and conducting polymers[45], such as RuO_2, Fe_3O_4, NiO and MnO_2 and metal hydroxides include $Ni(OH)_2$ and $Co(OH)_2$.[46] The specific capacitance of these materials exceeds that of carbon materials, justifying the interest in these systems. In addition to the high gravimetric capacitance, the volumetric capacitance is another attractive feature for using metal oxides as their densities are usually much higher than carbon-based materials. While they have very high capacitance, they suffer from the drawbacks of low power densities due to poor electrical conductivity, and lack of stability during cycling.

1.3.2.1 Ruthenium oxide (RuO_2)

Of all the pseudocapacitor materials, ruthenium oxide (RuO_2) is probably the most widely studied due to its intrinsic reversibility for various surface redox couples and high electrical conductivity. Various forms of ruthenium oxides, including rutile RuO_2 and disordered hydrous $RuO_2{\cdot}xH_2O$, exhibit strong pseudocapacitance when cycled in acidic aqueous electrolytes. RuO_2 has three distinct oxidization states accessible within 1.2 V.[47] The charge storage process of RuO_2 involves a series of fast, reversible electron transfer reactions that are coupled with adsorption of protons (equation 1.4)

$$RuO_2 + xH^+ + xe^- \leftrightarrow RuO_{2-x}(OH)_2 \qquad \text{(equation 1.4)}$$

The specific capacitance of RuO_2 for ranges from tens to hundreds of farads per gram (F/g), depending on factors including crystallinity, particle size and electrode architecture. For example, it has been shown that the amorphous hydrous ruthenium oxide exhibited a much higher specific capacitance (720 F/g) than its anhydrous counterpart.[48] Even though RuO_2 has outstanding performance, Ru-based materials are prohibitively expensive for practical considerations and therefore difficult to be produced in large-scales. Hence, considerable research efforts have been prompted to develop less expensive materials that can be used to replace RuO_2.

1.3.2.2 Manganese oxide (MnO_2)

Since the first report about the capacitive behavior of MnO_2 by Lee and Goodenough in 1991,[49] this material stands out as a promising alternative to RuO_2 for several reasons including natural abundance, low toxicity and ability to operate in neutral aqueous electrolytes with high theoretical specific capacitance (~1380 F/g).[50] The increasing worldwide interest in MnO_2 is based on the anticipation that it could serve as a safe and low-cost alternative to the state-of-art commercial organic EDLC and RuO_2-based acidic systems. On the basis of spectroscopic measurements such as X-ray photoelectron spectroscopy and X-ray absorption spectroscopy, MnO_2 stores electricity though redox cycling between MnO_2 and Mn_3O_4, compensated by the reversible insertion of cations and/or protons and with the reaction proposed as follows:

$MnO_2 + X^+ + e^- \leftarrow\rightarrow MnOOX$,

where $X^+ = H^+, Li^+, Na^+$, or K^+. (Equation 1.5)

Manganese oxides have a wide variety of crystal forms, defect chemistry, morphology, porosity and texture and therefore they exhibit a wide diversity of electrochemical properties. Therefore, considerable interest has been devoted to the modification of synthetic conditions and post synthetic procedures to obtain MnO_2 with desirable physical and chemical properties for improved capacitive and power characteristics. Among them, amorphous MnO_2 powders are probably the most widely studied material and the most common method to produce such material is through the chemical co-precipitation method. This is generally done by reacting a Mn (VII) salt (e.g $KMnO_4$) and a Mn(II) salt (e.g. $MnSO_4$) in water with appropriate molar ratio through the following reaction:

$$\text{Mn(VII)} + 3/2\ \text{Mn(II)} \rightarrow 5/2\ MnO_2\ \text{(IV)} \qquad \text{(Equation 1.6)}$$

Alternatively, MnO_2 with similar structures can be prepared by reacting $KMnO_4$ using different reducing agents, such as KBH_4, sodium dithionite, HCl, aniline and ethylene glycol.[51] MnO_2 synthesized by such methods is normally amorphous α-MnO_2 (as shown in Figure 1.12) with nearly 20% water content, and its specific surface area can be as high as 200 $m^2\ g^{-1}$.[52] It was found that this type of MnO_2 powder exhibited excellent capacitive behavior in several neutral alkaline-ions based electrodes such as KCl, NaCl and LiCl.[49] It was also found that the pseudocapacitive performance of such MnO_2

depended significantly on the annealing temperature. With several hundred degrees heat treatment, the hydrous amorphous phase will be dehydrated and convert to crystals (Figure 1.12 and 1.13). As a result, the crystalline grain increases and the specific surface area decreases, both of which eventually lead to decreases in gravimetric capacitance and rate capability.[53]

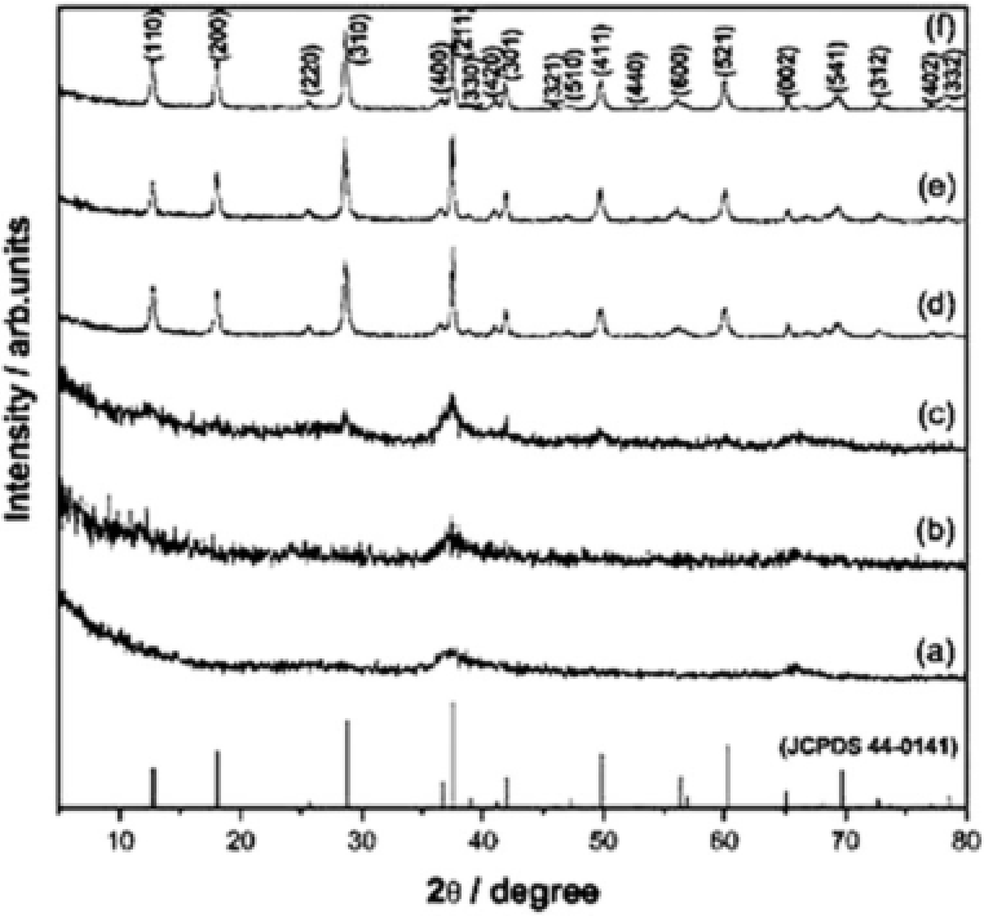

Figure 1.12: XRD pattern of as-prepared and annealed MnO2 samples (a) dried in air and annealed at 50 ^{0}C; (b) 200 ^{0}C; (c) 300 ^{0}C; (d) 400 ^{0}C; (e) 500 ^{0}C and (f) 600 ^{0}C for 3 hours in air. This figure is adapted from ref. [53]

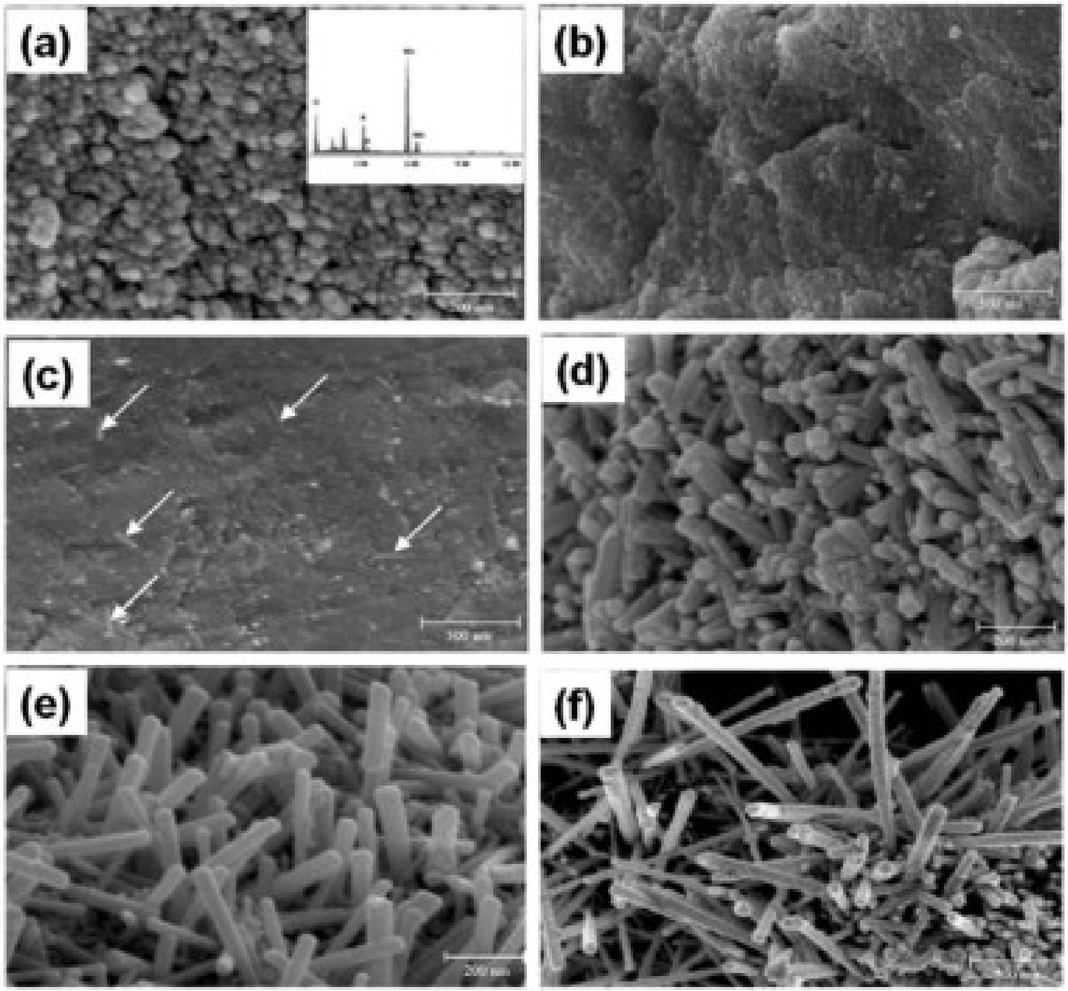

Figure 1.13: SEM image of MnO$_2$ (a) as prepared and dried 50 ^{0}C; (b) 200 ^{0}C; (c) 300 ^{0}C; (d) 400 ^{0}C; (e) 500 ^{0}C and (f) 600 ^{0}C for 3 hours in air. Arrows in (c) indicate initiation of nanorods. This figure is adapted from ref. [53]

Table 1-2: Comparison of the synthesis condition, physicochemical feature, and specific capacitance of MnO_2 under examination.

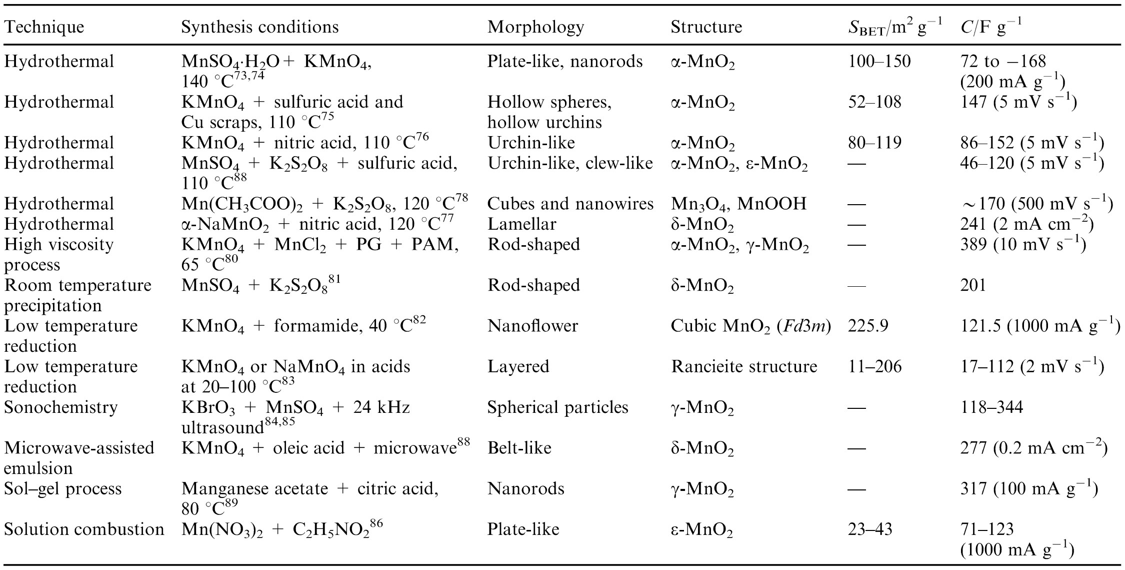

Technique	Synthesis conditions	Morphology	Structure	$S_{BET}/m^2\ g^{-1}$	$C/F\ g^{-1}$
Hydrothermal	$MnSO_4{\cdot}H_2O + KMnO_4$, 140 °C[73,74]	Plate-like, nanorods	α-MnO_2	100–150	72 to −168 (200 mA g^{-1})
Hydrothermal	$KMnO_4$ + sulfuric acid and Cu scraps, 110 °C[75]	Hollow spheres, hollow urchins	α-MnO_2	52–108	147 (5 mV s^{-1})
Hydrothermal	$KMnO_4$ + nitric acid, 110 °C[76]	Urchin-like	α-MnO_2	80–119	86–152 (5 mV s^{-1})
Hydrothermal	$MnSO_4 + K_2S_2O_8$ + sulfuric acid, 110 °C[88]	Urchin-like, clew-like	α-MnO_2, ε-MnO_2	—	46–120 (5 mV s^{-1})
Hydrothermal	$Mn(CH_3COO)_2 + K_2S_2O_8$, 120 °C[78]	Cubes and nanowires	Mn_3O_4, MnOOH	—	~170 (500 mV s^{-1})
Hydrothermal	α-$NaMnO_2$ + nitric acid, 120 °C[77]	Lamellar	δ-MnO_2	—	241 (2 mA cm^{-2})
High viscosity process	$KMnO_4 + MnCl_2$ + PG + PAM, 65 °C[80]	Rod-shaped	α-MnO_2, γ-MnO_2	—	389 (10 mV s^{-1})
Room temperature precipitation	$MnSO_4 + K_2S_2O_8$[81]	Rod-shaped	δ-MnO_2	—	201
Low temperature reduction	$KMnO_4$ + formamide, 40 °C[82]	Nanoflower	Cubic MnO_2 (*Fd3m*)	225.9	121.5 (1000 mA g^{-1})
Low temperature reduction	$KMnO_4$ or $NaMnO_4$ in acids at 20–100 °C[83]	Layered	Rancieite structure	11–206	17–112 (2 mV s^{-1})
Sonochemistry	$KBrO_3 + MnSO_4$ + 24 kHz ultrasound[84,85]	Spherical particles	γ-MnO_2	—	118–344
Microwave-assisted emulsion	$KMnO_4$ + oleic acid + microwave[88]	Belt-like	δ-MnO_2	—	277 (0.2 mA cm^{-2})
Sol–gel process	Manganese acetate + citric acid, 80 °C[89]	Nanorods	γ-MnO_2	—	317 (100 mA g^{-1})
Solution combustion	$Mn(NO_3)_2 + C_2H_5NO_2$[86]	Plate-like	ε-MnO_2	23–43	71–123 (1000 mA g^{-1})

Despite the many methods that have been established to improve the activity of MnO_2, experimentally its specific capacitances have been mostly within 100~200 F/g, much lower than the theoretical capacity and also much lower than for RuO_2 (typical results are shown in table 1.2). This occurs mainly because MnO_2 has very low electrical conductivity (10^{-5} s/cm) that limits the electrode performance when prepared as dense packaged powders. In view of this problem, thin-film electrodes with MnO_2 coating have been intensively explored recently. In these electrodes, a manganese oxide thin layer with desired features is directly fabricated on a current collectors through a variety of techniques, such as sol-gel dip-coating, anodic/catholic electrodeposition, electrophoresis, electrochemical formation of manganese and sputtering-electrochemical oxidization.[51] Figure 1.14 shows a set of typical SEM images of MnO_2 thin films prepared by anodic electrodeposition. When the coatings of MnO_2 were prepared with loading mass lower than tens of μg/cm^2, an anomalously high capacitance more than 1000 F/g (close to the theoretical value) can be obtained. This happens because as nanoscopically thin films, the diffusion distance for the solid-state transport of inserted cations is greatly reduced, overcoming the limitations of the poor electric conductivity of MnO_2. However, such thin film electrodes may only applicable as microsystems for energy storages because the weight of metallic current collectors, such as Al and Ni foil, is typically at a few mg/cm^2. Therefore, the performance metrics of thin-film based devices will be very low because the active material is just a fraction of the weight of the current collectors. In order to be used in large scale industrial applications, electrodes that have both high loading mass and high performance are required for industrial applications. The advantages of high specific capacitance as ultrathin coatings can be translated into 3D electrode architectures in which thin metal oxide coatings are applied to porous and conductive substrates, and this will be discussed in the following sections.

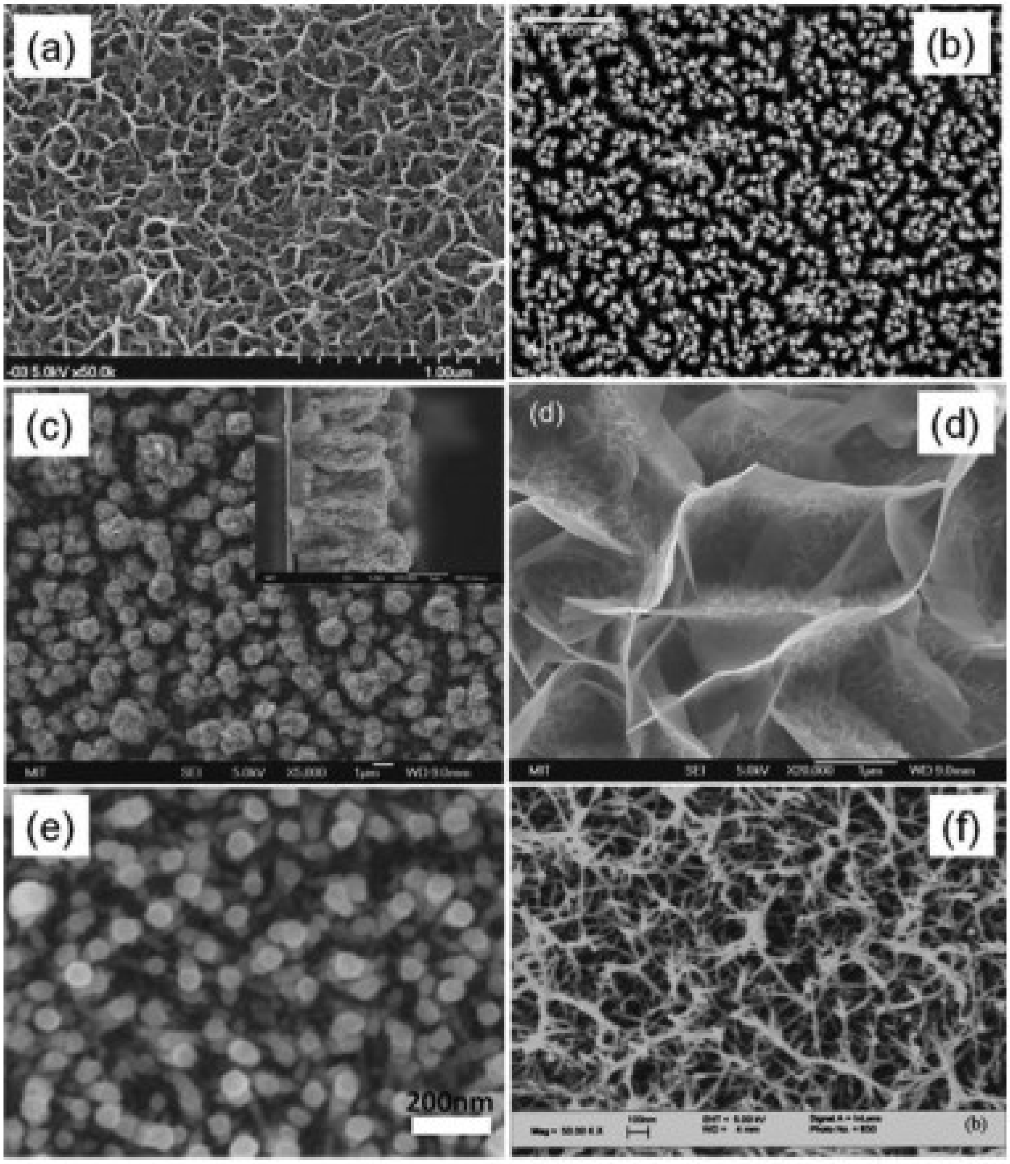

Figure 1.14: Typical surface morphologies for MnO_2 electrodes prepared through template-free anodic electrodeposition process. This figure is adapted from ref. [51]

1.3.2.3 Nickel oxides and hydroxides

Nickel oxide and hydroxide represent as another type of promising electrode materials in pseudocapacitors. They are low cost materials, have high specific capacitance in principle (theoretically: 3750 F/g) and can be synthesized relatively easily. In alkaline electrolytes, they store electricity through the following reaction:

$$NiO + OH^- \leftrightarrow NiOOH^- + e^- \qquad \text{(equation 1.7)}$$

Similar to other metal oxides, the reactivity of NiO also depends significantly on its porosity, structure and crystallinity. For example, a specific capacitance of 167 F/g was obtained for NiO with cubic structure, whereas porous NiO prepared by a sol-gel process exhibited 200~250 F/g. Significant improvements were obtained when NiO was annealed and its specific capacitance reached 696 F/g after annealing at 250^0C.[54] There are many challenges for NiO to be used for EC. Firstly, NiO usually has poor cyclic stability due to degradation during repeated charge-discharge cycles. Secondly, NiO also has very poor electrical conductivity and this results in a dramatically reduced specific capacitance when the current density increases. To resolve this problem, much work has been done on nanostructured NiO with various morphologies and structures including nanocolumns, nanosheets, nanoflakes, porous nanowall arrays and hollow nanospheres. A high specific capacitance of 770 F/g was obtained for flowerlike NiO hollow nanospheres at 2 A/g with improved cycling stability.[55]

1.3.2.4 Conducting polymers

Conducting polymers are unique types of pseudocapacitive materials. The capacitance of these materials originates from the fast and reversible oxidation and reduction processes related to the π-conjugated polymer chains.[56] Many types of conducting polymers have been studied for EC and they are typically synthesized through chemical or electrochemical oxidation of the monomer. These polymers include polyaniline, polypyrrole, polythiophene and their derivatives. Many studies have documented that these π-conjugated polymers derived from various heterocyclic organic compounds have high gravimetric and volumetric pseudocapacitance in various nonaqueous electrolytes with operating voltage of ~ 3V.[45] However, when used as bulk electrodes, conducting polymers suffer from limited cycle stability and capacitance gradually decrease over cycles.

Figure 1.15 compares the specific capacitance obtained experimentally for typical EC materials both for EDLC and pseudocapacitor. As can be seen, the specific capacitances of pseudocapacitive materials were generally higher than EDLC materials.

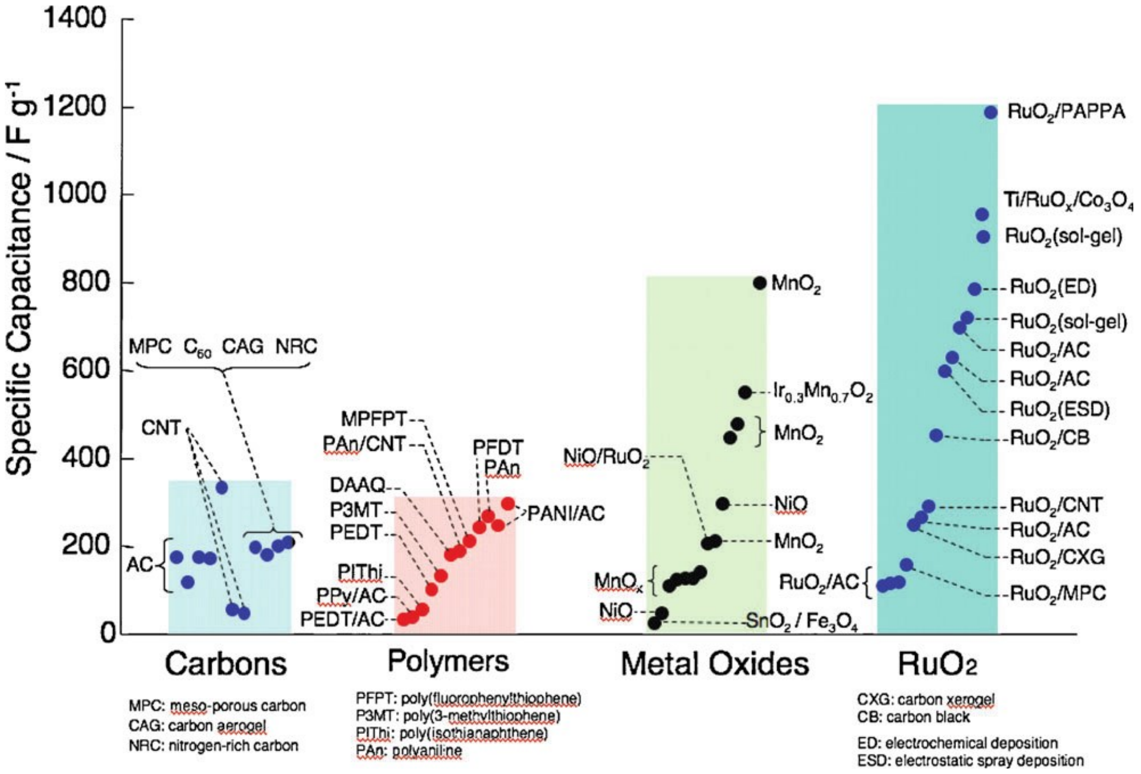

Figure 1.15: Comparison of the specific capacitance values reported in the literature for various materials under study for EC. Adapted from ref. [57]

1.4 Carbon nanomaterial/metal oxide composites for EC

Metal oxides and hydroxides are promising materials for batteries and EC because of their high specific capacities, typically 2~3 times higher than carbon/graphite based materials. However, the cycling stability and high-rate performance of these materials still cannot meet the requirements of practical applications. Therefore, it is still necessary to design strategies to improve their overall performances. In this section we will discuss the design, fabrication and testing of composite materials composing of carbon nanomaterials and metal oxides/hydroxides. The use of nanostructured hybrid electrode materials represents a promising strategy toward high performance energy storage devices that brings several advantages. First, with rationally designed composite materials, the unique merits of each materials can be integrated and enable electrodes that combined the advantages of large electrochemically active surface area, faster electronic/ionic transportation and improved mechanical stability. Second, a hybrid design, such as the core-shell structure, can effectively reduce the surface energy of active materials and therefore improve their stability during repeated charge-discharge cycles, and at the same time, avoid the aggregation of active materials. Finally, with rationally designed architectures the metal oxide based electrodes can be engineered to be binder-free flexible films and this represent as an exciting approach for high and fast energy storage.

1.4.1 Carbon/MnO_2 hybrid

Hybrid materials consisting of MnO_2 and various carbon nanomaterials (such as carbon aerogels, CNTs, graphene) were actively explored in recent years by researchers worldwide for EC and much higher capacities than pure MnO_2 were successfully demonstrated in this works. Taking CNTs for example, the composite MnO_2/CNTs can be synthesized using a simple chemical co-precipitation method as described above (section 1.3.2). In this process, it was found that functionalization of nanotubes played a critical role toward making uniform metal oxide coatings as this process increases the hydrophilicity of CNTs. The incorporation of mechanically strong and highly conductive nanotubes substantially improved the specific capacitance and rate capacity of MnO_2 as shown in Figure 1.16.[58] A third component can be added in order to further increase performance. In our previous work,[58] we designed a ternary hybrid materials composed of MnO_2, CNTs and conducting polymers (PEDOT-PSS). In this structure, PEDOT-PSS could function as an effective dispersant and interconnect the MnO_2/CNT composites. The overall conductivity of the electrodes was significantly improved since the polymer is conductive. Working together, a high specific capacitance of 427 F/g was obtained.

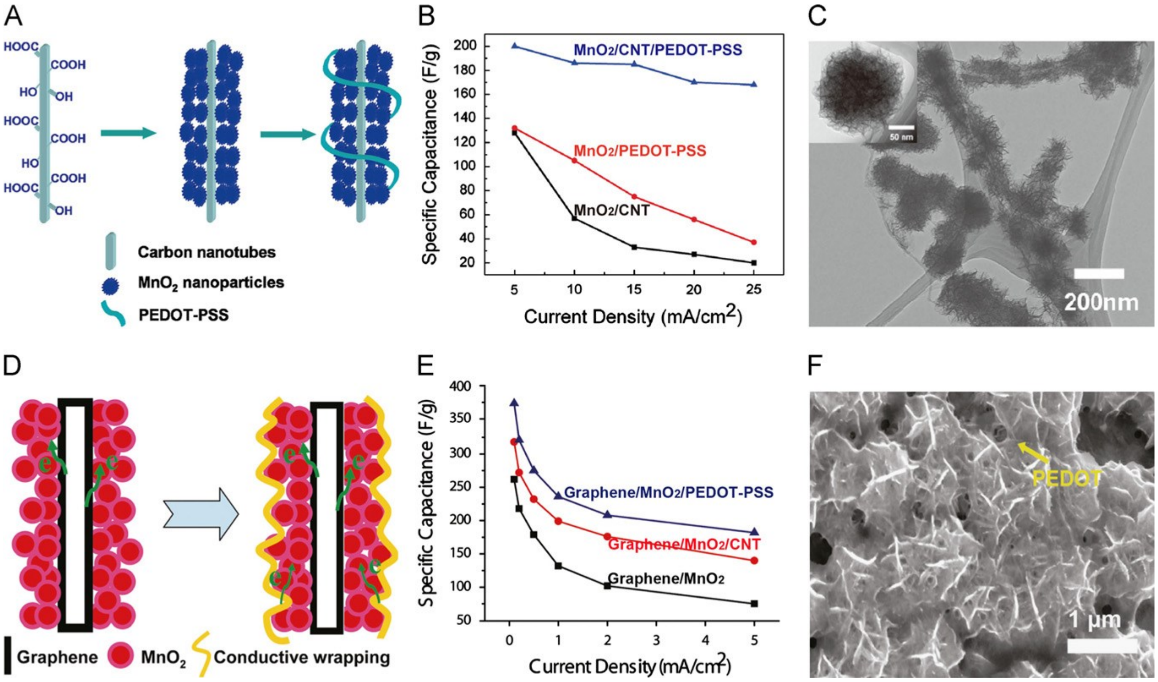

Figure 1.16: (A) schematic of MnO_2/CNTs/PEDOT-PSS ternary composite material; (B) specific capacitance of MnO_2/CNTs/PEDOT-PSS(blue), MnO_2/PEDOT-PSS (red), and MnO_2 film (black) at different charge/discharge current densities, (C) TEM of nanospheres in situ grown on CNTs. (D) Schematic illustration showing the conductive wrapping of graphene/MnO_2(GM) to introduce an additional electron transport path, (E) Summary plot of specific capacitance values for three different electrode systems:

GM-, GMC-, and GMP-based textiles at various current densities. (F) Typical SEM image showing graphene/MnO_2/PEDOT-PSS nanostructures (GMP).

Electrochemical deposition of MnO_2 on carbon networks is one of the most widely used approaches to prepare hybrid carbon/MnO_2 materials for EC.[59] The thickness and structure of deposited MnO_2 can be readily controlled by tuning the deposition voltage and current, and the electrolyte and properties of the carbon substrate have significant influences over their energy storage performance.[60, 61] Kang et al. deposited MnO_2 onto CNTs coated printer paper and found that the specific capacitance of such electrodes was able to reach 540 F/g at 2 mV/s.[62] However, the active MnO_2 loading was only 0.38 mg/cm^2 and therefore the electrode-level performance metrics, when considering its total weight, was actually quite poor. Therefore, highly conductive and porous substrates are desired for depositing MnO_2 with higher mass densities. In this case, cotton textiles and polyester fabrics coated with CNTs or graphene are excellent choices (Figure 1.16).[63-66] The macroporous nature of these substrates making them capable of loading much more MnO_2 and densities up to ~8 mg/cm^2 was successfully demonstrated using CNTs coated textiles.[64] Using these substrates, a high capacitance of 410 F/g was obtained when the MnO_2 loading was 0.06 mg/cm^2. Even though the gravimetric capacitance of MnO_2 was decreased along with the increase of MnO_2 loading ($<$ 100 F/g when MnO_2 loadings were $>$ 1 mg/cm^2), the areal capacitance increased and reached 2.8 F/cm^2 when 8.3 mg/cm^2 MnO_2 was used.[64] Using a similar approach, CNTs coated sponges were examined as the flexible substrate for depositing MnO_2. [63] Experimental results demonstrated that the lightweight and highly absorbing sponges were able to load MnO_2 as high as 12.8 mg/cm^2. High specific capacitances of ~ 1000 F/g were obtained when MnO_2 loading was less than 0.1 mg/cm^2. As the density of MnO_2 was increased, its specific capacitance also decreased to ~ 200 F/g. The MnO_2-CNT-sponge EC show only 4% degradation after 1000 cycles at charge-discharge specific current of 5 A/g and their specific power and energy are high with values of 64 kW/kg and 31 Wh/kg, respectively. Following these studies, a 3D conductive wrapping strategy using CNTs ink or conducting polymers was developed to further increase the performance of MnO_2/graphene/textile electrodes (Figure 1.16). Specific capacitances of the flexible electrodes were substantially increased by ~20% and ~45% after wrapping with CNTs and conducting polymers, respectively, with values as high as ~ 380 F/g achieved. Moreover, the wrapped electrodes also exhibited remarkable cyclic stability with >95% retention over 3000 cycles.[67] These results demonstrated that the conductive coating approach is a promising approach for enhancing the device performance of metal oxide based electrochemical capacitors and can be generalized for designing next-generation high performance flexible energy storage devices.

Also using the electrodeposition method, many other substrates were also used to fabricate MnO_2-based hybrid electrodes. Some typical examples are as follows (as well as in Table 1-3): carbon cloth (MnO_2 specific capacitance up to 425 F/g with good stability for over 3000 cycles under bending test);[68] carbon fabric with carbon nanoparticles (MnO_2 capacitance up to 800 F/g, areal capacity up to 109 mF/cm^2);[69] Zn_2SnO_4 coated carbon microfiber (621.6 F/g at 2 mV/s).[70] ZnO coated carbon cloth (138.7mF/cm2, 1260.9 F/g and 87.5% retention after 10 000 cycles);[71] CNTs buckypaper (516 F/g at 77 mA/g)[72] and graphene 3-D network that was obtained by direct growth using 3-D Ni foam as the sacrificial substrate (465 F/g with 0.1 mg/cm^2 of MnO_2, 1.42 F/cm^2 with 9.8 mg/cm^2 MnO_2)[73]

Most of the approaches described above for fabricating electrodes involved an "electrochemically-inert" component in their electrode structures (such as cotton textile and printer paper). These inert components, however, did not contribute to energy storage and therefore will reduce device level energy storage metrics. Hence, there are rising interests on the fabrication of electrodes without using inert supports. Li et al. fabricated flexible electrodes using graphene/MnO_2 composites simply by vacuum filtration of their aqueous dispersion.[74] Their study indicates that flexible electrodes with 24% of MnO_2 were able to deliver 256 F/g at 0.5 A/g but the MnO_2 loading is very low (~ 0.1mg). Electrodes with low MnO_2 loadings generally have high electrochemical activity but practical applications require high MnO_2 loadings.[75] In general, however, fabrication of flexible electrodes with both high MnO_2 loading and high specific capacitance is very challenging as any increase in MnO_2 loading will lead to a decrease in performance.

Table 1-3: Typical results for carbon/MnO_2 composites-based electrodes reported in the literature.

material	substrate	fabrication method	active material loading	results	remarks	Ref.
MnO_2	CNT coated paper	electrodeposition	0.38 mg/cm^2	540 F/g in 0.1 M Na_2SO_4 at 2 mV/s	20 Wh/kg and 1.5 kW/kg 5% drop for 1000 cycles	[62]
MnO_2	Graphene coated Textile	dip coating + electrodeposition	~0.4 mg/cm^2	315 F/g in 0.5 M Na_2SO_4		[65]
MnO_2	Carbon cloth	electrodeposition	0.2~1.2 mg/cm^2	425 F/g 230 mF/cm^2 in 0.1M Na_2SO_4	~ 6% loss during 1000 cycles	[68]
MnO_2	CNT coated sponge	electrodeposition	up to 12.8 mg/cm^2	~1000 F/g at 1mV/s for MnO_2 < 0.1mg/cm^2 ~200 F/g for MnO_2 > 0.5 mg/cm^2	~ 4% loss for 10000 cycles. 63 kW/kg and 31 Wh/kg	[63]
MnO2	CNT coated textile	electrodeposition	up to 8.3 mg/cm^2	2.8 F/cm^2 at 0.05 mV/s for 8.3 mg/cm^2 MnO_2 185 F/g at 0.8 mg/cm^2 of MnO_2	50% retention for 50 000 cycles 13 kW/kg and 5~20 Wh/kg	[64]
MnO_2	Graphene coated textile	electrodeposition	NA	380 F/g at 0.1mA/cm^2	20% and 45% capacitance increase with CNT and PEDOT wrapping, respectively	[67]
MnO_2	carbon nanoparticles coated carbon fabric	electrodeposition	0.072 ~ 0.562 mg/cm^2	109 mF/cm^2 with 0.562 mg/cm^2 MnO_2	15 min deposition lead to highest capacity (800 F/g)	[69]
MnO_2	Zn_2SnO_4 coated carbon microfiber	Chemical plating with $KMnO_4$	NA	621.6 F/g at 2 mV/s in 1M Na_2SO_4	36.8 Wh/kg and 32 kw/kg. active material loading is low	[70]
MnO_2	Graphene	Vacuum filtration	~0.07 mg	256 F/g with 24% of MnO_2 at 0.5 A/g	74% retention for 1000 cycles	[74]
MnO_2	Graphene and CNTs	Vacuum filtration	Up to 8.8 mg/cm^2	372 F/g at 10 mV/s, 130 F/cm^3	~ 200 F/g at 8.8 mg/cm^2	[76]
MnO_2	CNT buckypaper	electrodeposition	~20% of the whole electrode	516.2 F/g at 77 mA/g	88% retention for 3000 cycles	[72]
MnO_2	3-D graphene grown by CVD using Ni foam	electrodeposition	Up to 9.2 mg/cm^2 92.9% of the	130 F/g and 1.42 F/cm^2	Load with upto 92.9% of MnO_2 (entire electrode)	[73]
$Co(OH)_2$	CNTs/textile	hydrothermal reaction		11.22 F/cm^2 at 15 mA/cm^2	4% loss for 2000 cycles	[77]
V_2O_5	CNTs buckypaper	atomic layer deposition		Up to 1550 F/g in 8M LiCl	8% loss for 5000 cycles	[78]

1.4.2 Hybrids with other metal oxides/hydroxides

Several metal oxides/hydroxides based hybrids were also actively studied with the aim to develop high performance electrodes. Yuan et al. developed a process to fabricate flexible and porous cobalt hydroxide electrodes using conductive cotton textiles.[77] The conductive cotton textile was prepared by uniformly coating CNTs onto textiles also using the dip-coating process. Afterwards the textile was subjected to hydrothermal reactions to coat with the active $Co(OH)_2$. Electrochemical results show that such composite flexible electrodes were able to deliver high areal specific capacitance of 11.22 F/cm^2 at 15 mA/cm^2 and even 7.71 F/cm^2 at 60 mA/cm^2 with good stability of 4% capacity loss after 2000 cycles at high rates. In another study, electrodes were prepared by electrodeposition of porous $Co(OH)_2$ nanoflake films on stainless steel mesh. Such electrodes were able to deliver high specific capacitance of 609.4 F/g, good rate capability (less than 15% as current was increased by 10 times) and remarkable cyclic stability for 3000 cycles.[79]

Vanadium oxide is another widely studied material for pseudocapacitors. Boukhalfa et al. used an atomic layer deposition method to deposit ultrathin vanadium oxides on the surface of CNTs that was assembled as buckypaper. [78] Electrodes fabricated using this method was able to deliver remarkable capacitances of up to 1550 F/g per active mass of the V_2O_5 and 600 F/g per mass of the composite electrode at 1 A/g in 8 M LiCl. In another study, Perera et al. prepared electrodes consisting of V_2O_5 nanowires and CNTs using the vacuum filtration method.[80] Their study demonstrated that EC fabricated using such flexible electrodes as the anode and high surface area fiber electrode as the cathode exhibited a power density of 5.26 kW/kg and an energy density of 46.3 Wh/kg in an organic electrolyte (LiTFSI in acetonitrile, 3V voltage). They further prepared Li^+-doped V_2O_5 nanowires and showed that such nanowire-based flexible electrodes have improved electroactivity, reaching power density of 8.32 kW/kg and energy density of 65.9 Wh/kg. Such electrodes also have remarkable rate-performance as they delivered nearly stable capacitance over a wide range of current densities from 0.5 A/g to 10 A/g.

Zhang et al. synthesized porous CuO nanobelts with high surface area and small crystal grains and integrated them into fabricated flexible electrodes by depositing the mixture of CuO nanobelts and SWNTs as network films onto pure SWNT films without any binders.[81] The electrodes showed specific capacitance of 75.7 F/g when considering the total weight of the electrode in 1M $LiPF_6$/EC:DEC at 5 A/g with excellent cycling performances. Chen et al. prepared In_2O_3 electrodes by filtering its dispersion through a pre-prepared SWNT film.[82] The as-prepared flexible electrodes showed a layered structure and were able to deliver specific capacitance of 201 F/g. They further used this electrode to fabricate asymmetric supercapacitors as discussed below.

1.4.3 Asymmetric supercapacitors

As described in above, a working EC requires two electrodes, with one working as the positive electrode and the other one as the negative electrode. In assembly, these two electrodes can be either the same material or different materials. The development of pseudocapacitive materials with fast charge-discharge characteristics could enable EC with two electrodes paired with different materials, with a pseudocapative or battery type positive electrode (such as MnO_2) that relies on faradaic charge storage mechanism and a high surface area carbon based negative electrode that relies on EDLC. The asymmetric design combines the advantages of batteries and EC and enables devices with both high specific energy and specific power. More importantly, with asymmetric configuration the high overpotentials for H_2 and O_2 evolution at the carbon based electrode and pseudocapacitive electrode, respectively, extend the effective voltage window of aqueous electrolytes beyond the thermodynamic limit (~1.2V). As a consequence, asymmetric supercapacitors usually have higher specific energy density ($E \propto V^2$) compared with symmetric supercapacitors (identical material for the two electrodes) and received intense research focus over the past few years.[35, 83]

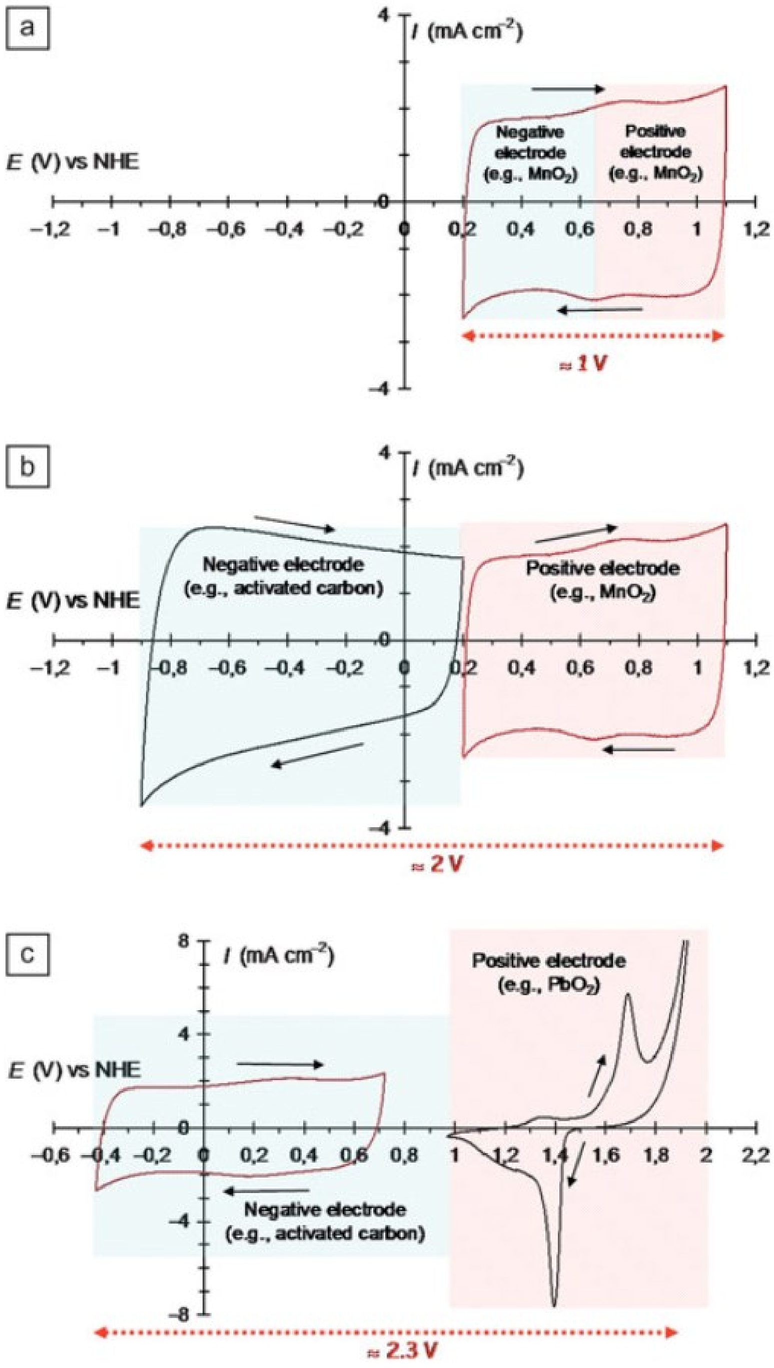

Figure 1.17: Schematic representation of cyclic voltammograms for three different configurations of aqueous-based EC in which areas shaded in red and blue represent the potential window of the positive and negative electrode, respectively for: (a) symmetric MnO2//MnO2 EC (b) asymmetric EC with AC//MnO_2 and (c) asymmetric EC with AC//PbO_2. This figure is adapted from ref. [35]

Since different materials with different energy storage characteristics are used, the fabrication of asymmetric EC requires optimization of the positive and negative electrodes to ensure high utilization efficiency. In this section we will introduce some of the typical results obtained on the fabrication of asymmetric supercapacitors, where in most cases a metal-oxide based electrode is used as the positive electrode and a carbon-based electrode is used as the negative electrodes.

The combination of positive electrodes based on MnO_2 and negative electrodes based on carbon is probably the most widely studied system for asymmetric supercapacitors (ASC).[35] In principle, the combination of MnO_2//carbon should be able to afford ASC with voltages of ~ 2.0 V in aqueous electrolytes. Yu et al. assembled ASC using graphene/MnO_2-textile as the positive electrode and CNT-textile as the negative electrode.[65] The fabrication of such textile electrodes is identical as discussed in the previous sections. The devices can be operated with 1.5V and were able to deliver energy density of 12.5 Wh/kg and power density of 110 kW/kg that are both higher then symmetric supercapacitors. The devices also have excellent cyclic performance, with ~95% capacitance retention over 5000 cycles at 2.2 A/g. In a similar study, Shao et al. used porous graphene/MnO_2 nanorod and graphene/Ag thin films that were both prepared using the vacuum filtration method as positive and negative electrode, respectively, in their fabrication of ASC.[84] This study demonstrated that Ag nanoparticles are very important in improving the performance of the graphene negative electrode because they can repair defects in the graphene surface and enhance their electronic conductivities. Additionally, they can also work as spacer to eliminate the restacking between adjacent graphene sheets. These devices exhibited a maximum energy density of 50.8 Wh/kg and still retain 7.53 Wh/kg at a high power density of 90.3 kW/kg. Their bending tests revealed that such devices are very promising as flexible ASC, with only 2.8% decrease in specific capacitance under bending conditions.

Hybrid electrodes that could effectively utilize the full potential of all the desired functions of each component are particularly promising for developing high performance electrodes. Lu et al. developed a procedure to fabricate flexible solid-state ASC based on one-dimensional core-shell nanowire hybrids.[85] In their approach, electroactive MnO_2 (positive electrode) and carbon shell (negative electrode) were uniformly coated onto hydrogen-treated TiO_2 that was pre-synthesized on carbon cloths. Devices fabricated using these electrodes were able to operate in 1.8 V and deliver a high specific capacitance of 139.6 F/g with maximum volumetric energy density of 0.3 mWh/cm^3 (59 Wh/kg) and volumetric power density of 0.23 W/cm^3 (45 kW/kg). Moreover, the device has excellent cycling performance (8.8% capacitance loss for 5000 cycles) and good flexibility.

Other combinations of materials are also being studied besides the MnO_2//carbon system as discussed above to prepare flexible ASC with high power and energy densities. A remarkable example is the flexible asymmetric supercapacitors based on MnO_2 and In_2O_3 and carbon nanotube films.[82] The optimized devices were able to operate in 2V window and deliver specific capacitance of 184 F/g, energy density of 25.5 Wh/kg and power density of 50.3 kW/kg. RuO_2 is one of the most widely studied materials for supercapacitors due to its remarkable performances. In a recent study, Choi et al fabricated flexible asymmetric supercapacitors using an ionic liquid functionalized-chemically modified graphene (IL-CMG) film as the negative electrode and a RuO_2-IL-CMG composite film as the positive electrode.[86] A solid-state electrolyte made with polyvinyl alcohol-H_2SO_4 was used to fabricate all-solid-state devices. Such asymmetric supercapacitors with optimized structure were able to be operated with cell voltage up to 1.8V and deliver a high energy density of 19.7 Wh/kg and power density of 6.8 kW/kg. More remarkably, such devices can be operated with high rate of 10 A/g with 79.4% retention of specific capacitance.

Chapter 2: Comparing Graphene and Carbon Nanotubes as Nanoscale Current Collectors in MnO_2-based EC*

2.1 Introduction

As has been discussed in Chapter 1, manganese oxide (MnO_2) is particularly attractive for EC due to its low cost, abundance and environmental compatibility.[87] Although a theoretical calculation indicates its specific capacitance (SC) can be as high as 1380 F/g, experimental results hardly reach this number (usually ~ 200 F/g under low current conditions) and also drops significantly at higher current densities due to poor conductivity of MnO_2. Recently, several research groups have observed that ultrathin (ten to hundreds of nanometers thick) MnO_2 films deposited onto flat current collectors have very high SC in the range of 700 to 1380 F/g.[88-91] They concluded that ultrathin films can overcome the poor electrical conductivity limitation of MnO_2 and reduce the ion diffusion length. Inspired by these findings, a novel approach of fabricating electrodes by translating flat current collectors to 3-D nanoscale current collectors that can support ultrathin MnO_2 has been proposed and applied. This 3-D approach combines the advantages of ultrathin MnO_2 film and high mass loadings of thick films and therefore has received tremendous interests. Typically, the 3-D current collectors being used are various forms of high surface area carbon, such as CNTs, [58, 92, 93] carbon areagels/

---

* This chapter has been published in ***Journal of Nano Energy and Power Research***, 2013, 2, 41-47.

nanofoam[94], templated mesoporous carbon[95, 96] and graphene. [97, 98] With these highly conductive nanostructured carbon serving as 3-D nanoscale current collectors, the SC and rate performance of MnO_2 can improve dramatically.

Several previous works have demonstrated that both graphene and CNTs were able to improve the performance of MnO_2 for EC.[83, 97, 98] However, it is still not clear which material performs better due to limited understanding on the structure and properties of their composites with MnO_2. With the motivation of designing high performance electrodes, it is therefore necessary to compare the effectiveness of graphene and CNTs so that we can rationally select materials/composites. In this project, we first examined the behavior of RGO as the current collector by studying the electrochemical behavior of the RGO/MnO_2 composites with various ratios synthesized through a facile chemical co-precipitation method. Our results show that the energy storage characteristics of MnO_2 were greatly improved in the RGO/MnO_2 composite. Compared with pure MnO_2, the *SC* of the composite was not only higher but also largely retained at increased scan rates and mass loading densities, demonstrating excellent performance of RGO as a type of nanoscale current collector. We also found that compared with RGO, the MnO_2 composites made from fFWNTs using the same approach have better performance as thin films, likely due to higher electrical conductivity. However, as the film gets thicker, the ion diffusion resistivity across the film seems becomes the major limitation and the two composites behave very similarly.

2.2 Experimental section

2.2.1 Synthesis and reduction of GO

GO was synthesized using a modified Hummers method (shown in Figure 2.1).[32, 99] Briefly, 2 g of natural graphite flake, 2 g of $NaNO_3$ and 90 ml of concentrated H_2SO_4 were mixed in a flask that was kept and stirred in an ice bath. Afterwards 12 g of $KMnO_4$ was added slowly to avoid overheating. The mixture was firstly stirred in the ice bath for 1.5 h and then at 35°C for 2 h. Next, 90 ml nanopure water was added dropwise to dilute the mixture, followed by another addition of 200 ml nanopure water and 10 ml H_2O_2 (30%). After 10 min, a brownish suspension was obtained (graphite oxide). Removal of the residual chemicals in the suspension was achieved by a three steps centrifuge at 16000 rpm. The centrifuged slurry was collected at each step and dispersed in nanopure water prior to the next centrifuge step. Followed by this, a mild sonication (20 min) was used to exfoliate the graphite oxide to GO. Finally, a low-speed centrifuge at 7000 rpm was used to remove large, thick multilayer graphite oxide until the supernatant was free of visible particles. The GO suspension obtained here is ready to use for next step after a dilution with nanopure water to the targeted concentration of 0.25 mg/ml.

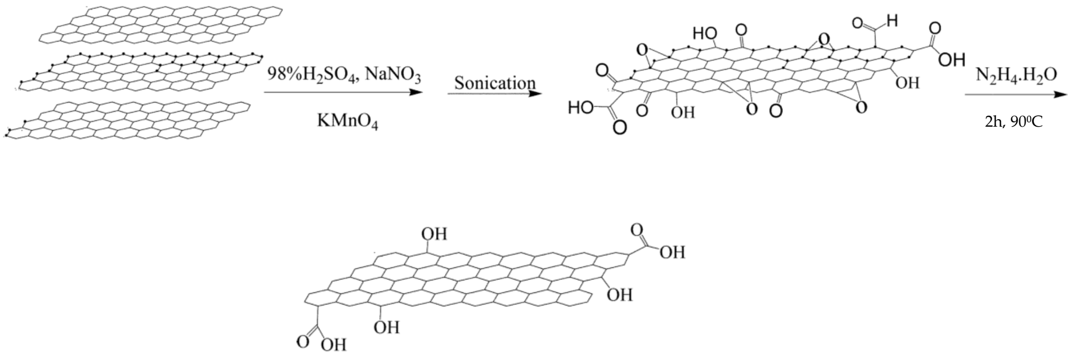

Figure 2.1: Schematic illustration of the reduced graphene oxide synthesis process

The reduction of GO was followed by a method developed by Li et al.[100] Typically, 18.0 µl of hydrazine solution (35% in water) and 126 µl of ammonia solution (28% in water) were added to 36 ml of GO dispersion (0.25 mg/ml) in a flask. After vigorous shaking, the flask was put in an oil bath and was heated at 90°C for 1 h. After cooling down to room temperature, the dispersion was dialyzed against a 0.5% ammonia solution for 24 h to remove residue hydrazine. The dispersion after dialysis was made with RGO and was used directly for synthesizing composites.

2.2.2 Synthesis and functionalization of few-walled carbon nanotubes

Few-walled CNTs were prepared by a bimetallic catalyst Co/Mo supported on MgO support following our published process.[101] Methane was used as the carbon source and hydrogen was also used with certain ratio to control methane decomposition rate. In a typical experiment, MgO supported Co/Mo catalyst was put into a quartz tube and was flushed with hydrogen while the catalyst was heated to the growth temperature. Afterwards methane was introduced for desired time (10–30 min) and then methane flow was turned off and hydrogen flow was kept on while the system is being cooled down.

To functionalize FWNTs, 2.0 mg of purified material was dispersed in 15 ml oleum and stirred continuously at room temperature for 48 hours. Afterwards the mixed solution was heated to 70°C and 5 ml of concentrated HNO_3 was then added at an injection rate of 0.3 ml/min. The final mixture was kept at 70°C for 2 hours, after which the solution was cooled, and 250 ml of nanopure water was added slowly to dilute the acids. The diluted solution was filtered, with the functionalized FWNTs collected and re-dispersed in water to make the fFWNTs/MnO_2 composite.

2.2.3 Synthesis of MnO_2 and MnO_2/carbon nanomaterial composites

Pure MnO_2 particles were synthesized with the chemical co-precipitation method[49, 102] that has been widely used by many research groups with slight modifications. Typically, 2.3 ml of $MnSO_4$ (0.03 M) and 2.3 ml $KMnO_4$ (0.02 M) were subsequently added into 35.4 ml of nanopure water. The mixed solution was kept for 1 h under vigorous stirring to ensure a complete reaction. The suspension was then vacuum filtered through a PTFE membrane (200 nm pore size) to collect the MnO_2 powder and washed with nanopure water.

RGO/MnO_2 and fFWNTs/MnO_2 composites were prepared with a sonochemical coprecipitation method. Typically, 2.3 ml of $MnSO_4$ (0.03 M) was added to the RGO dispersion that was obtained in step 2.2.1 while under probe sonication (20%

amplitude). After 1 h of sonication, 2.3 ml of $KMnO_4$ (0.02 M) was slowly added and sonication was continued for another 2 h. The amount of $MnSO_4$ and $KMnO_4$ could be varied depending on the desired ratio of MnO_2 to RGO. After sonication, the resulting RGO/MnO_2 composite was collected by vacuum filtration through a PTFE membrane (200 nm pore size) and washed repeatedly with nanopure water. fFWNTs/MnO_2 composites were prepared with an identical approach, and RGO was replaced with equivalent amount of fFWNTs.

2.2.4 Electrochemical measurements

Electrochemical tests were performed using a Bio-logic SP300 instrument with a standard three electrodes configuration. An Ag/AgCl (4M KCl) electrode and a platinum wire were used as the reference and counter electrode, respectively. A flat Au electrode with active material coating was used as the working electrode. Capacitance evaluation was conducted with cyclic voltammogram (CV, -0.1V ~ 0.9V) and galvanostatic charge-discharge techniques in 1 M Na_2SO_4 electrolyte. SC was determined by integrating the CV curve over the potential window of 1 V and calculated according the equation of $C = \frac{\int IdV}{vmV}$, where C is the specific capacitance (F/g), I is the response current, V is the potential window, v is the CV scan rate (mV/s), and m is the mass of the electroactive material.

2.2.5 Material characterization

The crystallographic structure of the powder materials was analyzed by a panalytical X'Pert PRO MRD HR X-ray diffraction system equipped with Cu Kα radiation (λ=0.15405nm). X-ray photoelectron spectroscopy (XPS) measurements were performed using a Kratos Analytical Axis Ultra XPS system with a monochromatic Al Kα (hv = 1486.6 eV) source. All XPS spectra were corrected using the C 1s line at 284.5 eV. The morphology of the material was studied with a scanning electron microscope (SEM, FEI XL30) and transmission electron microscopy (TEM, FEI Tecnai G^2 Twin). The specific surface areas were determined according to the Brunauer-Emmett-Teller (BET) method, from the absorption data collected with a Micromeritic Tristar system at 77K. Electrical conductivity of the material was measured with a four-probe station (Keithley multimeter). The thickness of the electrode was measured by a Bruker Dektak 150 profilometer.

2.3 *Results and discussion*

2.3.1 Characterization of the MnO_2/RGO composite

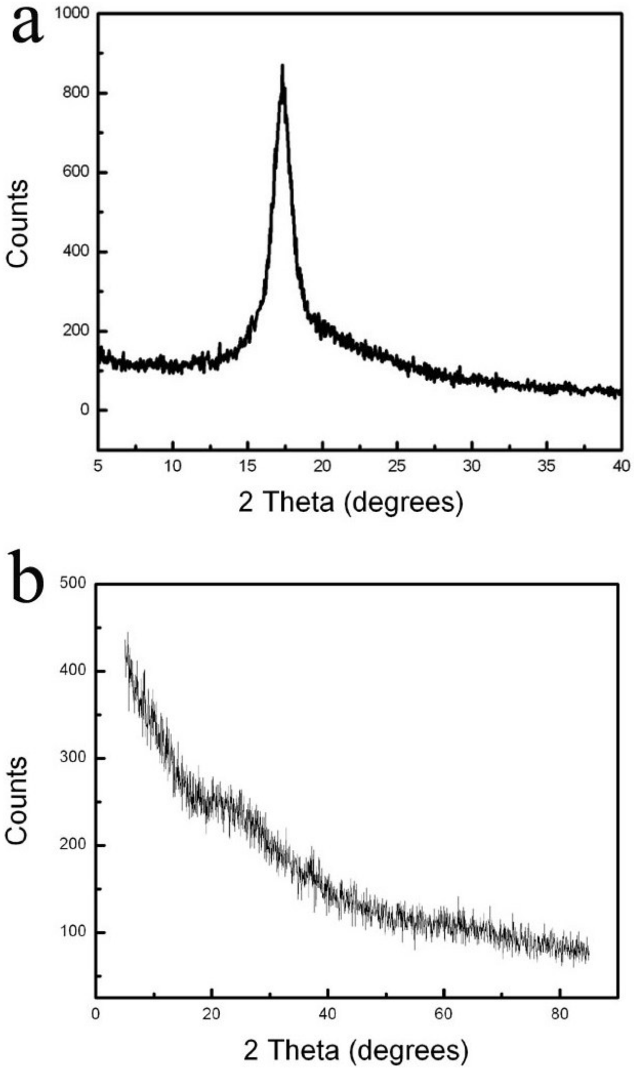

Figure 2.2: X-ray diffraction pattern of (a) RGO and (b) RGO/MnO_2 composite.

In this project, we used a simple but effective ultrasound-mediated co-precipitation approach to synthesize the RGO/MnO_2 composite. This method ensures uniform and controllable coating of MnO_2 on RGO surface and avoids aggregation of RGO sheets. The X-ray diffraction pattern shows that the composite was amorphous

(Figure 2.2a), similar to that of MnO_2 powders synthesized without RGO present. It is worth noting that the diffraction peak from RGO disappeared for the composite, demonstrating that MnO_2 has successfully coated onto the graphene sheets and lead to a wider separation between them, which would otherwise be narrow enough to give diffraction response (Figure 2.2b). [103] The nitrogen adsorption-desorption isotherm of the composite shows typical type IV isotherm (Figure 2.3), with BET specific surface area in the range of 170~230 m²/g depending on the composition of the composites (Table 2.1).

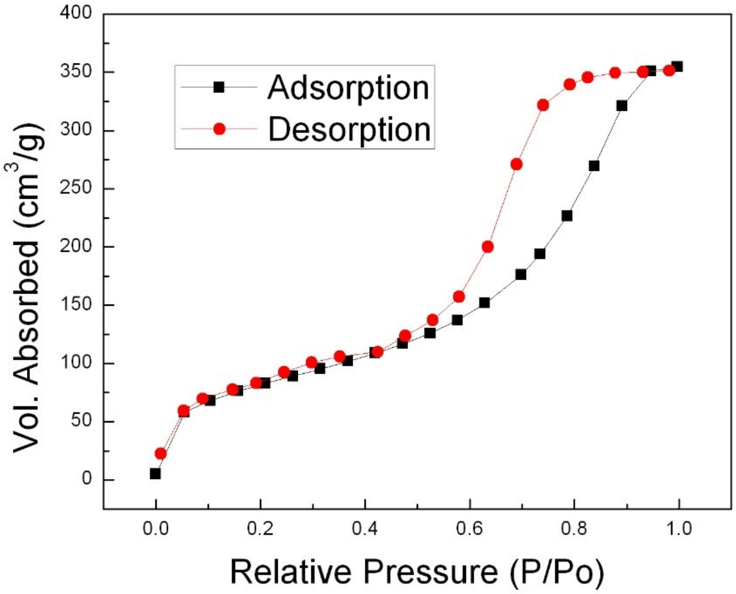

Figure 2.3: Nitrogen adsorption-desorption isotherm of the RGO/MnO_2 composite

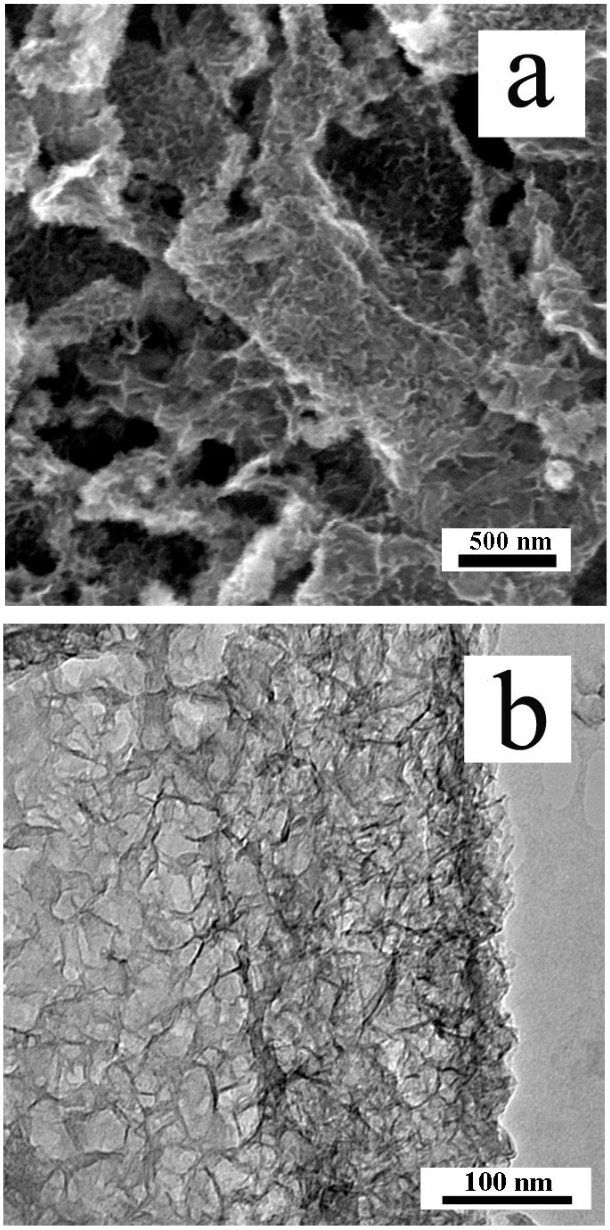

Figure 2.4: (a) SEM and (b) TEM image of the composite material, showing the uniform coatings of nanoscale MnO_2 on RGO sheets.

The morphology of the composite was studied with SEM (Figure 2.4a) and TEM (Figure 2.4b). After the ultrasound-mediated coprecipitation process, it can be seen that nanoscale MnO_2 particles were coated uniformly on the surfaces of RGO. The TEM images (Figure 2.4b) revealed that the edge area of graphene has a relatively thicker MnO_2 coating, which is probably due to higher density of functional groups (such as hydroxyl and carboxyl groups) at the edges. Nevertheless, most of the available surfaces of graphene have been coated with MnO_2 within nanoscale thickness, which agrees well with the XRD pattern. The XPS spectrum acquired from this composite shows that it is free from contaminants (Figure 2.5).

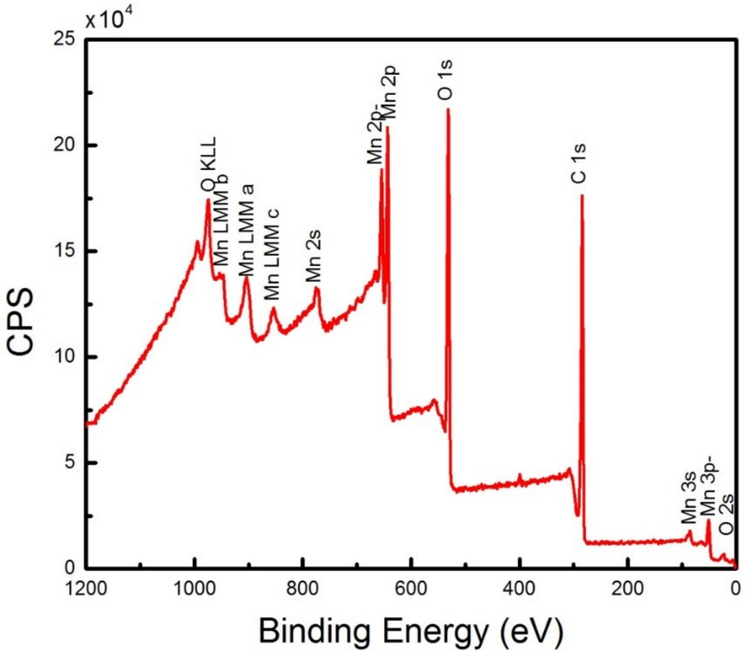

Figure 2.5: XPS survey spectrum of the synthesized RGO/MnO_2 composite.

The average manganese oxidation state was determined from the Mn 3s and O 1s core level XPS spectra. As reported previously,[104] the Mn oxidation state can be determined from the binding energy width (ΔE) between the separated Mn 3s peaks due to multiplet splitting. By reference to ΔE data of 5.79, 5.50, 5.41 and 4.78 eV acquired from reference samples of MnO, Mn_3O_4, Mn_2O_3 and MnO_2, respectively, the possible oxidation state of Mn contained in the composite was estimated as 3.82 (Figure 2.6A). Another effective way of determining the Mn oxidation state is from the O 1s core level spectrum.[88] By using the equation suggested in this paper,[58] the possible valence of Mn was 3.79 (Figure 2.6B). Based on these XPS analyses, the main compound of Mn in the composite is MnO_2 and/or Mn_3O_4. All these results indicate the effectiveness of our simple synthesis approach in fabricating the RGO/MnO_2 composites.

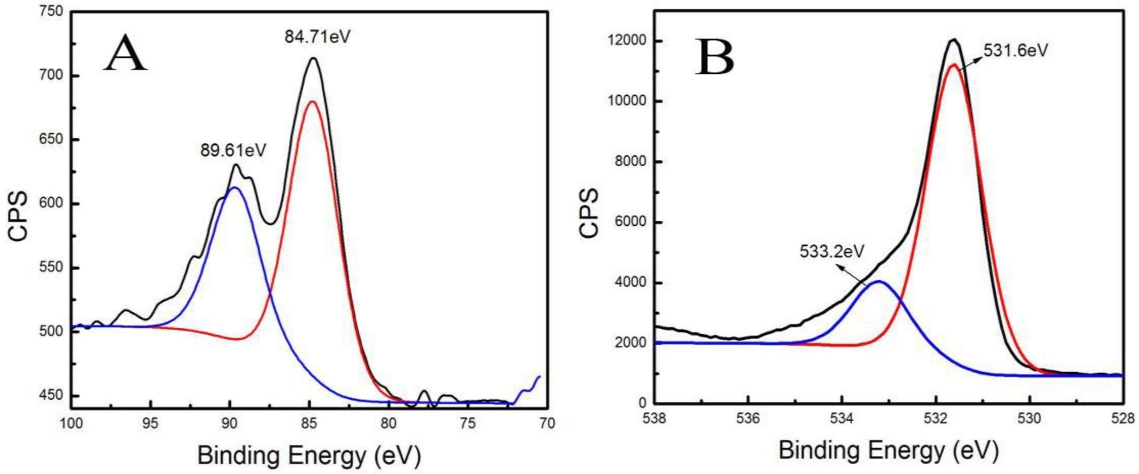

Figure 2.6: XPS spectra of the MnO_2 in Mn 3s (A) and O 1s (B) region. The raw data are represented by the black lines, and the fitted data are represented by the red and blue lines, repectively. The peaks at 531.6eV and 533.2eV in the O 1s core level spectra originate from Mn-O-Mn and Mn-O-H bonds.

2.3.2 Evaluation of RGO as the nanoscale current collector in RGO/MnO_2 composites

With the addition of 40 wt% RGO, the conductivity of the film increased dramatically from nearly insulating of 10^{-5}-10^{-6} s/cm for pure MnO_2 [91] to 0.045 s/cm. Hence, it is expected that the composite film should have improved electrochemical performance. A set of typical CV curves of this composite recorded at increasing scan rate were plotted in Figure 2.7a. As can be seen in this figure, the curves show close to the ideal rectangular shape even at a high scan rate of 500 mV/s, indicating a low contact resistance and superior high-rate performance. The calculated *SC* at 10 mV/s is 360 F/g and this is much higher than ~175 F/g for pure MnO_2 obtained at similar mass densities. The capacitance retention ratio (defined in this paper as the ratio of the *SC* at 500 mV/s over 10 mV/s) of 63% for the composite is also much higher than the 35% for pure MnO_2. The galvanostatic charge-discharge curves of the composite are also shown in Figure 2.7b. It can be seen that all these curves are highly linear and symmetrical at various current densities from 1 A/g to 25 A/g, further indicating the superior electrochemical reversibility and charge-discharge properties of the composite material.

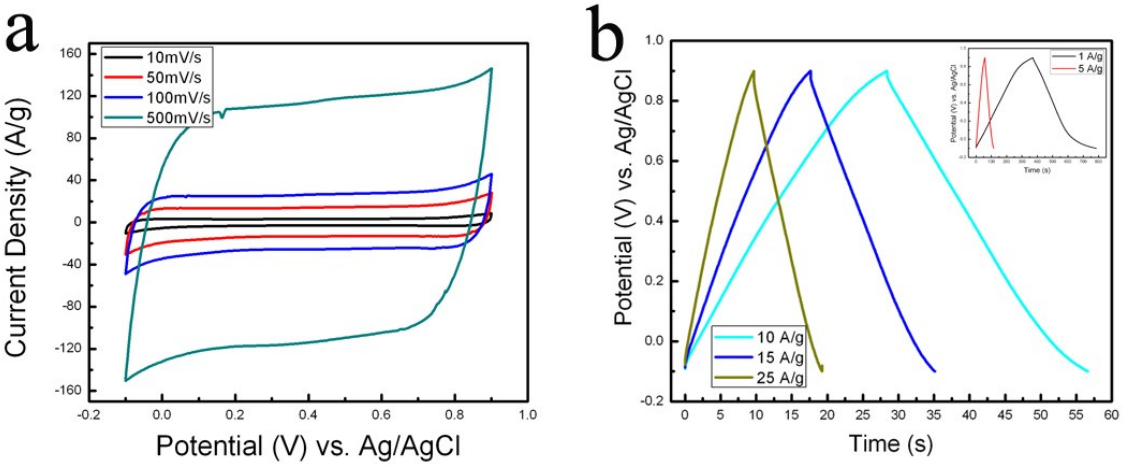

Figure 2.7 **Electrochemical characterization results of the RGO/MnO_2 composite. (a) Set of CV curves acquired at increasing scan rate from 10 mV/s to 500 mV/s. (B) Galvanostatic charge-discharge curves obtained at current density from 1 A/g to 25 A/g.**

The thickness of MnO_2 loaded on RGO sheets is an important factor that could affect the performance of the composite since the *SC* of MnO_2 decreases sharply with increased thickness[89]. To study this effect, we synthesized and examined composites with different MnO_2 ratios. Electrochemical measurements performed on these composites revealed that all of them have close to ideal EC behavior with low contact resistance. Their *SC* at 10 mV/s and capacitance retention ratios were calculated and compared in table 2.1.

Table 2-1: Comparison of the characterization results for the RGO/MnO_2 composites with different MnO_2 ratios

MnO_2 wt%	*20%*	*35%*	*52%*	*68%*	*84%*	*100%*
Specific surface area (m^2/g)	171	219	228	220	200	230
Specific surface capacitance ($\mu F/cm^2$)	81	93	96	99	110	85
Specific capacitance (MnO_2, F/g)	690	580	419	320	263	197
Capacitance Retention (%)	78	71	64	65	64	41

All of the electrodes were controlled to have mass densities around 0.2 mg/cm^2 to ensure comparable results. As summarized in this table, the composite with low MnO_2 ratio of 20% has a high *SC* of 690 F/g at 10 mV/s and high capacitance retention of 78%. As the mass ratio of MnO_2 increases, the *SC* clearly decreases, with the capacitance retention ratio also decreasing slightly. The *SC* for MnO_2 in the composites that have 35%, 52%, 68% and 84% of MnO_2 are 580 F/g, 419 F/g, 320 F/g and 263 F/g, respectively, with the corresponding capacitance retention ratios as 71%, 66%, 66% and 65%. The decrease in the *SC* might be due to the increase in the diffusion resistivity of electrolyte ions across thicker MnO_2 layers. However, despite the significant differences in the *SC*, the specific surface capacitances of these composites remain similarly around ~95 μF/cm^2. This similarity indicates that capacitance of MnO_2 depends strongly on the available surface area. The generally proposed charge storage mechanism of MnO_2 involves a surface faradic charge transfer process and an intercalate/deintercalate process within the bulk material.[50] However, the surface process seems to be the dominant mechanism in our system. The high performance of composites with lower MnO_2 ratios may indicate that when MnO_2 exists as an ultrathin layer on the current collector, the diffusion length of ions is greatly reduced and thus electrolyte ions have access to most of the pores, which could lead to a nearly complete surface redox reaction. In addition, the interconnected network formed by RGO sheets provides highly conductive channels for electron transport over the film and thus, significantly improves the performance of the composites at high scan rates. However, with the increment of the MnO_2 thickness, the effective interaction between the electrolyte ions and the electrode is greatly reduced and results in a reduction in their performance.

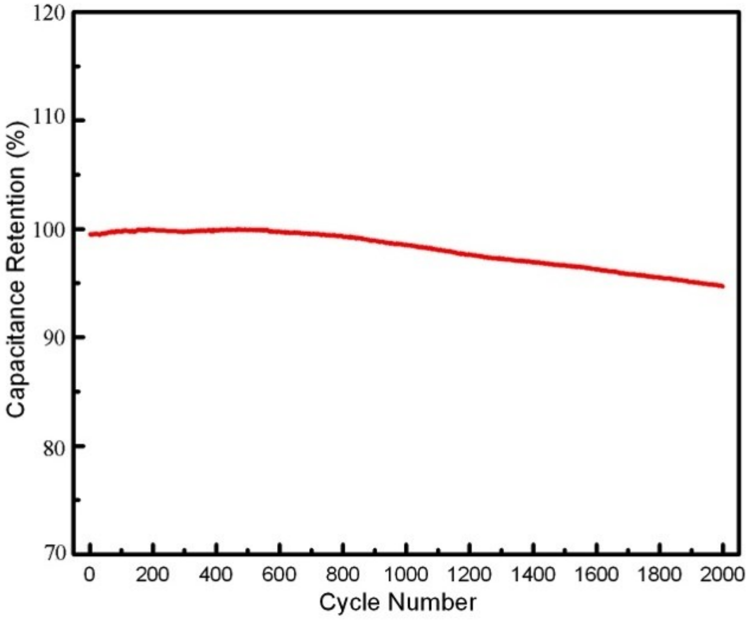

Figure 2.8: Cycling stability of a RGO/MnO$_2$ electrode upon charging/discharging at a current density of 5 A/g.

The electrochemical stability of the composite material was evaluated by charge-discharge test conducted at a high constant current density of 5 A/g for 2000 cycles. The capacitance retention ratio as a function of cycle numbers is presented in Figure 2.8. As this figure shows, the capacitance decreases only 5.5% of the initial value after 2000 cycles without the addition of any binder, demonstrating excellent electrochemical stability of the composite material that is largely originated from the mechanical stability of RGO sheets. EC materials with such excellent stability are crucial for practical applications.

2.3.3 Comparison of graphene and CNTs as nanoscale current collectors

To compare the effect of RGO and carbon fFWNTs as the nanoscale current collector, we synthesized and examined fFWNTs/MnO_2 composites with the same MnO_2 concentration of 60% as the RGO/MnO_2 composite. A typical TEM image of the fFWNTs/MnO_2 composite is presented in Figure 2.9a, which shows that the MnO_2 grew uniformly on the nanotubes as flow-like particles. Figure 2.9b shows a set of typical CV curves acquired from this composite. It can be seen that similar to RGO/MnO_2, the fFWNTs/MnO_2 composite also shows close to ideal rectangular CV curves at increasing scan rates.

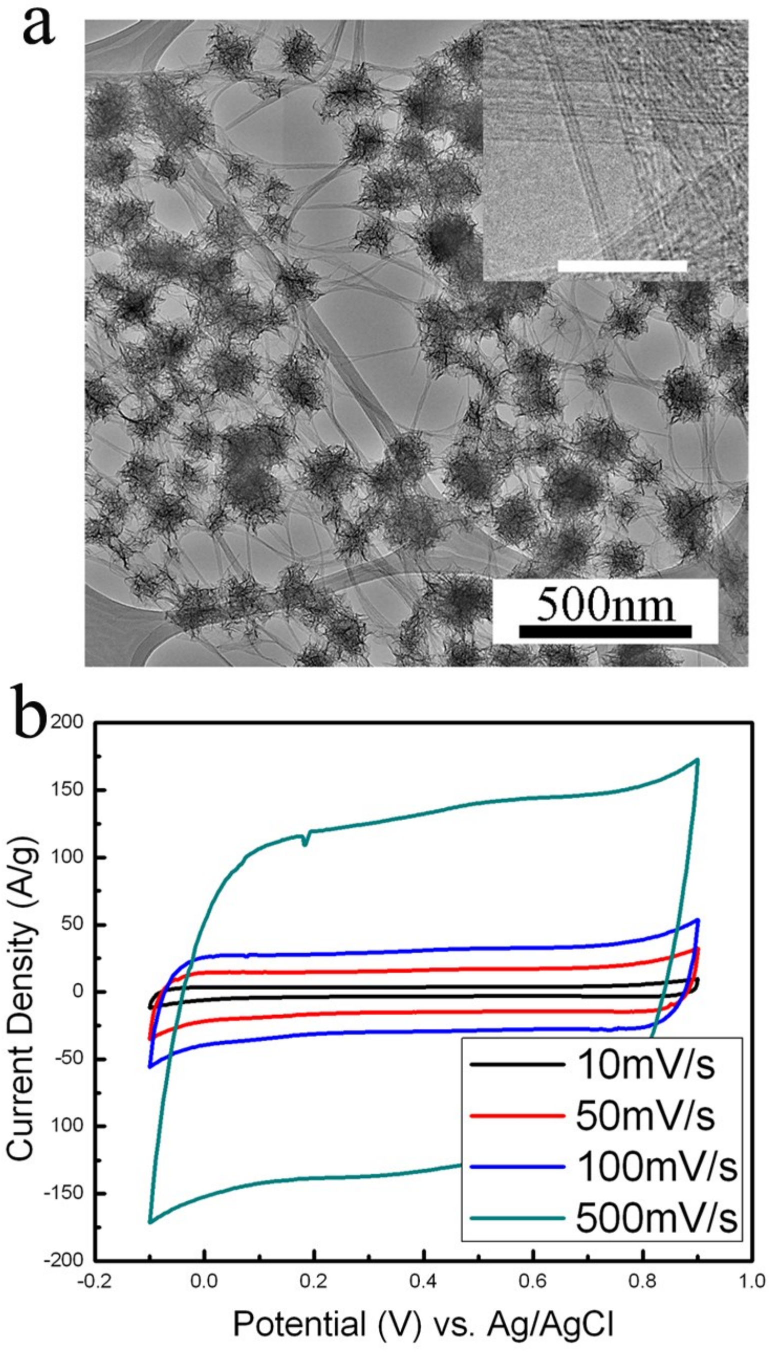

Figure 2.9: (a) TEM image of the fFWNTs/MnO_2 composite that shows the MnO_2 grew uniformly on carbon nanotube as flower-like particles. The inserted picture is a typical TEM of the FWNT (scale bar is 10 nm); (b) A set of typical CV curves acquired from the fFWNT/MnO_2 composite at increasing scan rate

Supposedly, ideal nanoscale current collectors should be able to provide electron conductance throughout the composite film that independent of the macro-scale film thickness, with performance of the composites relying only on the thickness of the MnO_2 deposited on them. Hence, a comparison between RGO and fFWNTs as nanoscale current collector was conducted by examining the performance of their composites with varied mass loading densities. The *SC* and capacitance retention ratio obtained from these composites are compared in Figure 2.10 a and b. The behavior of pure MnO_2 is also included in these two figures. As can be seen from Figure 2.10 a, both RGO and fFWNTs improved the performance of $MnO_{2,}$ with the *SC* generally higher than 300 F/g at various mass loading densities. In contrast, the *SC* of pure MnO_2 was much lower and only 130 F/g for thicker film due to its poor conductivity that results in a high ion diffusion resistivity.[88] Compared with RGO/MnO_2, the fFWNTs/MnO_2 composite has much higher *SC* at mass density lower than 0.1 mg/cm^2 (730 F/g vs. 460 F/g at ~ 0.050 mg/cm^2). However, the difference of these two composites decrease to less than 10% as the film gets thicker. Since the error from the mass measurement by an electrical balance must be accounted for, we conclude that the difference of these two composites are similar at higher mass loadings.

The better performance of the fFWNTs/MnO_2 composite as a thin film may track to its higher conductivity. According to our measurement, the conductivity of fFWNTs/MnO_2 as 4.11 S/cm, much higher than the 0.045 S/cm for RGO/MnO_2. This may originate from the fact that CNTs are more conductive than RGO (275 S/cm for functionalized CNTs[105, 106] and 1.56 S/cm for RGO obtained by the hydrazine reduction method[106]). The similarity of these two composites at higher densities may indicate that the ion-diffusion resistivity across the thick film, rather than the electrical conductivity, has become the major limiting factor in determining their performance.

Despite the differences in the *SC*, the capacitance retention ratios of these two composites remain stable in the range of 55~65% across the mass loading densities that we studied (Figure 2.10 b). In contrast, this ratio for pure MnO_2 decreases sharply from 52% at low mass loading density to only 22% at high density. Hence, we conclude that both carbon nanotube and RGO have excellent performance as the nanoscale current collector. In summary, our comparison results indicates that the fFWNTs/MnO_2 composite is preferable for ultra-thin film EC, while RGO/MnO_2 composite might be good for systems that require thick, large-scale material coating due to its economic advantage.

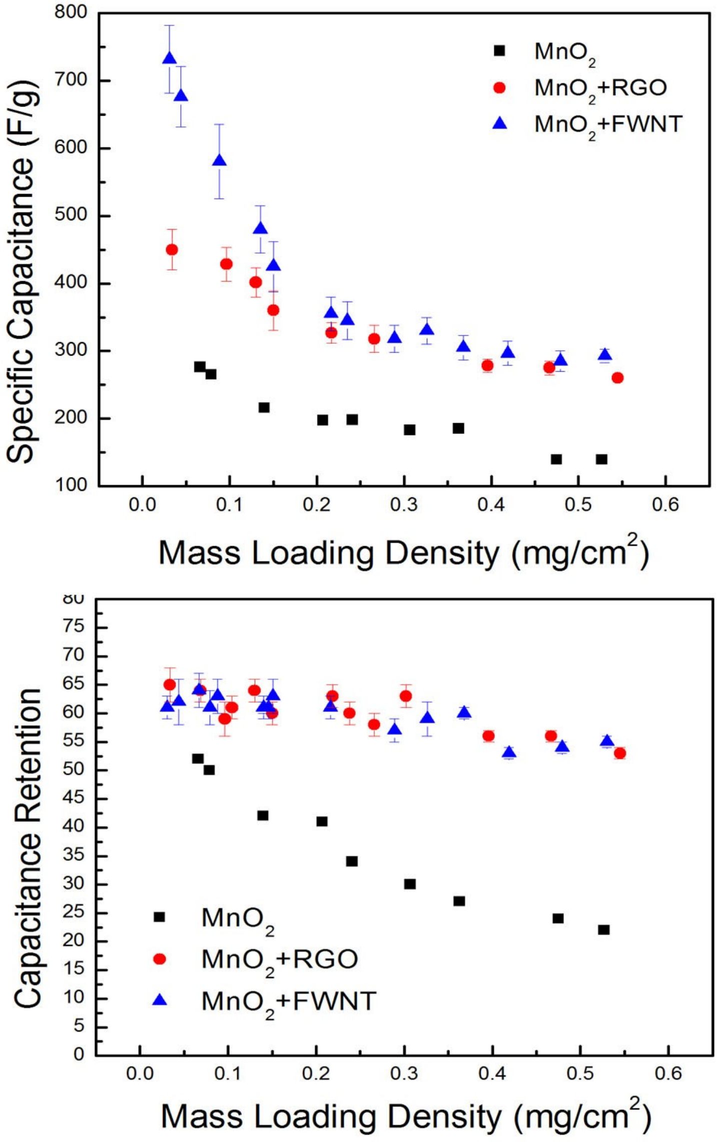

Figure 2.10: (a) comparison of the C_{sp} and (b) capacitance retention ratios as a function of the mass loading densities for the fFWNTs/MnO$_2$, RGO/MnO$_2$ and pure MnO$_2$.

2.4 Conclusion

In summary, in this chapter we described a facile but efficient method to synthesize high surface area RGO/MnO$_2$ composites through the chemical coprecipitation route. This composite material combines the advantage of high performance of ultrathin MnO_2 layers and the electrical conductivity and mechanical stability of RGO and thus has superior EC performance. The *SC* of MnO_2 in the composite is generally higher than 300 F/g and is largely retained at higher scan rates (over 55% at 500 mV/s). Compared with RGO/MnO_2, the composite of fFWNTs/MnO_2 has better performance as thin films due to its better electrical conductivity. However, these two composites perform very similarly as thick films. These results demonstrate that the fFWNTs/MnO_2 is preferable for ultra-thin EC systems, while the RGO/MnO_2 composite is attractive for thick systems. Our finding may be useful for designing electrochemical EC systems for portable electrical devices, hybrid vehicles and back-up energy storage devices where high rate power supply is desired.

Chapter 3: Synergistic Effects from Graphene and Carbon Nanotubes Enable Flexible and Robust Electrodes for High-Performance Supercapacitors*

3.1 Introduction

Manganese dioxide (MnO_2), a traditional battery material, has received tremendous interest recently in supercapacitor applications due to its natural abundance, low cost, low toxicity and high theoretical capacitance close to 1300 F/g.[51, 107] MnO_2 stores energy through a charge-transfer, faradic reaction that is known as pseudocapacitance.[49] However, two major challenges exist when integrating MnO_2 with flexible energy storage systems: its poor electrical conductivity (10^{-5}~10^{-6} s cm^{-1}) and rigid metal oxide nature. The poor conductivity limits its performance as thick films in electrochemical applications due to its strong thickness-dependent electroactivity.[88] Despite the fact that MnO_2 has extremely high SC exceeding 700 F/g when made as an ultrathin film with thickness less than 100 nm,[108, 109] most reported studies only observed a SC of less than 200 F/g when the MnO_2 electrodes exceed 1 mg/cm^2 areal density.[102, 110] Conventionally, the approach to fabricate flexible electrodes is to deposit the electroactive material directly on flexible and conductive substrates, such as CNT buckypaper,[111] carbon foam[94], carbon fabric[69] and DVD media discs etc.[112] More recently, coating metal oxide, graphene and/or CNT composite on papers, textiles and sponges

---

[*] This chapter has been published in Cheng et al. ***Nano Letter***, 2012, 12, 4206-4211.

were also reported as feasible methods to prepare flexible electrodes for supercapacitors.[63, 113-115] However, the utilization of electrochemically inert supports significantly reduces the overall energy and power density of the devices. Besides, in such approaches, trying to increase MnO_2 loading density usually requires its thickness to be increased, which will significantly reduce its electrochemical activity.[63, 113] Thick MnO_2 (>1 mg/cm^2) film also suffers from significant decrease in capacitance under high current conditions. For example, the *SC* of a MnO_2-CNT-textile electrode is reduced from ~150 F/g to ~50 F/g when the scan rate increased from 5 mV/s to 200 mV/s.[113] Thus, designing a scalable process for fabricating robust and flexible MnO_2-based films for supercapacitors with high electrochemical performance and high mass loading density still remains a challenge.

3.2 Experimental details

3.2.1 Materials and methods

The graphene dispersion and graphene/MnO_2 composites were prepared using methods as described in 2.2. The methods for synthesis, purification and functionalization of FWNTs were also same as described in 2.2. The flexible graphene/MnO_2/fFWNTs films were fabricated by vacuum filtration method. Typically, desired amounts of functionalized fFWNTs dispersion and graphene/MnO_2 suspension were mixed in a glass vial. The amounts varied to control the thickness of the final film (for example, 20 ml of CNTs dispersion and 33 ml of graphene/MnO_2 suspension were used to make a film with 2.02 mg/cm^2 areal density). The mixed solution was then sonicated for 20min and filter through a mixed cellulose ester membrane (1.2μm pore size, Millipore). The obtained filter cake was then vacuum dried for 24 hours to get a freestanding film.

3.2.2 Material characterization and electrochemical measurements

The methods for material characterization and electrochemical evaluation were the same as described in 2.2. In this project, flexible films were used directly without any mechanical support as the working electrode. The rolled-up full cell for symmetric capacitor measurements was assembled by rolling the stacked films that was stacked in the order of separator/flexible film/separator/flexible film. Two platinum wires were included to connect the flexible film to the external measurement circuit. After assemble, a carbon tape was used to hold the structure. Then the whole cell was immersed in 1M Na_2SO_4 for the electrochemical measurements

3.2.3 Data analysis

Using the cyclic voltammetry testing data, the specific capacitance was calculated according to the equation of $C = (\int IdV)/vmV$, where C is the specific capacitance (F/g), I is the response current, V is the potential window, v is the CV scan rate (mV/s), and m is the mass of the electrode material.

The specific capacitance of MnO_2 was estimated by subtracting the contribution of the fFWNTs from the results obtained from the flexible electrodes using the equation below:

$$C_{sp} = \frac{C_{ff} - C_{CNT} * wt\%(CNT)}{wt\%(MnO2)}$$

where the C_{ff} is the C_{sp} of the flexible electrode, C_{CNT} is the C_{sp} of the fFWNTs , wt%(CNT) is the weight percentage of fFWNTs in the electrode and wt%(MnO_2) is the weight percentage of MnO_2. Based on our measurements, the C_{CNT} at different scan rates of 10, 50, 100, 250 and 500 mV/s are 67, 64, 61, 56 and 48 F/g, respectively.

The energy density and power density of the assembled symmetrical supercapacitor was evaluated by the galvanostatic charge-discharge technique conducted at 0.65 mA, 1.30 mA, 3.90 mA, 6.48 mA and 13.0 mA (Figure 4d and 4E in the main text). The energy density was calculated using:

$$E = \frac{1}{2}CV^2$$

where C is the specific capacitance of the full cell and V is the voltage difference between the voltage after the iR drop at the beginning of discharging and the voltage at the end of discharge. The power density was calculated using:

$$P = \frac{E}{t}$$

where E is the energy density and t is the corresponding discharge time in hours.

3.3 *Results and discussion*

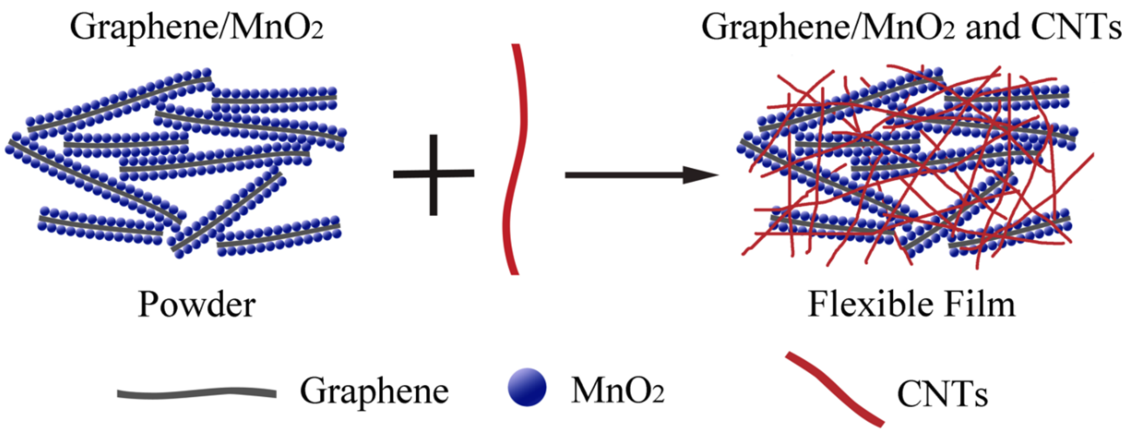

Figure 3.1: Schematic illustration of the fabricated flexible and conductive film using graphene/MnO_2 /CNTs. Note the difference in the possible electron paths for the two architectures: electron has to pass the insulating MnO_2 layers for the graphene/MnO_2 composite (left) while the interconnected CNTs provide rapid electron conductance for the flexible film shown on the right.

Herein, we present a method for fabricating compact, flexible and mechanical robust films for supercapacitor electrodes with excellent electrochemical performance based on the interpenetrative nanocomposites of graphene/MnO_2 and CNTs (Figure 3.1). The key difference of this new approach compared to early efforts is combing the synergistic effects from both graphene and nanotubes by using graphene as a high-surface area substrate for direct growth of MnO_2 nanoparticles and CNTs to provide electron conductance and mechanical reinforcement. Graphene has been widely considered as an ideal substrate for ultrathin coating of functional materials due to its unique structural and electrical properties[31], while interconnected CNTs network is highly conductive and porous and therefore beneficial for electronic and ionic transport. In early approaches, it was discovered that direct growth of MnO_2 nanoparticles on graphene or nanotubes is a critical factor to improve the performance of the composite films.[63, 115-117] Physical mixing of MnO_2 and carbon materials, on the other hand, could not fully capture the properties of the nanotubes and graphene due to aggregation, phase separation and poor connectivity between metal oxide and carbon. However, composite films made from MnO_2 directly grown on CNTs or graphene still have limited performance because the conductivity of the film is significantly reduced due to the disruption of the carbon-carbon conductive network (Figure 3.1) by the metal oxide coating. As a result, electrodes based on such architecture still suffer from low mass loading densities[92, 109] or require substantial amounts of conductive additives[118, 119] in order to achieve the desired performance. Recently, Yu et al. developed a surface warping technique using CNTs or conducting polymers to improve the conductivity of their electrodes.[114] However, the distribution of conducting additives in the electrodes is not homogenous and thus the improvement is limited. Recent reviews summarize various effects of nanotubes and graphene on energy storage when they are used individually with oxide materials.[51, 116]

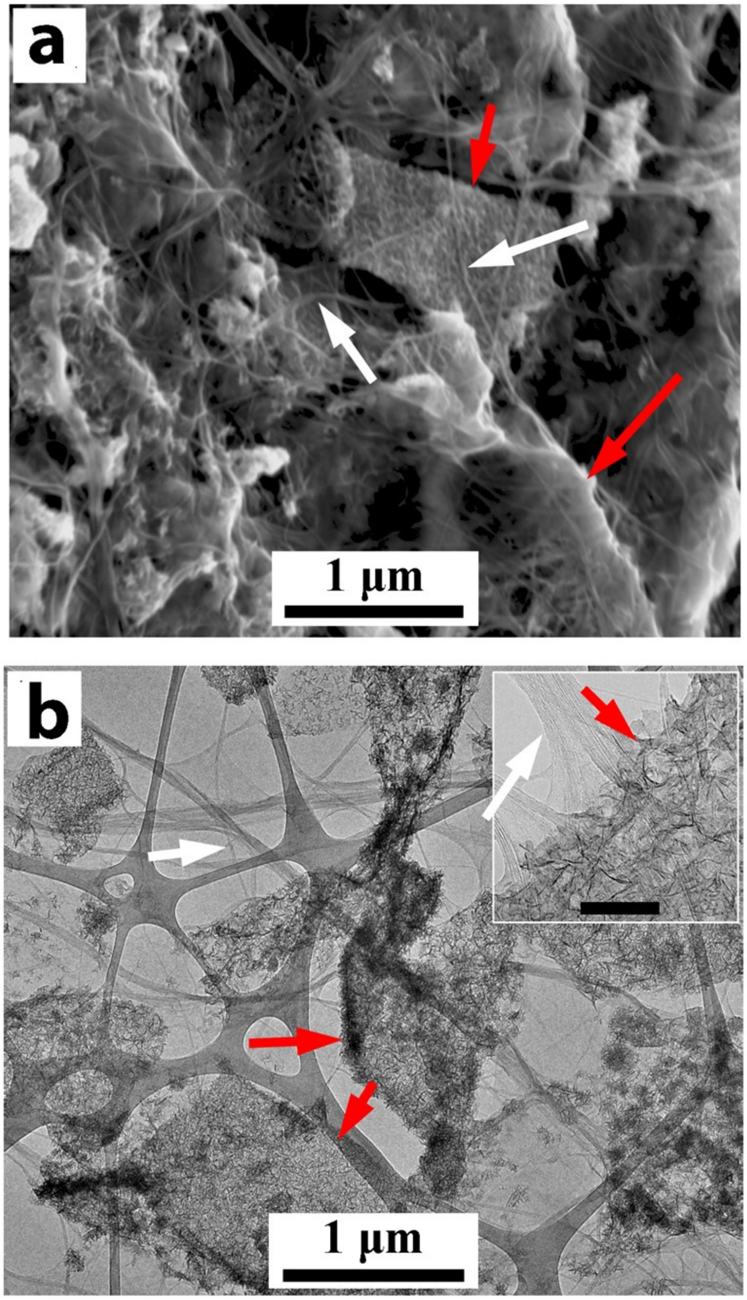

Figure 3.2: (a) SEM and (b) TEM images of the interconnected structure formed by graphene/MnO_2 composite (red arrows) and fFWNTs (white arrows), the inserted image shown in (b) highlight their close interaction.

In our designed architecture (Figure 3.1), a key requirement for the nanotubes is that they are not coated with MnO_2, thus allowing them to form a complete and highly conductive network with the graphene/MnO_2 composite. The nanotubes that we used are functionalized few-walled CNTs (fFWNTs) with 3~5 walls and they have better electric conductivity and mechanical strength compared with other types of nanotubes.[17] To prepare the designed ternary composite, a binary graphene/MnO_2 composite is first synthesized using a sonication-assisted chemical co-precipitation method. The high surface area graphene ensures ultrathin MnO_2 coating with high mass content in the composite (75wt%). Afterward, desired amounts of fFWNTs suspension and graphene/MnO_2 dispersion are mixed and sonicated for 20 min to ensure good mixing. The SEM (Figure 3.2a) and TEM (Figure 3.2b) images taken from this mixture reveal that they are well linked, with CNTs (white arrows) distributed uniformly in the matrix of graphene/MnO_2 composite (red arrows). The mixed solution was then vacuum-filtered and a freestanding film would form after vacuum drying (Figure 3.3a). In strong contrast, the composite of graphene/MnO_2 without fFWNTs did not form a continuous film on the filter membrane (Figure 3.3b). Thus, the incorporation of nanotubes is critical to the formation of a flexible film.

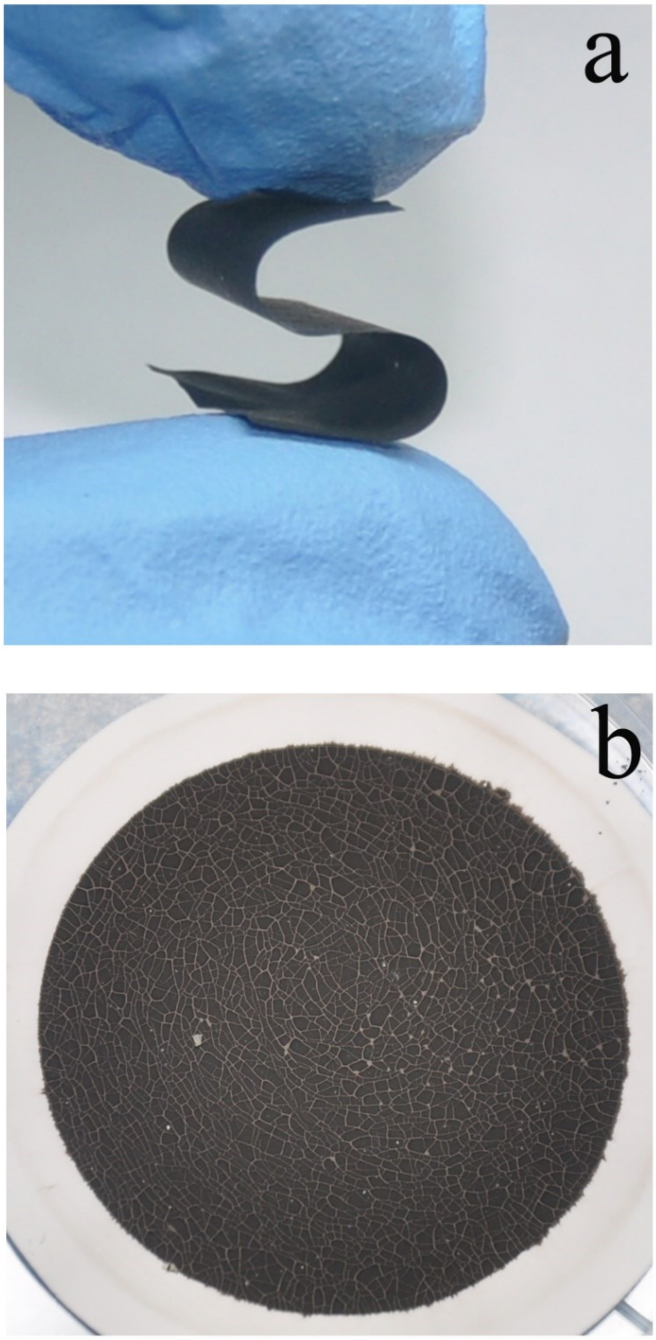

Figure 3.3: Digital images of (a) a graphene/MnO_2/CNTs flexible film and (b) a graphene/MnO_2 composite dried on a filtration membrane.

Systematic experiments with varing ratios of fFWNTs in the film indicated that as little as 5wt% of nanotubes could enable the composite to form a flexible film (with 71wt% of MnO_2). However, at least 25wt% of CNTs is needed in order to render the film highly flexible and mechanically robust. In fact, a tensile strength test from a 30μm film prepared with 25wt% of nanotubes (~56wt% of MnO_2) revealed a Young's modulus of 2.3 GPa and a tensile strength of 48 MPa (Figure 3.4), demonstrating its superior mechanical properties. More importantly, the active material loading of these flexible films is also significantly higher than the literature value for the flexible films containing metal oxide.[120] Additionally, the film is compact and has the density around 0.67 g/cm^3, which is twice higher than the films made by traditional carbon electrodes.[75] Finally, the incorporation of fFWNTs also brought superior electronic conductivity. Four Probe measurements indicated the sheet resistance of the flexible films is typically ~5 Ω/□ (67 S/cm).

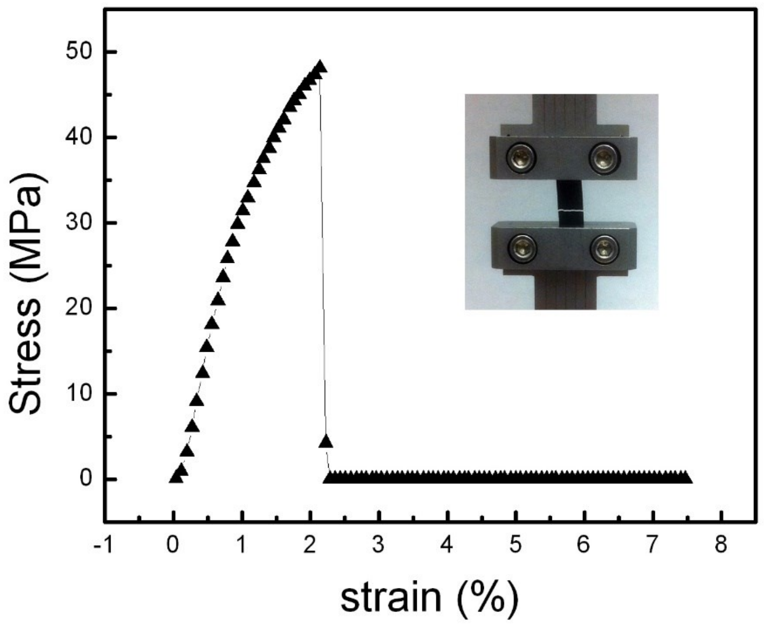

Figure 3.4: Typical stress-strain curve for a graphene/MnO_2/CNT composite film with 25wt% of fFWNTs.

The electrochemical performance of the flexible film was first examined using the CV method in 1 M Na_2SO_4. All of the films that were reported herein had the same composition of 25wt% of fFWNTs and 75wt% of graphene/MnO_2 composite. No metal support or current collector was used in the test and the film was directly attached to a metal clip for electrical connection. Figure 3.5 a and b show a set of rate-dependent CV curves acquired from the film electrode (30 μm, 2.02 mg/cm^2) at scan rates up to 500 mV/s within 0.0~1.0V voltage window.

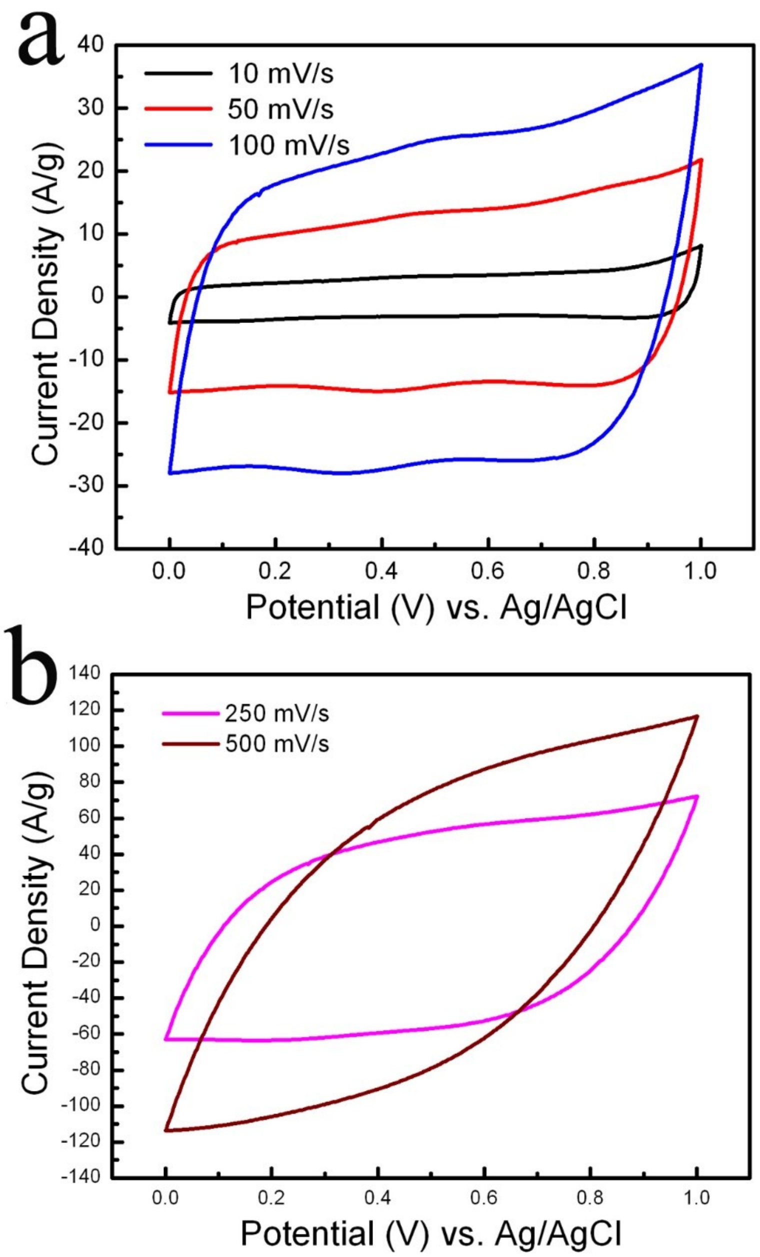

Figure 3.5 (a) and (b) CV curves for a 30 μm flexible film (2.02 mg/cm^2) acquired at different scan rates.

It can be seen that these curves have nearly ideal rectangular shapes, indicating superior supercapacitor behavior even at such high areal density. The combined contribution from graphene and fFWNTs ensures MnO_2 to have only ~55% capacitance loss (326 F/g to 148 F/g) when the scan rate was increased from 10 mV/s to 500 mV/s, which is much better compared to previous reports at similar mass densities.[115] More importantly, these results are obtained from a thick film with high MnO_2 content (56 wt%). Films with lower MnO_2 content or thinner thickness (< 5 μm) would have much better performance (372 F/g at ~0.4 mg/cm^2). Results from thick films are reported here because they are more amenable to real commercial manufacturing. Furthermore, the calculated volumetric capacitance of 130 F/cm^3 is also much higher than previous reports, [94] which indicates that such flexible electrodes are also promising for compact energy storage systems.

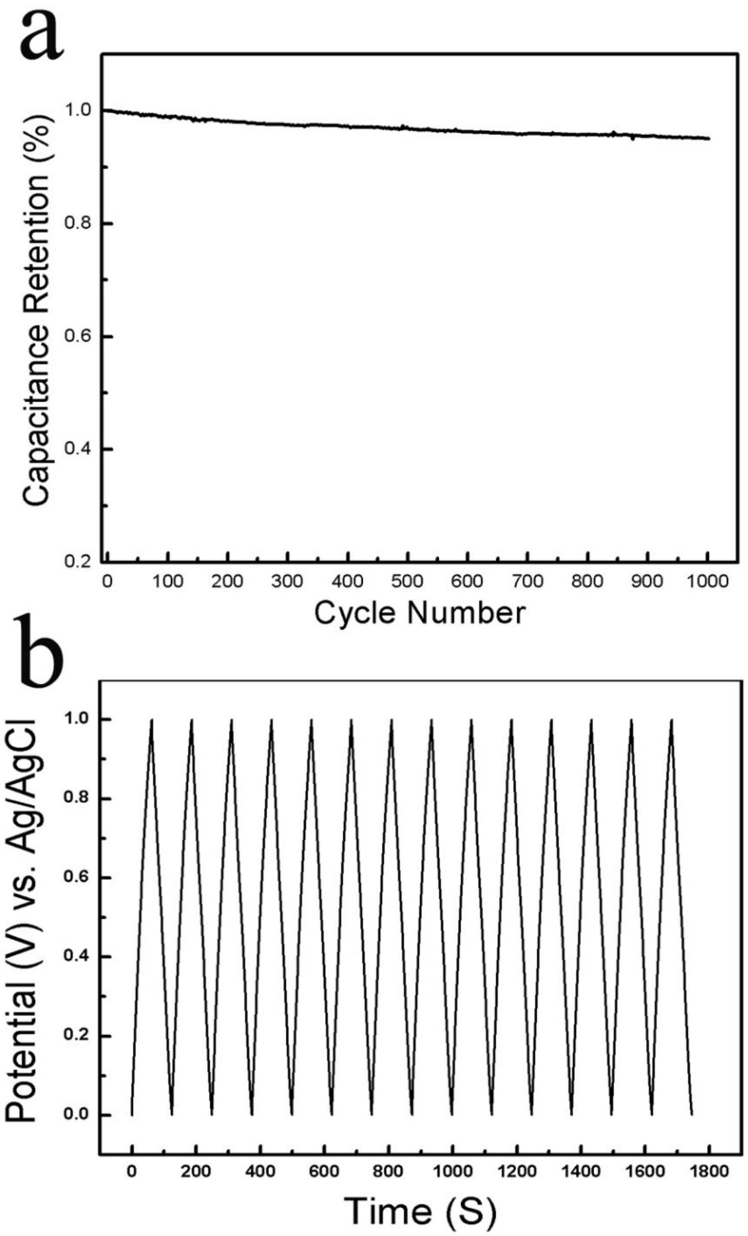

Figure 3.6: (a) Capacitance retention of the film electrode at 4 A/g over 1000 cycles and (b) typical charge-discharge profile.

The cycle-stability of the flexible film was evaluated using the galvanostatic charge-discharge technique conducted at 4 A/g (Figure 3.6). The film shows ~5% of capacitance loss after 1000 cycles, revealing its outstanding electrochemical stability.

Figure 3.7a compares the CV curves acquired at the same scan rate of 50 mV/s from films with different areal densities. As this figure shows, the curves show slight distortion as the film gets thicker and the *SC* of MnO_2 drops only by 38% (312 F/g to 194 F/g, Figure 3.7b) as the areal density increases from 0.38 mg/cm^2 to 8.80 mg/cm^2. In contrast, the graphene/MnO_2 composite exhibits significant thickness-dependence in performance, as its electroactivity decreases rapidly as the thickness is increased (decrease from 288 F/g at 0.4 mg/cm^2 to 130 F/g at 2.1 mg/cm^2, Figure 3.7b).

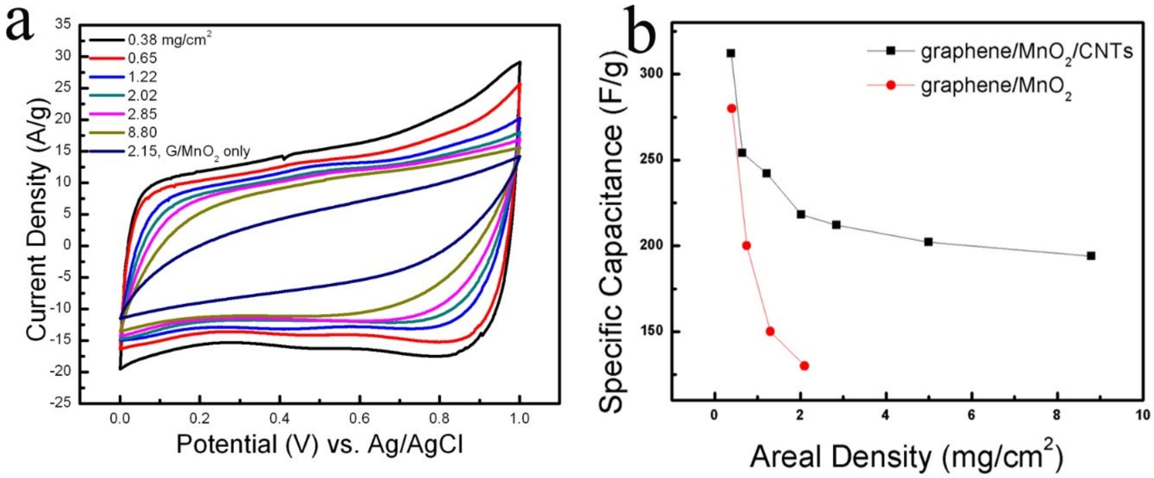

Figure 3.7: (a) Comparison of the CV curves acquired at 50 mV/s for flexible films with different areal densities and (b) comparison of the SC of flexible graphene/MnO_2/CNTs films and graphene/MnO_2 electrodes at different areal densities at 50 mV/s.

The improved conductivity by fFWNTs also significantly boosted the rate-capability of the flexible film. As discussed previously, the electrodes with fFWNTs deliver 148 F/g at 500 mV/s, 45% of the available capacitance at 10 mV/s. In contrast, an electrode made from graphene/MnO_2 composite supported on a gold electrode at similar areal density only retains 10%, with 90% of available capacitance at 10 mV/s lost at 500 mV/s (Figure 3.8). It is believed that such a strong difference is due to the homogeneous incorporation of highly conductive fFWNTs in the graphene/MnO_2 composites. The formation of uniform films rather than phase separated nonuniform films is the key reason for observing high performance in our measurement. We propose this is mainly due to the synergistic effects from graphene and nanotubes, since it is well known that graphene can be a good surfactant to disperse nanotubes in aqueous solutions.[121] In our system, graphene serves as the connecter between the metal oxide, which prefers to attach to the defect sites on the graphene, and the nanotubes, which prefer to attach to the graphitic part of the graphene.

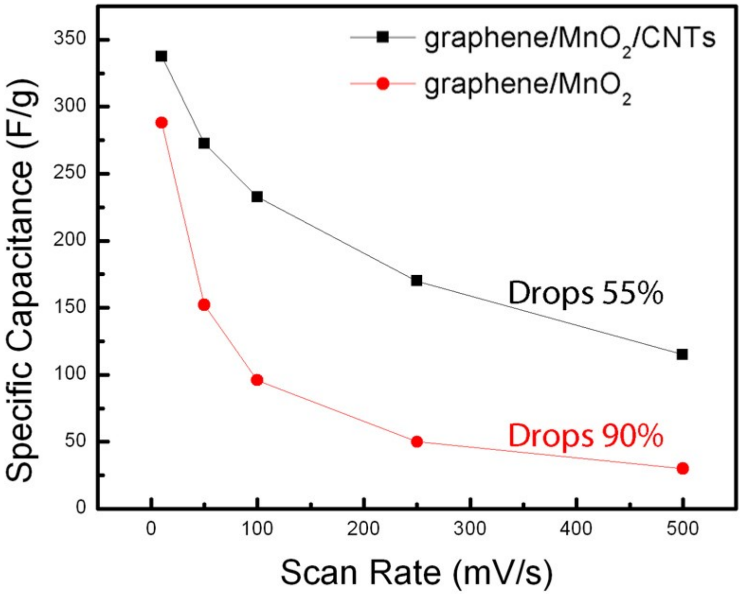

Figure 3.8: Comparison of the *SC* of MnO_2 measured at increasing scan rates for flexible films and graphene/MnO_2 electrodes fabricated at similar areal densities around 2 mg/cm^2.

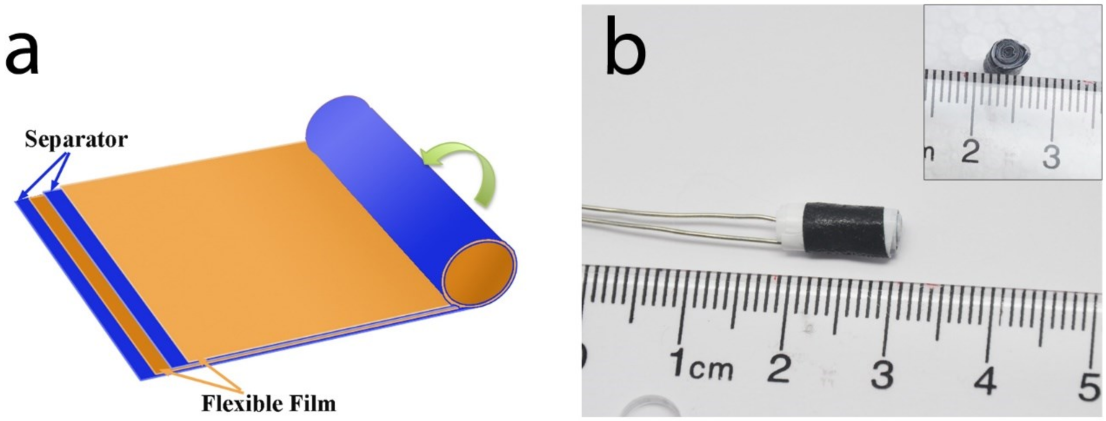

Figure 3.9 (a) Schematic illustration of the fabrication process to make a full cell using the flexible film. (b) Digital image of the actual compact full cell (insert: cross-sectional image), the superior mechanical strength and flexibility of the electrodes ensure rolling around a platinum wire (0.5 mm diameter) without losing their electroactivity.

To further examine the performance of our flexible films as supercapcitor electrodes, a rod-shaped capacitor was assembled by rolling up two films with identical composition (3.2 mg, 2.02 mg/cm^2) that were separated by the separator (Celgard 3501) (Figure 3.9 a and b). Owing to the highly flexible nature of these electrodes, they can be wrapped around a 0.5 mm Pt wire without any observable change in their electrochemical properties and mechanical strength, indicating a significant improvement in their mechanical stability. Such roll-up approach also offers higher volumetric capacity compared with the stack design and thus is promising for fabricating high-capacitance and small-size power devices.[63, 122] The CV curves acquired from the full cell at increasing scan rates from 10 mV/s to 100 mV/s (Figure 3.10a) show nearly ideal rectangular shapes, further demonstrated the excellent capacitive characteristics and ultrafast response of the flexible films. Based on the analysis of the CV curves, the full cell has the *SC* of 70 F/g at 10 mV/s (based on both electrodes) that corresponding to 280 F/g if measured in a three electrode testing system.[123] More significantly, 65% of the available capacitance obtained at 10 mV/s was retained at the high scan rate of 100 mV/s (SC: 45 F/g), which is also higher than most of the previous results.[113]

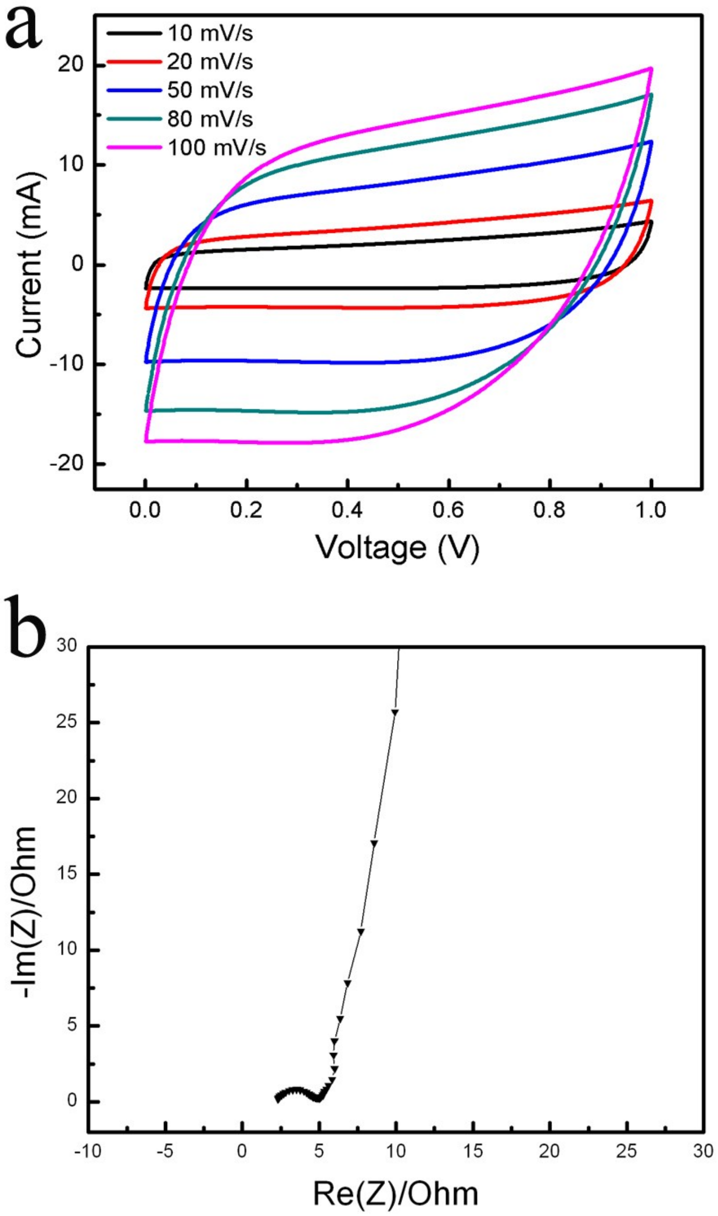

Figure 3.10: (a) CV curves of the full cell acquired at different scan rates between 0.0~1.0 V. (b) Electrochemical impedance spectrum of the full cell.

The impedance spectrum acquired is shown as the Nyquist plot in Figure 3.5e, which exhibits a typical arc at the high frequency region and a spike at the low frequency region. The equivalent series resistance of the assembled cell is ~2.4 Ω, which is similar or lower than the reported values.[63, 113, 124, 125] It is also noticeable that the Nyquist plot shows an almost vertical line at lower frequencies, indicating highly capacitive behavior[126] and superior performance of the flexible film under high mass densities.

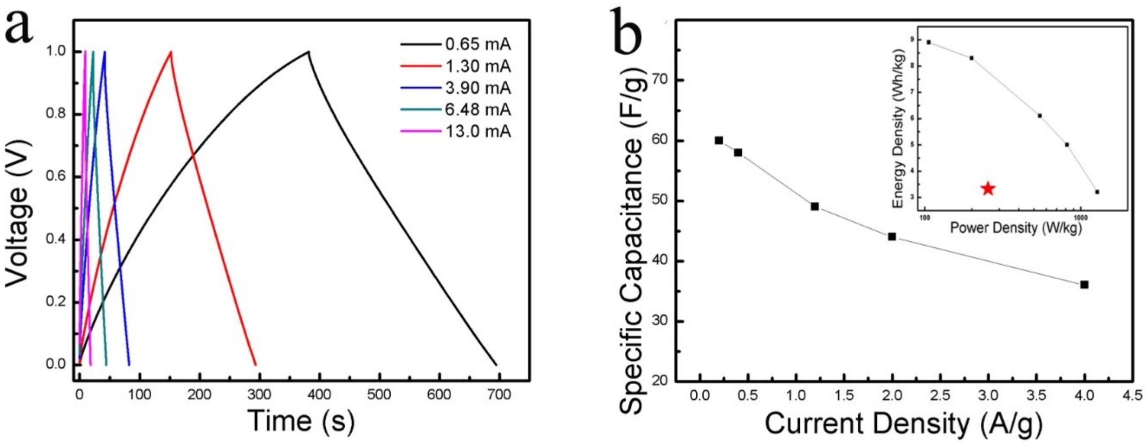

Figure 3.11: (a) Galvanostatic charge-discharge curves acquired at different currents and (b) specific capacitance (based on both electrodes) at different current density and the Regone plot for the fabricated cell (inserted).

The voltage versus time profiles obtained by the galvanostatic charge-discharge technique conducted at different currents (Figure 3.11a) show highly linear behavior and nearly symmetrical shape that also proved ideal capacitive behavior of our cell. On the basis of the galvanostatic charge-discharge results, the specific capacitance, as well as the energy densities and power densities, of the full cell were calculated (Figure 3.11b). The cell delivers 8.9 Wh/kg at the power density of 106 W/kg and 3.2 Wh/kg at 1.28 KW/kg. Using the method described by Fan et al.[126], the maximum power density of our assembled full cell is 170 kW/kg. Comparing such performance metrics with the MnO_2

symmetric supercapacitor (red star, Figure 3.11b) fabricated using the traditional approach by mixing MnO_2 (65wt%), conductive carbon (30wt%) and binder (5wt%),[127] our graphene and CNTs based flexible cell has noticeably higher power density and energy density. Such improved performance is likely due to the improved conductivity of the whole electrode by the interconnected CNTs and the ultrathin MnO_2 coatings enabled by graphene that improved overall electrochemical efficiency. When considering all the components of the packaged cell,[75] the estimated maximum energy density and power density of the assembled cell are 2.2 Wh/kg and 42 kW/kg, respectively. Since the mechanically strong film did not require any heavy current collector (for example, ~ 5 mg/cm^2 for Al foil) or binder to operate, our approach has the potential to further improving the device performance metric with optimized cell assembly. Besides, significant improvement regarding the energy density could be realized by using the asymmetrical supercapacitor design.[35]

3.4 Conclusion

In conclusion, a method to fabricate highly flexible, robust film with superior conductance based on interconnected graphene/MnO_2/CNTs nanocomposite for supercapcitor electrode was developed. The highly conductive architecture in such films enables efficient charge transport and electrode integrity, endowing the films with high capacity, superb rate-capability and stable specific capacitance in a large range of areal densities. The flexible film also enables the fabrication of a high performance full cell using the rolled-up approach without metal current collectors and binders that could reduce both the weight and volume of the supercapacitors. These results suggest that flexible and robust films enabled by the synergistic effects from CNTs and graphene could have significant potential as electrode materials for wearable and lightweight energy storage devices. We also foresee that this design concept could be readily applicable other electrochemical materials containing metal oxides for energy storage systems, bringing new opportunities for a wide range of applications.

Chapter 4: Flexible Asymmetric Supercapacitors with High Energy and High Power Density in Aqueous Electrolytes[*]

4.1 Introduction

Supercapacitors are considered to be promising devices to combine with energy-dense but power-limited components (such as batteries and combustion engines) to meet the rigorous energy requirements.[49] However, a major drawback of supercapacitors is that they have limited energy density.[10] Recently, tremendous research efforts have been devoted to improving their energy density while preserving high power density.[40, 58, 63] Technically, enhancements of energy densities (E) can be achieved by increasing either specific capacitance or operation voltage[128]. Conventionally, high energy density supercapacitors are usually realized by using nonaqueous electrolytes that can operate at ~3 V with electrodes that are made of high surface area and lightweight materials such as activated carbon.[46] However, such systems usually have low capacitive and power capabilities because of limited ionic concentration and conductivity in organic electrolytes.[128] On the other hand, aqueous-based electrolytes offer ions of smaller size, higher ionic concentration and higher mobility than nonaqueous electrolytes and thus could facilitate high power operation. They also have added advantages of low cost and enhanced safety in operation.[35]

---

[*] This chapter has been published in Cheng et al. ***Nanoscale***, 2013, 5, 1067-1073.

However, water-based electrolytes can only be operated within 1.2 V due to the electrochemical instability of water when identical materials are used as positive and negative electrodes[69]. To extend the operating voltage, ASC based on different electrode materials that have high over potentials for O_2 and H_2 evolution have been designed and studied extensively.[129] Using this design, the voltage of assembled supercapacitors can be effectively extended beyond 1.2 V, leading to significantly increased energy density.[130]

Several combinations of materials, such as $Ni(OH)_2/RuO_2$,[131] $Ni(OH)_2$/Activated Carbon (AC)[132] and MnO_2/AC[127, 129, 133] have been studied for preparing ASC. Among these, the MnO_2/AC based system is particularly attractive as MnO_2 is naturally abundant, has low toxicity and can operate in neutral electrolytes with high theoretical *SC* up to~1300 F/g. AC is another widely used electrode material because of its high surface area.[42, 46] However, the poor conductivity of MnO_2 could significantly limit the overall power and energy densities of the fabricated devices.[65] Although promising energy densities of 10~28 Wh/kg have been demonstrated in various studies, such high values were obtained only under low power density conditions (100~500 W/kg) and they usually were found to decrease rapidly as the power density was increased. [83, 127-129, 134] Some of the recent studies on supercapacitors using ultrathin electrodes fabricated with either CNTs or graphene showed much improved results, but these electrodes are not suitable for practical applications[135] due to their very limited thickness of the electrodes.

On the other hand, only limited energy densities (< 10 Wh/kg) were obtained under high power conditions when thicker electrodes were used. For example, only 7.0 Wh/kg was retained at 5.0 kW/kg for a MnO_2/graphene system.[83] Considering the critical importance of high power density for supercapacitors, further improvements in the energy density under high power conditions are needed. Additionally, the conventional slurry casting approach of electrode fabrication needs conducting additives, binders and current collectors. As a result, this approach results in less than 30 wt% of the total electrode weight being electrochemically active and thus reduces the overall device-level performance metrics.[75] So there is a need for a novel process to prepare electrodes without binders and current collectors. In this chapter, a novel approach to fabricating binder free and current collector free, flexible, ASC with high power and energy densities is discussed.

Flexible energy storage systems have received intense research interest recently due to their significant potential applications in foldable displays and wearable electronics.[136] They also offer better manufacturability because they can be folded, twisted or cut to fit any desired spaces.[45] Although previous studies focused on designing flexible single electrodes have reported promising results, they either still require electrochemically inert flexible substrates,[136, 137] or have low electroactive material loading [74] with limited flexibility and mechanical strength.[138, 139] Thus, further advances toward fabricating flexible electrodes with high active material loading and improved mechanical strength are required. In the previous chapter we have identified that the synergistic effects from graphene and CNTs could enable highly flexible and mechanically strong electrode films with improved electrochemical activity.[76] However, the symmetric configuration used in that work resulted in limited overall energy and power density. The aim of this project is to improve the power and energy density of SCs by using an asymmetric configuration.

In this current system, the fundamental building blocks for the flexible ASC are MnO_2 nanoparticles, AC, RGO and fFWNTs. Ternary composites of RGO/MnO_2/fFWNTs were used as the positive electrodes and the AC/fFWNTs composite were used as the negative electrodes. Combining the unique properties of each functional material, the present strategy enables practical thick electrodes with superior mechanical strength, excellent conductivity and high electroactive material loading. Using these flexible films as electrodes, ASC with high energy density (24 Wh/kg) under a high power density of 7.8 kW/kg were fabricated employing a roll-up approach. These features are very attractive for a variety of critical applications, such as the power sources in hybrid electric vehicles or back-up power for wind and solar energy.

4.2 Experimental details

4.2.1 Material synthesis

RGO dispersion and RGO/MnO_2 composites were synthesized using the methods as described in Chapter 2. The synthesis, purification and functionalization of few-walled CNTs were also same as described in Chapter 2.[140] An appropriate amount of the prepared fFWNTs dispersion was added to the RGO/MnO_2 suspension (for the positive electrode) or activated carbon (for the negative electrode) dispersion and sonicated for 20 min to ensure a good mixture of the constituents. The mixed solution was then filtered through a filtration membrane (Millipore, 1.2 μm) and a flexible film was obtained after 24 hours of vacuum drying at room temperature of the filter cake. The dried flexible films were then used as electrodes for the supercapacitors assembly and characterization.

4.2.2 Characterization

Material characterization is the same as described in 2.2.

4.2.3 Electrochemical measurements

The methods for electrochemical measurements were the same as described in Chapter 2. The properties of different flexible electrodes were measured using CV at different scan rates. ASCs were assembled by rolling up the stacked flexible films for the positive and negative electrodes that were separated by separators (Celgard 2501). Two platinum wires were used to connect flexible films to an external measurement circuit. After assembling the components, a carbon tape was used to hold the structure together. The whole cell was then immersed in 1M Na_2SO_4 electrolyte for the electrochemical measurements.

The capacitance C of the ASC was calculated using the following equation on the basis of the galvanostatic charge/discharge data:

$$C = i/-[\Delta V/\Delta t]$$

where i is the current applied, and $\Delta V/\Delta t$ is the slope of the discharge curve after the iR drop. The calculations of energy and power densities were the same as described in Chapter 3.

As for a full supercapacitor, the balance of the charge flow between the positive electrode and the negative electrode is critical for optimum performance (i.e. $q_+ = q_-$). The charge stored by each electrode depends on its specific capacitance (C_{sp}), the potential range of the charge/discharge process (ΔE) and the mass of the electrode (m) following the Equation:

$$q = C_{sp} * \Delta E * m$$

and in order to get equal charge flow ($q_+ = q_-$), the mass ratio between the positive and negative electrodes needs to follow:

$$\frac{m_+}{m_-} = \frac{C_- * \ \Delta E_-}{C_+ * \ \Delta E_+}$$

On the basis of the specific capacitance values and potential windows found for the flexible graphene/MnO_2/CNTs electrode and the AC/CNTs, the optimal mass ratio between these two electrodes was determined to be as 0.65 for the flexible ASC. Prior to testing, both electrodes were polarized to 0.0 V vs. the Ag/AgCl (4M KCl) reference electrode for 30 min.

4.3 Results and discussion

In this project, RGO/MnO_2/fFWNTs flexible films were used as the positive electrodes and flexible films made with activated carbon (AC)/ fFWNTs were used as the negative electrodes for the fabrication of ASC. The properties of the flexible RGO/MnO_2/fFWNTs electrodes have been described in Chapter 3 and thus are not discussed in detail in this Chapter. During the AC/fFWNTs electrode preparation process, the sonication step is critical to enhance mixing as AC particles were found to be well connected by nanotubes as shown in a TEM image (Figure 4.1a) of the composite. An SEM image (Figure 4.1b) taken from a dried film also revealed that fFWNTs were distributed homogeneously in the film over large area and were connected well to the AC particles.

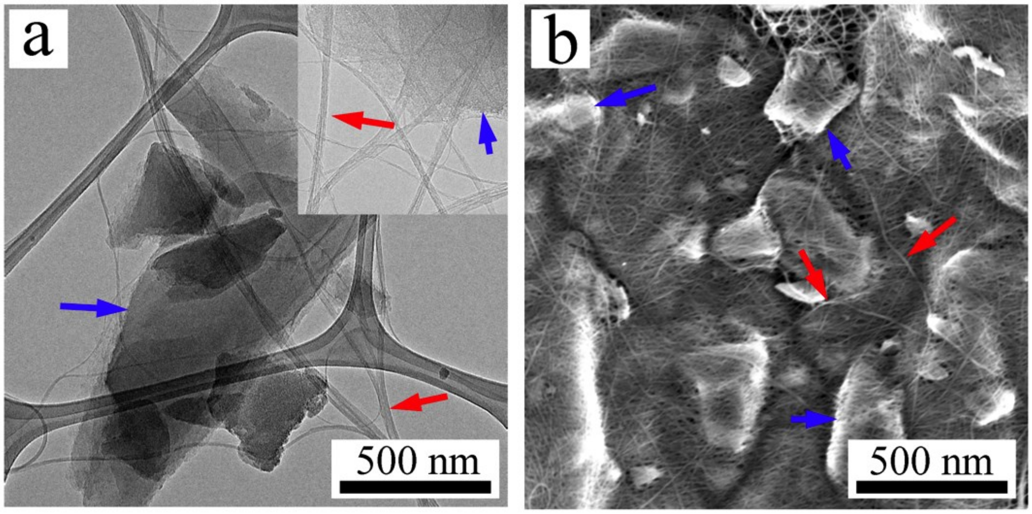

Figure 4.1 a) TEM and b) SEM images of the fFWNTs (red arrows)/AC (blue arrows) composite showing that nanotubes were distributed uniformly in the composite and were connected to AC particles, the inserted image in (a) is a high resolution TEM image that highlights their close interaction.

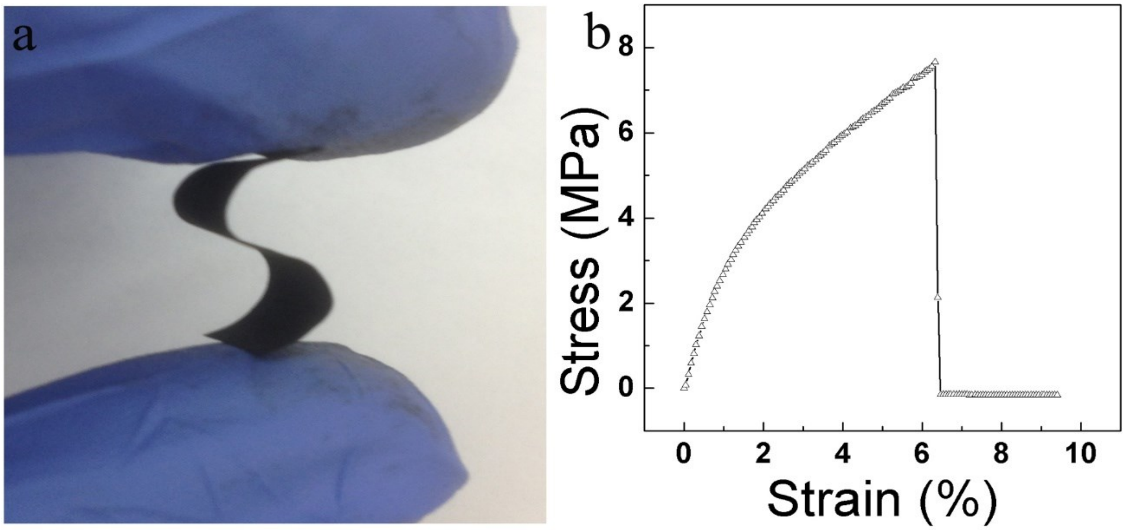

Figure 4.2: (a) Digital image of a flexible film (1 cm × 2 cm) held between two fingers and (b) a typical stress-stain curve of the film.

With the addition of ultra-long and strong fFWNTs, the composite electrodes showed high flexibility (Figure 4.2a). Mechanical property characterization of the samples indicated that these films (~ 100 μm thick, with a density of 3 mg/cm^2) have Young's Modulus of 0.1 GPa and tensile strength of 7.5 MPa (Figure 4.2b). Additionally, the mechanical strength of the films improved as the CNT amount was increased (Figure 4.3). However, 20 wt% was identified as the optimum percentage for practical considerations as nanotubes are more expensive than AC, and also in light of the overall specific capacitance as discussed below and shown in Figure 4.3

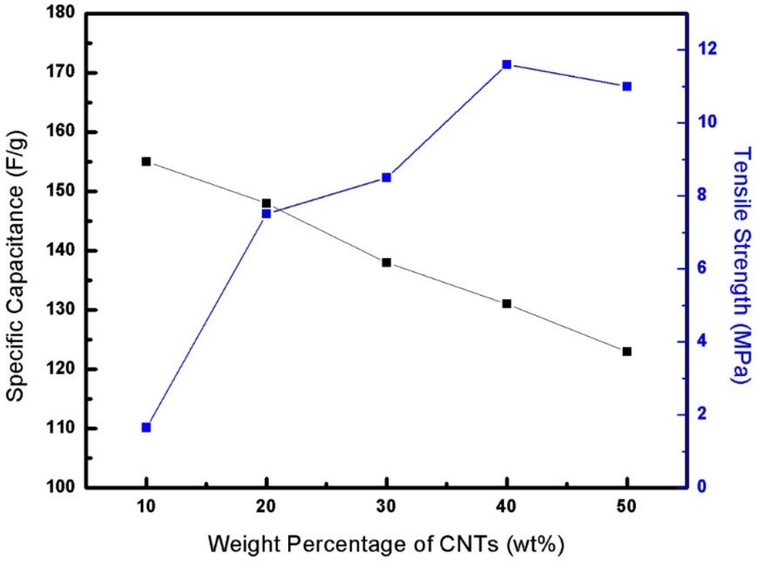

Figure 4.3: Comparison of the specific capacitance and tensile strength of flexible films made with different weight percentage of CNTs.

Prior to the fabrication of ASC, the electrochemical properties of flexible AC/fFWNT electrodes were first investigated by CV. It has been reported that CNTs are able to substantially improve the capacitive behavior of AC.[141] However, little effort has been made towards the fabrication of flexible and current collector free electrodes. With the addition of fFWNTs, the flexible electrodes showed improved capacitive behavior within -1.0~0.2 V versus the reference electrode in 1 M Na_2SO_4. Despite AC has higher capacitance in KOH,[142] a neutral electrolyte of Na_2SO_4 is used in the present study for its environmental friendliness and compatibility with MnO_2. The CV curves (Figure 4.4a) have nearly rectangular shapes without noticeable redox peaks, indicating ideal double layer charge storage property. The specific capacitances calculated are 203, 185, 163, 147 and 105 F/g at the scan rate of 2, 10, 50, 100 and 250 mV/s respectively.

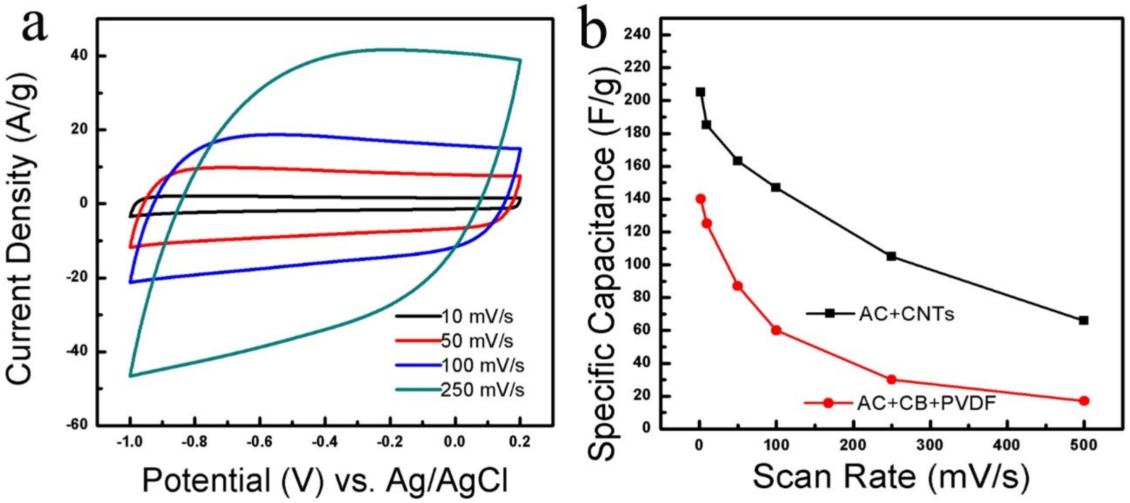

Figure 4.4: (a) A set of CV curves for the fFWNT/AC flexible electrode measured at increasing scan rates in -1.0~0.2 V (vs. Ag/AgCl (4M KCl)); (b) Comparison of the specific capacitance measured at different scan rates for a flexible AC/fFWNT electrode fabricated with 20 wt% of CNTs and an electrode made with the traditional approach of mixing AC (70wt%) with carbon black (20wt%) and PVDF (10 wt%).

Compared with electrodes fabricated using the traditional approach, such nanotube enabled flexible AC electrodes have significantly higher capacitance value (141 F/g at 10 mV/s, Figure 4.4b) and rate performance. The improvement is likely due to facilitated electronic and ionic transport in porous flexible electrodes incorporated with CNTs. At a high scan rate of 500 mV/s, the CV curve exhibits obvious distortion from the ideal rectangular shape and only has 66 F/g. The lower rate capability of AC/fFWNT electrodes (32% of the capacitance measured at 10 mV/s retained at 500 mV/s) as compared with positive RGO/MnO_2/fFWNTs electrodes (45%) might originate from intrinsic properties of AC, such as low conductivity and micro-porosity that are usually inaccessible for ions[143]. Nevertheless, increasing the amount of nanotubes improved the electronic conductivity of the film and thus lead to better rate capability. However, the available capacitance is compromised since low surface area fFWNTs have limited contribution to the whole composite (Figure 4.3). As a result, AC/fFWNT electrodes with 20 wt% of fFWNTs were used in this project.

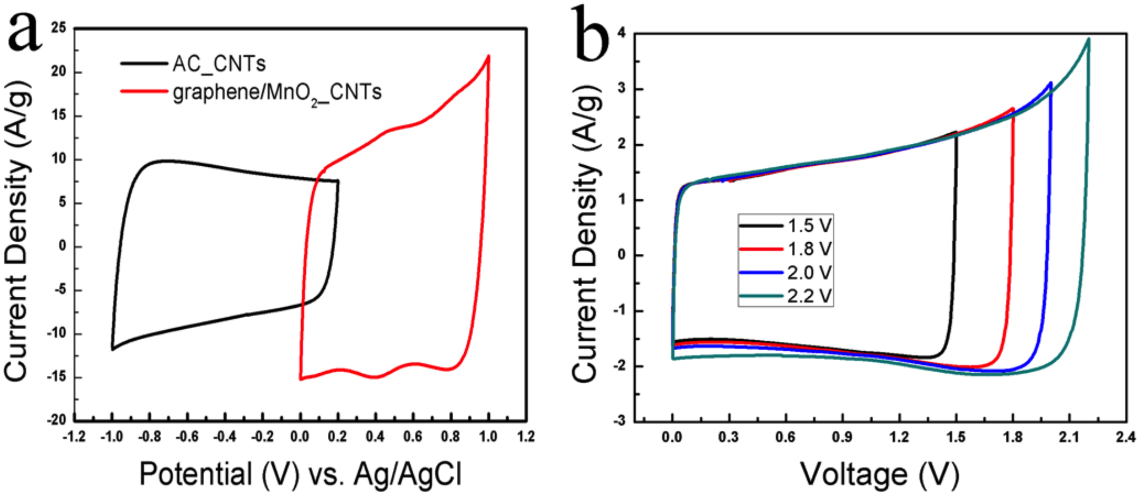

Figure 4.5 Comparative CV curves of the flexible ternary RGO/MnO_2/fFWNTs and flexible AC/fFWNTs electrodes measured at 50 mV/s. b) CV curves of an optimized ASC measured at different voltage windows at a scan rate of 20 mV/s.

On the basis of the operating voltage window determined by the CV measurements (Figure 4.5a), an ASC assembled with flexible RGO/MnO_2/fFWNTs and AC/fFWNTs electrodes are expected to have stable working voltage of 2 V in 1M Na_2SO_4. To ensure full charge storage of the two electrodes, their masses were optimized according to their specific capacitance and operating voltage window.[142] Figure 4.5b shows the CV curves of an optimized device acquired with different voltage windows measured at a scan rate of 20 mV/s. As expected, the assembled cell showed ideal capacitive behavior with rectangular CV curves at voltages up to 2.0V. At voltages beyond 2.0 V the cell exhibited a sharp increase in the response current that was probably related with gases (such as O_2 and H_2) formation on the electrode(s) and thus would be unsafe for regular operation. Noticeably, compared with CV results obtained from the ASC assembled using traditional approach,[83, 128] the CV curves of the flexible supercapacitor reported herein are closer to the ideal rectangular shape and thus indicate reduced charge transfer resistance and improved capacitive characteristics due to the unique nanocomposite structure of the electrodes.

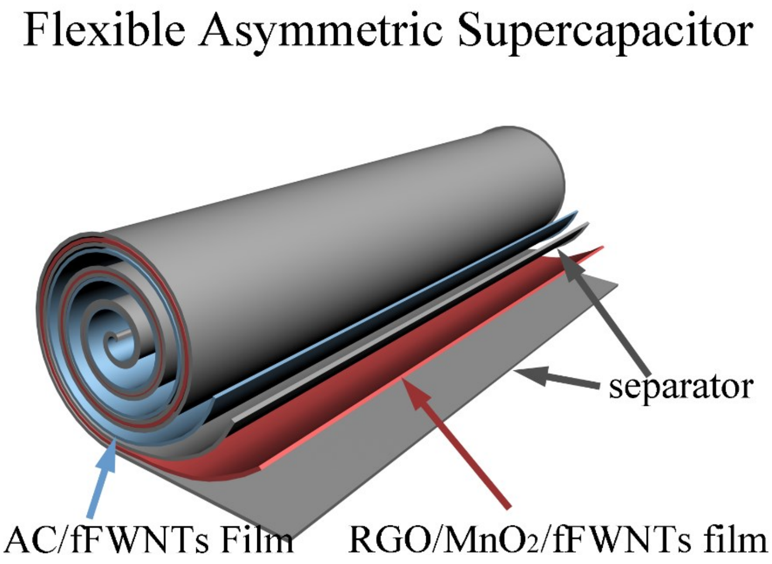

Figure 4.6: Schematic illustration of the assembly process of a flexible ASC using the roll-up approach.

Thanks to the superior mechanical strength, flexibility and electronic conductivity of both flexible electrodes, ASC were fabricated using a roll-up approach without any mechanical support or current collectors as illustrated in Figure 4.6. The roll-up approach, compared with the stack-up method, offers higher volumetric capacitance and thus is a promising approach for making compact and high performance energy storage devices.[122]

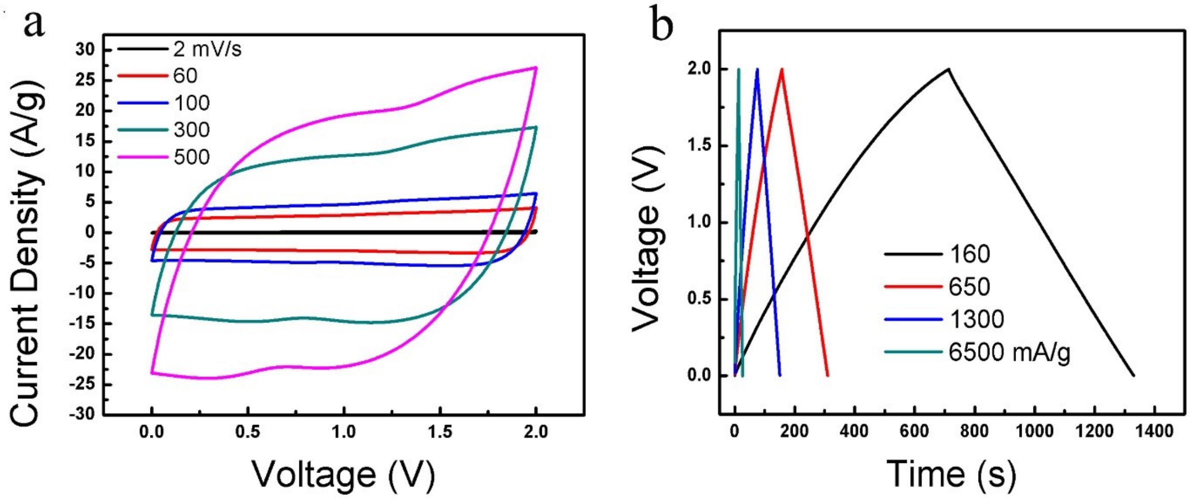

Figure 4.7: a) CV curves of the ASC acquired at increasing scan rates from 2mV/s to 500 mV/s in 1 M Na_2SO_4; b) Galvanostatic charge-discharge curves obtained under different current densities.

Figure 4.7a and b present the electrochemical characterization results for capacitors fabricated using the roll-up approach. The CV curves (Figure 4.7a) acquired within 2V exhibit typical rectangular shape without obvious redox peaks, indicating ideal capacitive behavior. More remarkably, the CV curve still retains the rectangular profile without significant distortion even at a high scan rate of 500 mV/s. In strong contrast, a capacitor fabricated using the same electroactive material but with the traditional approach, exhibited significantly distorted CV curves under the same testing condition at high scan rates (Figure 4.8), highlighting the critical role of CNTs on improving their rate performance as practical thick films. On the basis of the CV results, the SC of the ASC was calculated using the total mass of the materials from both electrodes, rather than of a single electrode. Even though calculations based on a single electrode yield much higher results (four times higher than two electrodes), such an approach should not be used to predict the device-level performance metrics as being noted recently.[35, 75] Nevertheless, the assembled cell delivered 46 F/g at 2 mV/s and still kept 36 F/g at a high scan rate of 500 mV/s (78% retention). Compared with the capacitance retention ratios of ASC assembled in earlier studies, such as graphene/MnO_2//ACN a (~30%),[142] the device studied here has noticeably higher capacitance retention ratio and thus better power capabilities.

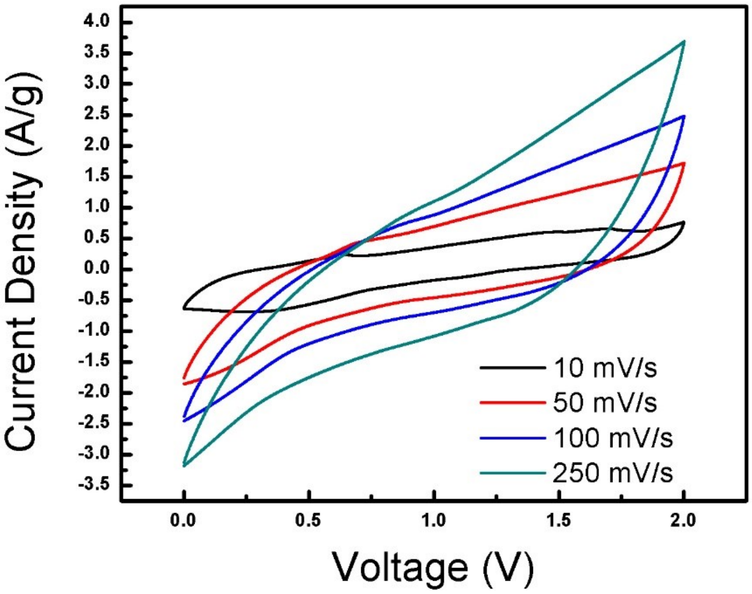

Figure 4.8 Characterization of the ASC using electrodes fabricated by the conventional method. Both positive and negative electrode were fabricated casting the slurry of active materials (70 wt%), carbon black (20 wt%) and PVDF (10 wt%) on Ni foam.

Galvanostatic charge-discharge technique was used to further evaluate the performance of the assembled ASC and the results were plotted in Figure 4.7b. As can be seen, the ASC showed typical triangular-shaped and symmetrical charge-discharge curves at various current densities ranging from 0.16 A/g to 6.4 A/g. The charge and discharge profiles were almost all linear in shape, corresponding to the behavior of ideal capacitors agreeing well with CV results. The columbic efficiencies were all almost 100% under the various current densities being tested, indicating a highly efficient device. On the basis of the charge-discharge tests results, the energy densities and the power densities of the assembled capacitor were calculated and the results are summarized as the Ragone plot in Figure 4.9. The energy density of the device was found to be 27 Wh/kg at a power density of 130 W/kg and reduced slowly as the power density was increased. At a high power density of 7.8 kW/kg, the energy density was still 23.9 Wh/kg (89% retention), further proving the superior power capability of the CNTs based flexible SC. Noticeably, the obtained energy density is significantly higher than the symmetrical supercapacitors such as AC//AC capacitor (~10 Wh/kg)[143], MnO_2//MnO_2 capacitor (~ 3 Wh/kg)[127] and also higher than the ASC of graphene/MnO_2//CNT textiles (12.5 Wh/kg)[65] and MnO_2//AC (10 Wh/kg)[133]. Even though the energy density is comparable to graphene/MnO_2//graphene SC (30 Wh/kg) [83] and MnO_2/graphene//graphene SC (28 Wh/kg) [144], the flexible ASC described herein is able to deliver much higher energy density under high power conditions. For example, the

MnO_2/graphene//graphene ASC only has 7 Wh/kg at the power density of 5 kW/kg (Fig. 4a). However, it should be noted that only reported results that were calculated using the same method were compared in this study, as different calculation methods would give diverse results.[35] Remarkably, the maximum energy density of the flexible ASC was estimated as 130 kW/kg using the method described by Fan et al. [142] Thus, besides the superior flexibility, such ASC is also able to achieve both high power and energy densities.

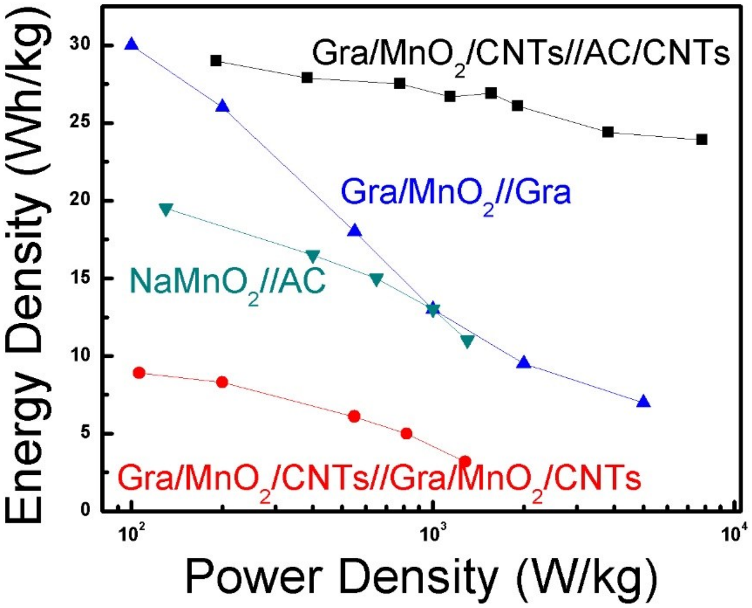

Figure 4.9: Comparison of the Ragone plots for flexible ASC assembled in this work, flexible symmetric RGO/MnO_2/CNTs//RGO/MnO_2/CNTs supercapacitor[76], $NaMnO_2$//AC ASC [134] and graphene/MnO_2// graphene ASC. [83]

The superior performance observed in the ASC could be attributed to the appropriate combination of each unique electrode materials: the atomic layer thick graphene flakes can ensure MnO_2 grow as nanoscale particles on their surfaces with excellent interfacial contact, which results in a binary composite with improved mechanical integrity and electrostability during charge-discharge cycles. The high surface area AC is favorable for the formation of double-layer charge storage on its surface with facilitated transport of electrolyte ions. The uncoated and functionalized CNTs can form interconnected conductive network that would further improve the conductivity of the fabricated electrodes. Besides forming a highly porous network, the nanotubes are also beneficial for ionic transport as well. Working together, the combined contribution from each components enable electrodes with greatly facilitated electron transport and shortened diffusion and migration paths of electrolyte ions, which eventually leads to substantially improved charge storage of AC and MnO_2. More significantly, the fabrication process of the flexible ASC is free from any conventional and heavy metallic current collectors (such as ~5 mg/cm^2 for aluminum foil at 20 μm thickness) thus reducing the weight of the SC and maximize the amount of electroactive materials.

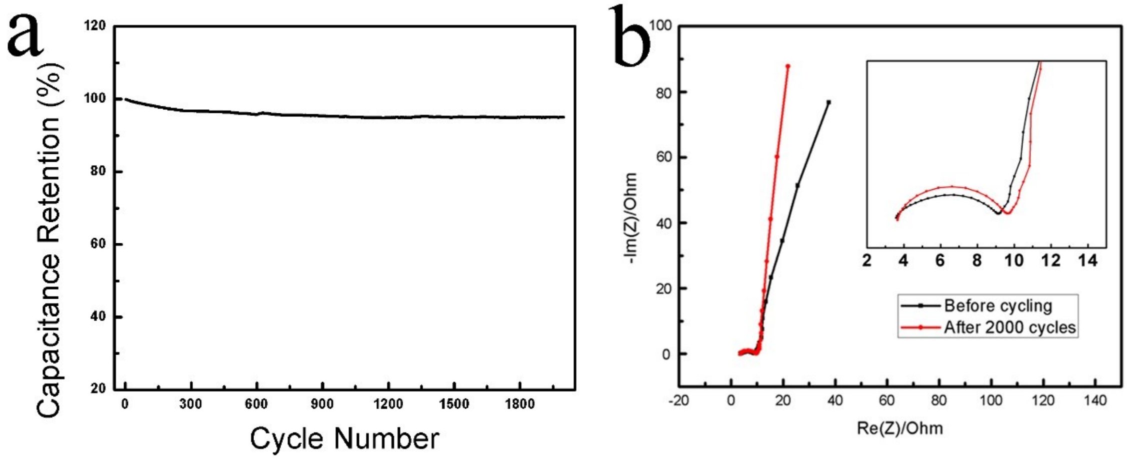

Figure 4.10: (a) Electrostability of a flexible ASC operated at 2 V in 1 M Na$_2$SO$_4$; and (b) Nyquist plots of the ASC acquired before and after the 2000 charge-discharge cycles.

Long cycle life is critical for practical ASC. The cycle performance of a fabricated flexible ASC was evaluated by a 2000 cycles charge-discharge test conducted at 1 A/g (1.2 kW/kg). Figure 4.6b shows the capacitance retention ratio as a function of cycle numbers, and indicates only ~ 5% of capacitance loss compared with the initial capacitance after 2000 cycles (~95% capacitance retention). Such high capacitance retention ratio is comparable with other ASCs and thus is highly promising for practical applications. The electrochemical impedance spectra (EIS) acquired before and after the 2000 cycles were plotted as the Nyquist plots (Figure 4.6b, insert). As can be seen from this figure, both of the impedance spectra show a typical arc at high frequencies and a spike at low frequencies that is typical for ideal supercapacitors.[97] Upon cycling, the EIS shows only subtle changes and thus further demonstrates excellent electrochemical stability of the fabricated ASC. The nearly vertical-shaped spikes also demonstrate facilitated ion diffusion across the flexible electrodes at low frequencies, which agree well with other characterization results as discussed above.

4.4 Conclusion

In conclusion, a cost-effective approach to fabricate flexible ASCs with both high power and high energy density was developed. The combination of unique properties from different nanomaterials (activated carbon, CNTs, MnO_2 and graphene) allows fabrication of flexible electrodes with superior mechanical strength, electric conductivity and efficient use of the electroactive materials. Working together, the flexible electrodes showed improved charge storage with facilitated transportation for both ions and electrons, thus rendering the assembled ASC with high power and energy densities, as well as remarkable electrostability over large operation voltage ranges (~2.0 V) in aqueous electrolytes. Combining with the advantage of the binder-free and current collector free approach, the present method shows great promise towards the design of low-cost, lightweight and high performance energy storage systems.

Chapter 5: Improving the Performance of Cobalt-Nickel Hydroxides based Self-supporting Electrodes for Supercapacitors using Accumulative Approaches[*]

5.1 Introduction

Advanced energy storage systems with both high power and energy densities are highly desired for future society due to their potential impacts to a variety of fields including transportation, renewable energy and portable electronics.[2, 57] Hence, considerable research efforts have been devoted to the design of advanced electrodes with increased performance metrics for batteries and supercapacitors.[42, 58, 145]Nickel hydroxide ($Ni(OH)_2$), in particular, is one of the widely used materials for batteries[146] and could potentially be used for supercapacitors due to its low cost, well-defined redox behavior and high redox activity.[131] Usually, $Ni(OH)_2$ used in supercapacitors is in either the well crystallized β-phase or the poorly crystallized α-phase.[147] However, both of these phases have low electrical conductivity (~10^{-5}-10^{-9} s/cm).[148] Hence, the electrodes made with them generally have compromised rate capability and reversibility and therefore are not suitable for high power applications. As a result, it is highly desirable to develop effective strategies to assemble $Ni(OH)_2$-based electrodes that are able to support fast electronic and ionic transport with improved power capability and cycle stability.

---

[*] This chapter has been submitted to ***Energy & Environmental Sciences***, and currently is under review.

Over the past decades, various approaches have been attempted to enhance the electrochemical performance of $Ni(OH)_2$. Of these, one effective approach is to directly grow $Ni(OH)_2$ as nanoparticles on highly conductive substrates, such as graphene,[149] carbon nanotube[150] and activated carbon.[151] These conductive substrates are able to electrically connect $Ni(OH)_2$ nanoparticles and thus could improve their capacitance and rate capability. For example, $Ni(OH)_2$ grown on lightly oxidized graphene sheets was able to deliver 1335 F/g.[149] Noticeably, several recent studies demonstrated that $Ni(OH)_2$ directly deposited on the walls of three dimensional nickel foam substrates exhibited very high specific capacitance (> 2500 F/g).[152, 153] However, the amount of $Ni(OH)_2$ that can be loaded by such methods is limited. Additionally, nickel foams by themselves have redox activity in alkaline electrolytes and thus could exaggerate the observed results.[154] Alternatively, another effective approach is to synthesize mixed hydroxides by partially substituting Ni with other cations, such as Co,[155, 156] Al,[146, 157] Fe,[158] and Mn[159]. In particular, the Co-Ni double hydroxides generally exhibit increased capacity and improved cycle stability compared with pure $Ni(OH)_2$.[156, 160-162] For instance, the Co-Ni hydroxide nanocones exhibited a specific capacitance of ~1500 F/g.[162] Yan et al. synthesized Ni-Co double hydroxides microspheres with hollow interior that have improved capacity of 2275.5 F/g at 1 A/g, but the capacitance faded rapidly to only ~1000 F/g at 25 A/g.[163] In general, however, these strategies still suffer from either low rate capability, low specific capacitance or limited material loading. Hence, it is still desirable to develop strategies for assembling electrodes with combined properties of high capacity, rate capability and material loading.

In this project, we describe an effective accumulative approach to fabricate high performance electrodes. Specifically, we not only synthesized advanced active materials of Co_xNi_{1-x} double hydroxides directly grown on graphene sheets to take the advantage of both nanoscale conductive substrate and cobalt substitution, but we also developed an effective electrode assembly strategy. Currently, the most widely used approach for fabricating electrodes is based on mixtures of active material, conductive carbon and binder. This approach, however, is not ideal for nanoscale active materials because these components are under different size scales (nano vs. micro) and their interactions is unsatisfactory. The isolating binder could also affect the rate performance of the electrodes. Recently, hybrid electrodes assembled using different nanomaterials to fully take their advantages have attracted substantial interests. For example, graphene and CNT composites were used to support noble metal catalysts for improved activity for electrocatalysis.[164, 165] Deposition of MnO_2 onto pre-assembled graphene/CNT nanocomposites also showed significantly improved activity. [166] In those studies, CNTs and graphene were mostly used to assemble three dimensional and porous carbon frameworks for decorating active materials but their unique advantages were relatively not well realized (for example, the deposition of active materials inside the frameworks could not be uniform). In this study we designed a better strategy that clearly defined the functionality of graphene and nanotubes by using graphene as high surface area substrate to anchor active materials and CNTs to interconnect graphene/active material composites. A advantages of this design include interconnected highly conductive and porous CNT networks that will truly act as nanoscale current collectors, superior electronic conductivity and remarkable porosity because of the combined effects from graphene and CNT and therefore afford active materials with close to their theoretical capacity and significantly improved rate-performance. More significantly, this strategy is scalable and controllable toward large scale productions. The electrodes exhibited tunable electrochemical behavior with remarkably high specific capacitance (2360 F/g at 0.5 A/g), rate capability (~2030 F/g at 20 A/g, 86% retention ratio) and good cycle stability compared with previous studies. In strong contrast, electrodes made with either pure $Ni(OH)_2$ or $Co(OH)_2$, or with traditional fabrication approaches all showed inferior performance.

5.2 Experimental details

5.2.1 Materials and methods

GO was synthesized using modified Hummer's method.[34] Few-walled CNTs were synthesized and functionalized following developed procedure.[76] $Ni(NO_3)_2 \cdot 6H_2O$ and $Co(NO_3)_2 \cdot 6H_2O$ were purchased from Sigma-Aldrich; Ammonium hydroxide and KOH were purchased from Fisher Scientific; Hydrazine hydrate (35%) was from Acros Organics.

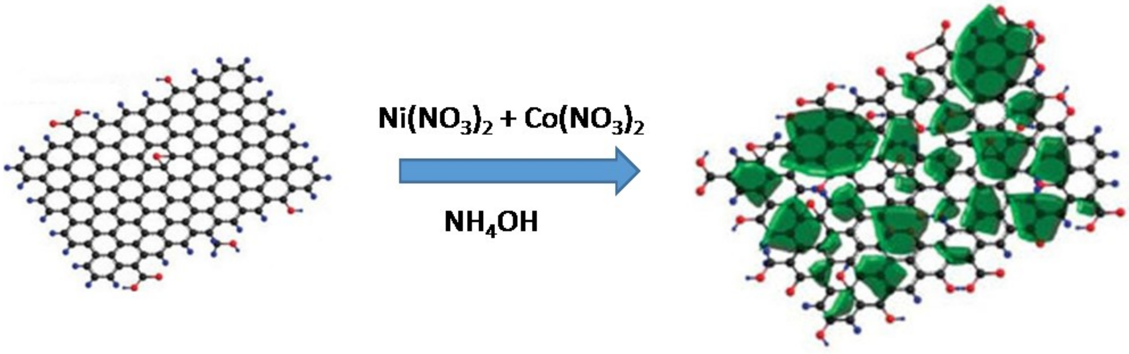

Figure 5.1: Schematic illustration of the process used to synthesis double hydroxide/RGO nanocomposite.

RGO sheets were prepared similarly as described in Chapter 2. Afterwards, cobalt nitrate and nickel nitrate aqueous solution with appropriate molar ratio was added to the graphene dispersion (as shown in Figure 5.1). Uniform coatings of small Co-Ni hydroxides were deposited on the graphene sheets by adding ammonium hydroxide. The amount of graphene in the final composites were controlled to be ~10 wt%. Different molar ratios of $Co(NO_3)_2$ and $Ni(NO_3)_2$ were used to synthesize composites with controlled cobalt substitution ($0 \leq x \leq 1$). For example, to synthesize the $Co_{0.5}Ni_{0.5}(OH)_2$/graphene composite, 140 mg of $Co(NO_3)_2 6H_2O$ and 140 mg of $Ni(NO_3)_2 6H_2O$ were firstly added to 40 ml of the graphene suspension. Then ammonium hydroxide was added dropwise under continuous sonication until the pH of the mixed solution reach 9 that was indicative of completed precipitation reaction. Finally the products were collected by vacuum filtration through a membrane (1.2μm, Millipore) and rinsed with nanopure water until pH is neutral.

5.2.2 Material characterization

Material characterization is the same as described in Chapter 2.

5.2.3 Electrodes assembly and measurements

The electrodes for electrochemical tests were assembled with fFWNTs as shown in Figure 5.2.[76] Typically, ~ 6.0 mg of the double hydroxide/graphene composite and ~1.5 mg of fFWNTs were dispersed together in water with the aid of sonication to ensure good mixture. Afterwards the mixture was collected by vacuum-filtration through a cellulose membrane (Millipore). Then the filtered cake was dried firstly under ambient condition for 24 hours and then at 70°C for 3 hours and afterwards a self-standing film (disc shape with diameter 1.2 cm) was obtained. A small piece of the film was then pressed onto a piece of nickel mesh and used as the working electrode for all the testing. For control purposes, several electrodes were also fabricated without graphene or/and CNTs. In these cases, the active material was mixed with carbon black and polyvinylidene difluoride (PVDF) with the mass ratio of 70:20:10 and the mixture was casted on nickel foam, which was then dried and used directly as the working electrodes.

Electrochemical characterization was conducted using a Bio-logic SP300 instrument. A saturated calomel electrode (SCE) and a platinum wire were employed as a reference and counter electrode respectively. 2 M KOH solution was used as the electrolyte. The energy storage characteristics of the electrodes were evaluated using CV and galvanostatic charge-discharge techniques. Electrochemical impedance spectroscopy (EIS) measurements were conducted in a frequency range from 10mHz to 200 kHz at open-circuit potential with an ac perturbation of 5 mV.

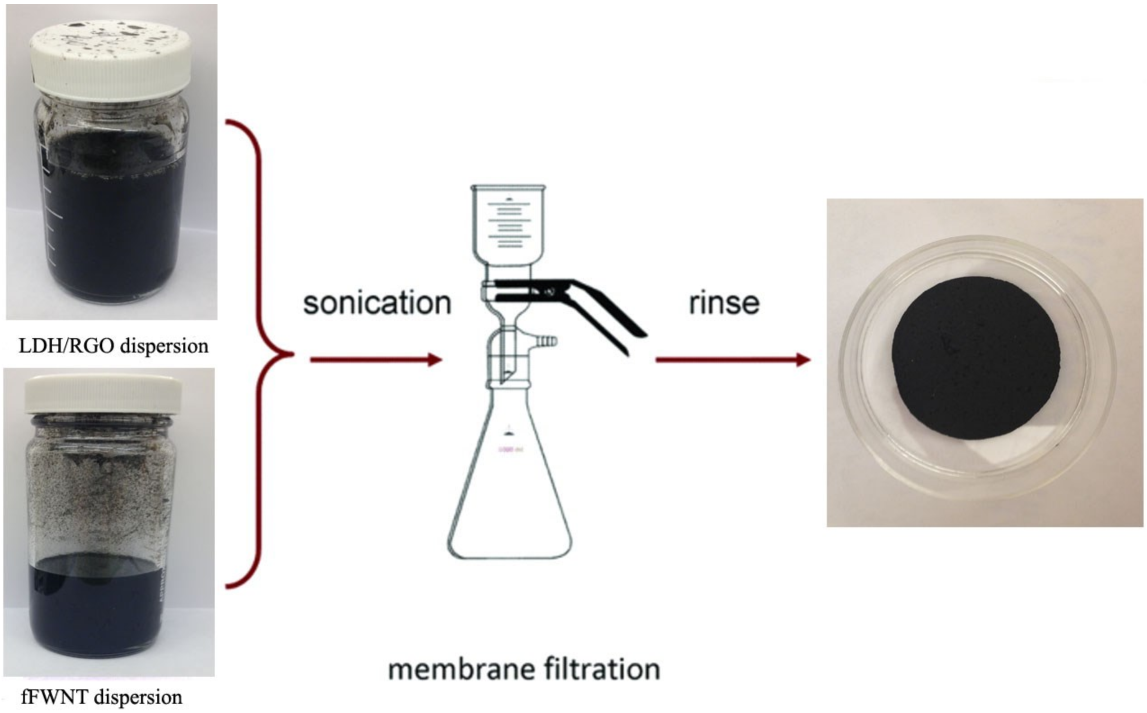

Figure 5.2: Illustration of the electrode fabrication process.

The specific capacitance of the electrodes were calculated using the same method as described in Chapter 2.

5.3 Results and discussion

Since nickel hydroxide and cobalt hydroxide have similar crystal structures and solubilities in water, they could be precipitated together with the addition of ammonium hydroxide. Importantly, sonication was used over the course of the entire synthesis process to avoid the aggregation of graphene and ensures uniform hydroxide coating.[58]

As revealed by TEM images, the Co-Ni double hydroxides were grown uniformly on graphene surface and were in the shape of "nanodiscs" that is indicative of layered structure (Figure 5.3 a and b). The sizes of the hydroxide particles were in the range of 10~30 nm.

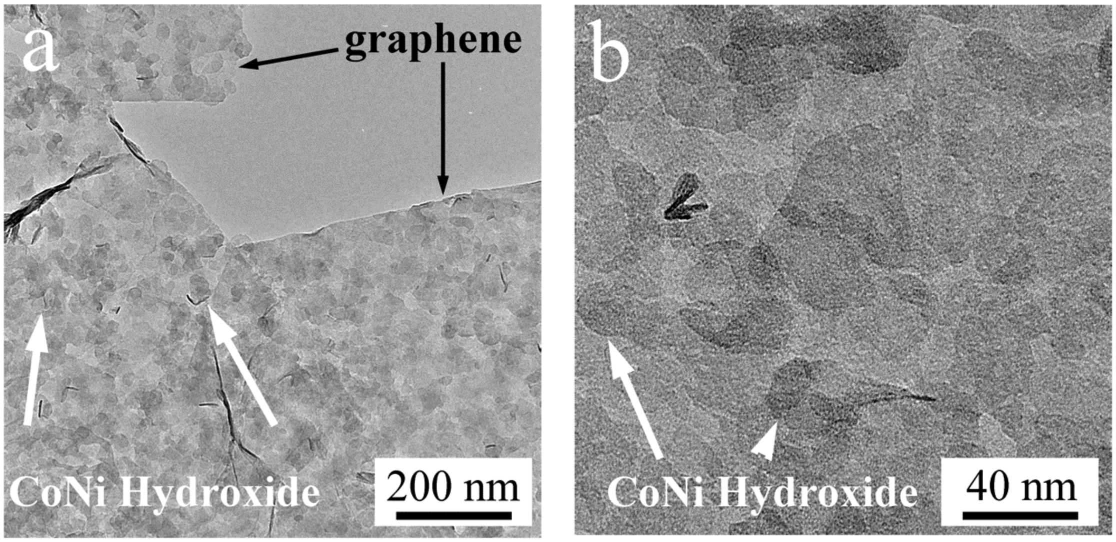

Figure 5.3: TEM images at different magnifications acquired from a sample of $Co_{0.5}Ni_{0.5}(OH)_2$/graphene composite.

The SEM image (Figure 5.4a) further indicates that the hydroxide particles appear uniformly on the graphene sheets and no obvious aggregates were identified. The actual molar ratios of cobalt to nickel were determined by EDS and the results were very close to the molar ratios of their precursors, indicating a very efficient co-precipitation process. A typical EDS spectrum for the $Co_{0.5}Ni_{0.5}$ hydroxide/graphene composite is shown in Figure 5.4b. The EDS mappings of cobalt and nickel (Figure 5.5) show that both of them distributed continuously and uniformly in the composite and no obvious phase segregation was observed.

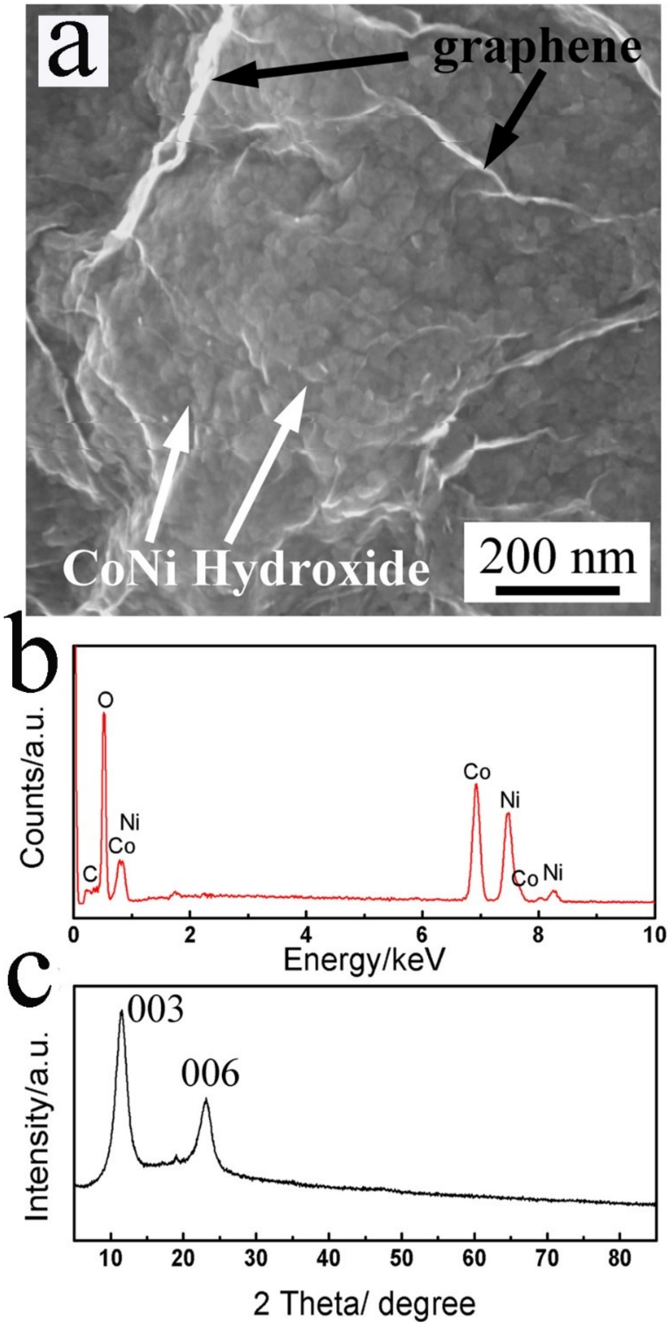

Figure 5.4: a) SEM image; b) EDS spectrum and e) XRD pattern acquired from a sample of $Co_{0.5}Ni_{0.5}(OH)_2$/graphene composite.

X-ray diffraction (XRD) measurements were conducted to determine the phase of the as-prepared double hydroxides. A typical pattern is presented in Figure 5.4c, which was acquired from the $Co_{0.5}Ni_{0.5}(OH)_2$/graphene composite. Composites with other Co/Ni ratios show similar patterns. As can be seen, two distinctive diffraction peaks at 11.50° and 23.06° were identified, which can be assigned to the 003 and 006 reflection of the hydrotalcite-like structure.[167] The d-spacing between the basal plane of the double hydroxide was determined as 7.69 Å. Noticeably, this is between the 7.56 Å of pure α-$Ni(OH)_2$ [168] and the 7.75 Å of pure α-$Co(OH)_2$.[169] Such results are indicative of a well-mixed layered structure of the synthesized double hydroxide that agrees well with the EDS mapping results. From the width of the diffraction peaks, the average diameter of the particles was estimated and is consistent with the TEM and SEM results as discussed above. However, no other diffraction peaks were identified, indicating the hydroxides were poorly crystallized. Additionally, no diffraction peak corresponding to graphene (at ~25°)[170] was observed, indicating that most of the graphene was covered by the hydroxides and hence the layer-to-layer interaction between adjacent graphene pieces as in a pure graphene film is significantly reduced in the composite.

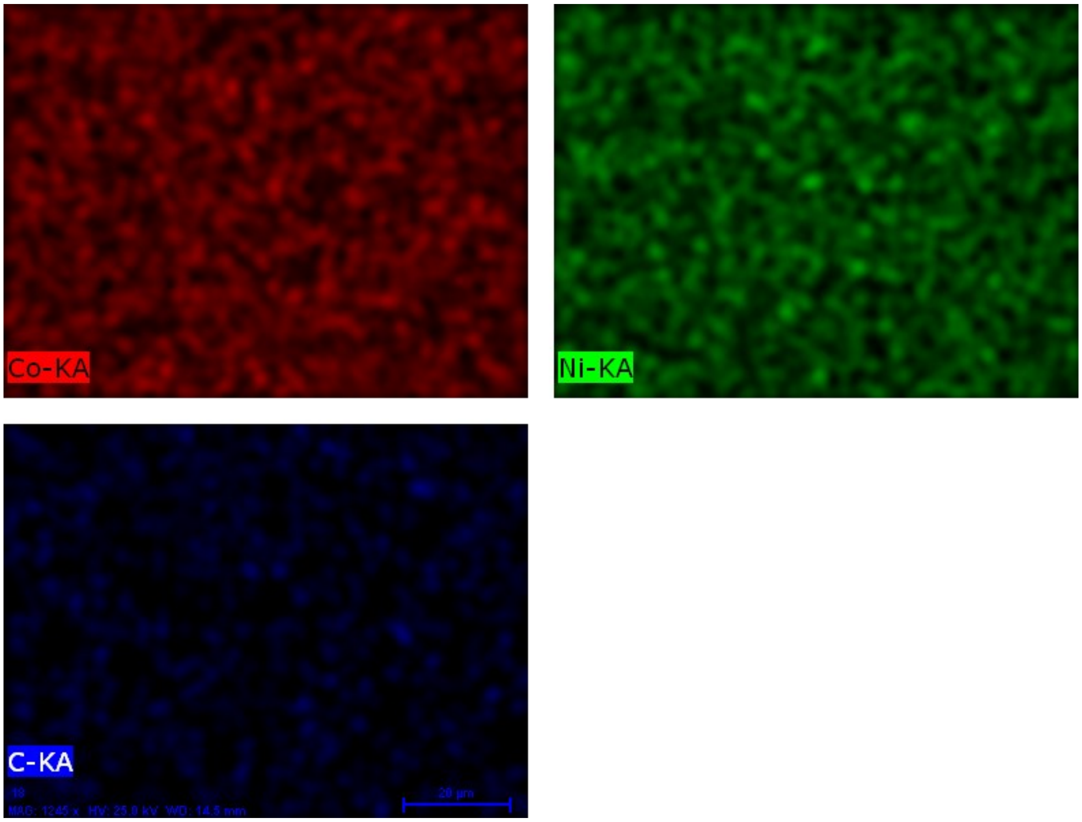

Figure 5.5: EDS elemental mapping of the $Co_{0.5}Ni_{0.5}(OH)_2$/graphene composite. Both nickel and cobalt appear distributed uniformly in the composite, no obvious phase segregation was observed

As described in the experimental section, our electrodes were fabricated as freestanding films with 20 wt% of CNTs using the accumulative approach and their mass loading densities were all ~6.0 mg/cm^2. Such loading density is significantly higher than most of previous studies where loadings were usually less than 1.0 mg/cm^2.[149, 160, 171] Material loading is an important parameter in determining the device-level performance metrics since weights from components such as electrolyte, separator and current collector also need to be considered.[75] This means that devices with low active material loadings will have inferior device-level performances per unit volume or weight and therefore electrodes with high material loadings are preferred for practical applications. Designing electrodes with both high material loading and good performance is very challenging especially for metal oxide/hydroxides based systems since any increase in loading will decrease their performance due to their poor conductivity.[172] This study effectively resolves this challenge by the incorporation of interconnected, highly conductive and mechanically strong fFWNTs that link graphene/double hydroxide composites to ensure superior electrical conductivity throughout electrodes.[76, 173] FWNTs were used selectively because they have higher electrical conductivity and better mechanical strength compared with MWNTs and excellent balance between surface functionalization and electrical conductivity compared with SWNTs because the functionalization process will only damage their outer-walls and leave inner-walls intact. Figure 5.6 shows a set of CV curves for hydroxides with different amounts of cobalt (x=0, 0.3, 0.5, 0.7, 1.0) measured in a potential range of -0.15 V~0.45 V at a scan rate of 5 mV/s. The redox peaks were clearly defined, which could relate to the combined contributions from the redox reactions derived from cobalt and nickel hydroxides: $Co(OH)_2 + OH^- \leftrightarrow CoOOH + H_2O + e-$ and $Ni(OH)_2 + OH^- \leftrightarrow NiOOH + H_2O + e^-$. [162] In contrast to previous works that observed separate redox peaks from $Co(OH)_2$,[163, 174] the electrodes fabricated herein only exhibit one pair of redox peaks. The absence of peak separation might be due to the good mixing of Co-Ni composite as revealed by the XRD and EDS results. Interestingly, the double hydroxides show cobalt concentration (x)-

dependent reduction and oxidization peak positions, indicating the electrochemical behavior of the mixtures could be readily tuned by controlling their composition. Importantly, the redox currents were noticeably enhanced after the addition of cobalt, indicating increased SC.

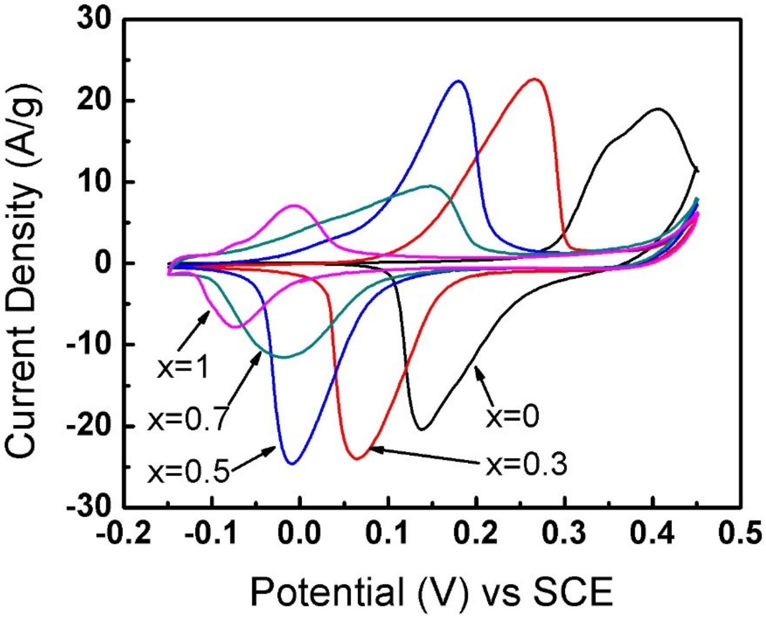

Figure 5.6: CV curves at 2 mV/s for $Co_xNi_{1-x}(OH)_2$/graphene/CNTs composite electrodes with different cobalt concentrations.

The galvanostatic charge-discharge behavior of the hydroxides was studied at 1 A/g. The results are shown in Figure 5.7a and they also exhibited cobalt dependent behavior corresponding well with CV results. The potentials (vs. SCE) of the discharge plateau shifted from 0.22 V for pure $Ni(OH)_2$ to 0.14 V, 0.12 V, 0.03 V for x=0.3, 0.5, 0.7, respectively. On the basis of these results, the SCs of the $Co_xNi_{1-x}(OH)_2$ were determined to be 1960, 2123, 2305, 1529 and 843 F/g for x=0, 0.3, 0.5, 0.7 and 1, respectively (Figure 5.7b). The substitution of nickel with appropriate amount of cobalt clearly increased the

SC of the electrodes and the peak performance was reach with ~ 50% of cobalt. electroactive sites due to possible valence interchange or charge hopping between Co and Ni cations. [161, 162, 174] More significantly, the accumulative approach can afford electrodes with substantially higher specific capacitance compared with traditional approaches used by earlier studies and further strengthened the importance of graphene and CNTs toward high performance electrodes. It is also noteworthy that our electrode assembly approach is also able to support pure $Ni(OH)_2$ with much higher SC (~1960 F/g) compared with previously reported results.[149, 175]

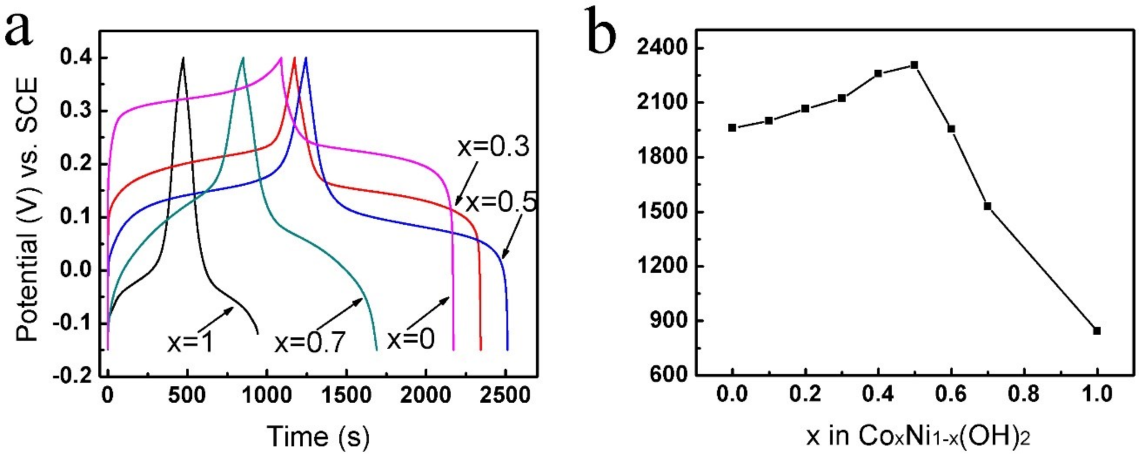

Figure 5.7: a) Galvanostatic charge-discharge curves at 1 A/g for $Co_xNi_{1-x}(OH)_2$/graphene/CNTs composite electrodes with different cobalt concentrations and b) comparison of the specific capacitances for the composite electrodes with different value of x.

On the basis of the results discussed above, it is obvious that the $Co_{0.5}Ni_{0.5}(OH)_2$/graphene/CNTs electrode has the maximum specific capacitance. However, its performance under high current condition also needs evaluation for practical applications. Hence, its rate capability was further studied. Figure 5.8 shows the galvanostatic discharge curves acquired at increasing current densities from 0.5 to 20 A/g. Noticeably, all of them exhibited well-defined discharge plateau in the range of 0.0~0.1 V (vs. SCE), indicating that the hydroxides were highly active for all the current densities studied. The double hydroxides grown on graphene delivered a SC as high as 2360 F/g (360 mAh/g) at 0.5 A/g and still kept a remarkable 2030 F/g (310 mAh/g) at the high current density of 20 A/g (~86% retention, Figure 5.9), which are substantially higher than previous studies on double hydroxides.[161, 163] Furthermore, such high rate capability (a 86% retention ratio as the current densities increases by 40 times) is close to that of pure carbon based electrochemical double layer capacitors (EDLC)[40] and is significantly higher than typical pseudocapacitor materials including MnO_2 [76] and RuO_2 [176]. Besides, considering the fact that such high specific capacitance and remarkable rate capability were obtained from electrodes with high mass loading of ~6 mg/cm^2, the electrode architecture designed in this work is of promising practical significance in real products. Generally, high values of specific capacitance and capacitance retention can only be obtained from electrodes with densities less than ~1 mg/cm^2 and both of them fade rapidly as the electrodes become thicker.[75] Hence, it is reasonable to conclude that the electrode architecture designed in this work offers high conductivity and high electroactive material utilization efficiency.

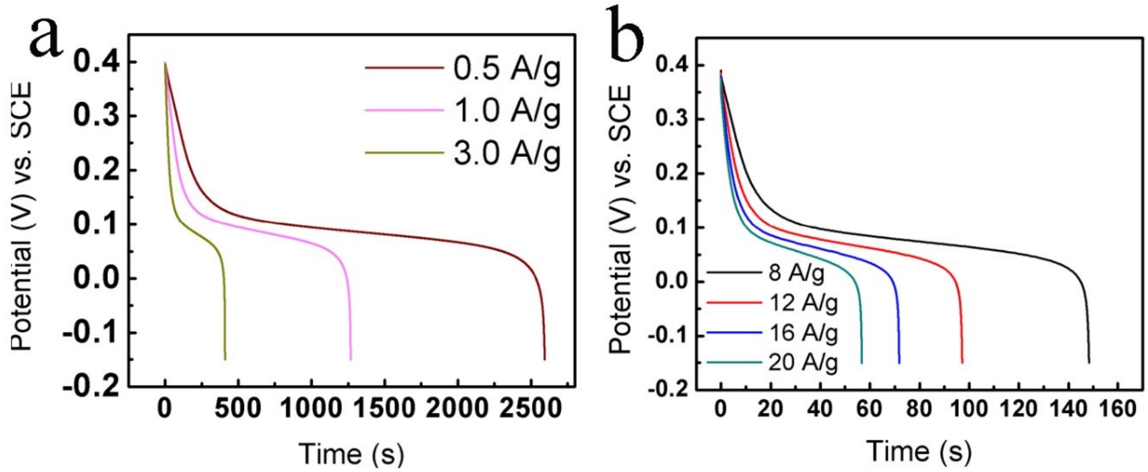

Figure 5.8: Galvanostatic charge-discharge curves for a $Co_{0.5}Ni_{0.5}(OH)_2$/graphene/CNTs electrode at different current densities.

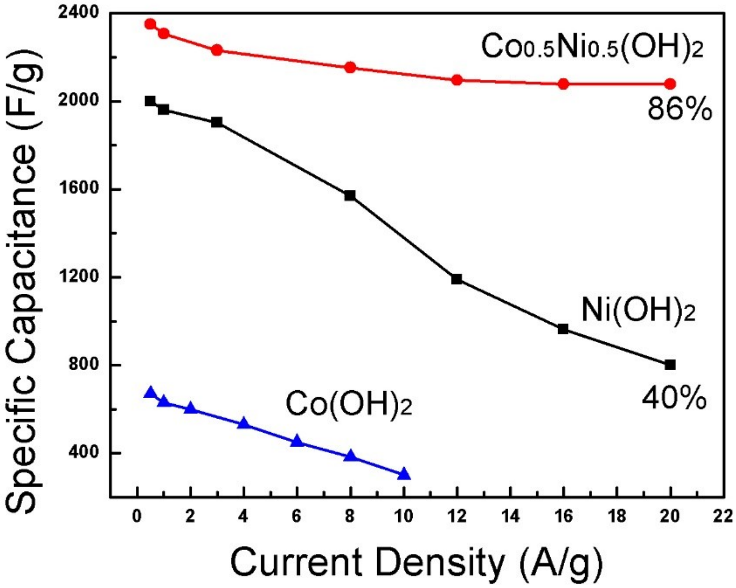

Figure 5.9: Comparison of the variations of the specific capacitance of $Co_{0.5}Ni_{0.5}(OH)_2$, $Ni(OH)_2$ and $Co(OH)_2$ at increasing current densities, all of the electrodes were made with graphene and CNTs

The significantly improved electrochemical performance of the electrode assembled in this work could be attribute to the synergistic contributions from cobalt substitution, graphene and CNTs. Without cobalt substitution, a pure $Ni(OH)_2$ electrode has ~2000 F/g at 0.5 A/g but quickly fade to ~800 F/g at 20 A/g (Figure 5.9). On the other hand, a pure $Co(OH)_2$ electrode has much lower capacitance of 670 F/g at 0.5 A/g. Therefore, it is obvious that the addition of cobalt not only improved the specific capacitance but also the rate capability of the electrode. To gain deeper insight, EIS were conducted at the charging potentials of the electrodes made with and without cobalt evaluate their charge transfer characteristics.[177] Figure 5.4b compares the Nyquist plot of electrodes consisting of $Co_{0.5}Ni_{0.5}(OH)_2$ or $Ni(OH)_2$ (both made with graphene and nanotubes). Both electrodes show similar EIS profiles, with a semicircle at high-frequency region and a straight line at low-frequency region. The calculated charge-transfer resistances (R_{ct}) at high frequency range were estimated to be ~ 2.0 Ω for the double hydroxide electrode, which is noticeably lower than the ~2.6 Ω for pure $Ni(OH)_2$. Additionally, the double hydroxide electrode exhibited a more close to vertical spike in the low frequency region, indicating that cobalt substitution also improved the capacitive behavior of the electrode, likely because the double hydroxide particles were much smaller with higher surface area than $Ni(OH)_2$.[174] Therefore, the increases of the performance metrics after cobalt substitution may originate from both the reduced charge transfer resistance and improved capacitive behavior since $Co(OH)_2$ has much higher conductivity than $Ni(OH)_2$.

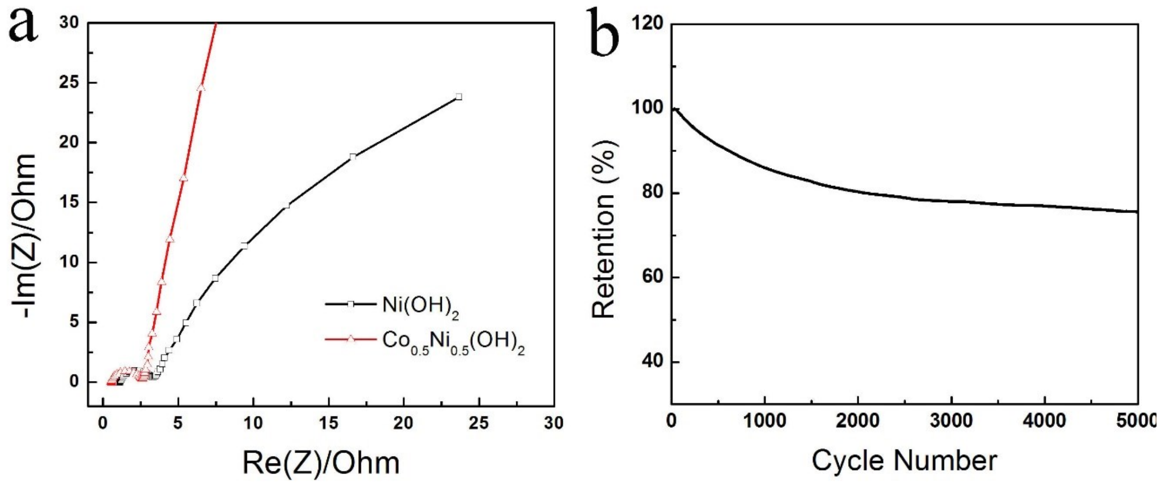

Figure 5.10: a) Comparison of the Nyquist plot of electrodes made with $Co_{0.5}Ni_{0.5}(OH)_2$ or $Ni(OH)_2$; b) Cycling stability of the $Co_{0.5}Ni_{0.5}(OH)_2$/graphene/CNTs electrode at 10 A/g.

Both CNTs and graphene are critical on achieving high performance reported here. In a control experiment, an electrode was made without nanotubes by casting a mixture of $Co_{0.5}Ni_{0.5}(OH)_2$/graphene composite, carbon black and binder (PVDF) on a piece of nickel foam (a standard method used by most groups to evaluate active materials) and its performance was evaluated (Figure 5.10 a and b). The double hydroxide only has ~ 1000 F/g at 0.5 A/g, far below the ~2300 F/g when made with CNTs under the same current density. On the other hand, another control electrode was assembled without graphene and nanotubes. In this case, the Co-Ni hydroxides were synthesized without the presence of graphene and the electrode was made similarly as the control electrode discussed above. Electrochemical testing results revealed that such electrode only delivers 860 F/g at 0.5 A/g and 580 F/g at 10 A/g (Figure 5.10 c and d)

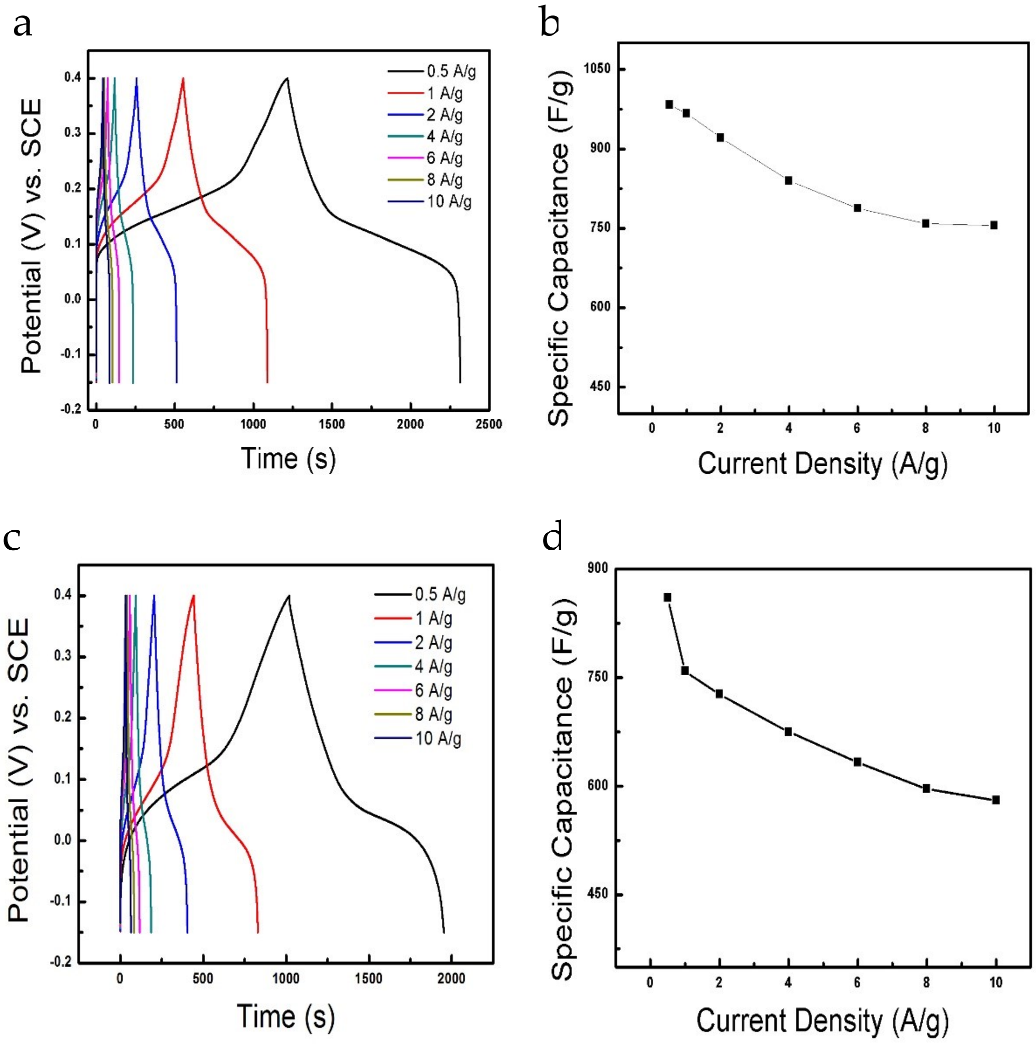

Figure 5.11: Electrochemical testing results of control electrodes: (a) and (b) without CNTs and (c) and (d) without CNTs and graphene.

The cycle stability of the $Co_{0.5}Ni_{0.5}(OH)_2$/graphene/CNT hybrid electrode was evaluated by 5000 galvanostatic charge-discharge cycles at 20 A/g. The retention ratio, as a function of cycle numbers, is plotted in Figure 5.10b. The electrode exhibited capacity decay relatively high initially but was able to stabilize afterwards. Overall, it exhibited ~25% decay for 5000 cycles and this is comparable or better than previous studies.[156, 160, 162] The observed capacitance fade might be related to the volume expansion and shrinkage of the layered structures of the hydroxides under repeated charge-discharge process. Nevertheless, the cycle stability of the double hydroxide is improved compared to pure $Ni(OH)_2$, which shows much higher capacitance loss under the same testing condition (Figure S4), similar as previous studies.[156]

Finally, we assembled ASC using the double hydroxide-based electrodes as the positive electrodes to evaluate their practical applications. The negative electrodes were made with activated carbon and fFWNTs using the method as we previously reported.[148] Figure 5.6a compares the CV curves of these two types of electrodes acquired at scan rates as noted and indicates that their combination as ASC is able to afford devices with 1.4 V operation voltage. In fabrication of ASC, the weights of positive and negative electrodes were optimized based on results of single electrode measurement to assure efficient utilization of electroactive materials. The energy storage characteristics of the assembled ASC were studied using CV and charge-discharge techniques at different current densities (results shown in Figure 5.6 b and c). The device was able to deliver specific capacitance as high as 150 F/g (based on the total weight of both electrodes) at 300 mA/g and 106 F/g at a high current density of 6.0 A/g. On the basis of these results, the energy and power densities of the ASC were determined and the results were shown as Ragone plot in Figure 5.6d. The device was able to deliver a high energy density of 41 Wh/kg at the power density of 210 W/kg and still kept a remarkably energy density of 29 Wh/kg as the power density was increased to 4.2 kW/kg, which are substantially higher than typical ASC.[173] Noticeably, the retention of energy density as the power density increases is also remarkably higher than similar studies.[178]

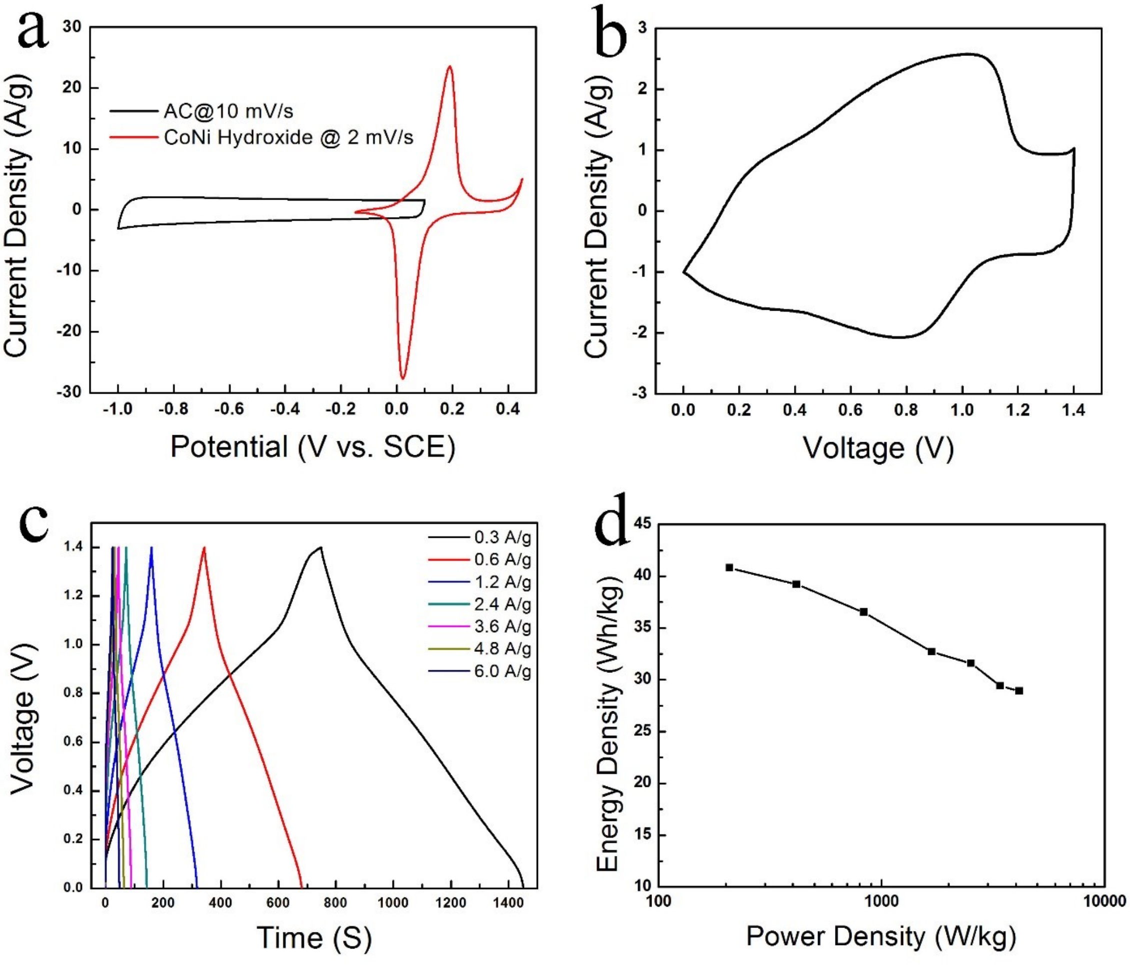

Figure 5.12: (a) Comparative CV curves of an electrode made with activated carbon (AC) and CNTs and an electrode made with $Co_{0.5}Ni_{0.5}(OH)_2$/graphene/CNTs. (b) CV and (C) charge-discharge curves at different current densities of an ASC assembled using $Co_{0.5}Ni_{0.5}(OH)_2$/graphene/CNTs positive electrode and AC/CNT negative electrode, and (d) the corresponding Ragone plot of the ASC.

5.4 Conclusion

In summary, a simple, scalable and solution based method to synthesize layered Co-Ni double hydroxide/graphene composites with controlled composition was developed in this work. The energy storage characteristics of the composites were evaluated using self-standing thick films fabricated using carbon. Experimental results indicate that the synergistic contributions from cobalt substitution, graphene and CNTs enabled substantially improved electrochemical performance. With 50% cobalt ($Co_{0.5}Ni_{0.5}(OH)_2$), the double hydroxide exhibited the maximum SC of 2360 F/g (~360 mAh/g, at 0.5 A/g) and still maintained a remarkable value of 2030 F/g at 20 A/g (~86% retention). Control experiments show that the double hydroxides outperform either of the $Co(OH)_2$ or $Ni(OH)_2$ alone. Additionally, the mixed hydroxides exhibited tunable redox behavior that can be controlled by the ratio between cobalt and nickel contents. These results demonstrate the importance of the rational design of functional composites and large-scale assembly strategies for assembly of electrodes with improved performance for energy storage applications.

Chapter 6: Highly Efficient Oxygen Reduction Electrocatalysts based on Winged Carbon Nanotubes[*]

6.1 Introduction

The development of electrocatalysts with high selectivity and efficiency for the oxygen reduction reaction (ORR) is critical for practical applications of fuel cells and metal-air batteries.[179, 180] Precious metals based catalysts (such as Pt and its alloy) are widely used to catalyze the ORR due to their high activity. However, such catalysts are not practical for widespread applications because of their prohibitive high cost, instability over long-term operations (via sintering, dissolution and corrosion of the carbon support) and susceptibility to fuel crossover effect and carbon monoxide poisoning.[181] Consequently, considerable research efforts have been devoted to develop advanced electrocatalysts with improved efficiency, stability and selectivity.[182] In addition to develop Pt-based electrocatalysts with minimized Pt loading and improved stability,[183, 184] alternative non-Pt electrocatalysts including metal-N complex on carbon matrixes, transition metal chalcogenides and doped carbonaceous materials have also been actively pursued.[185-187]

Carbonaceous materials play critical roles over the course of the developments of ORR catalysts and their physicochemical properties have significant influences on the overall activity and durability of the catalysts.[188] Therefore, recent developments of

---

[*] This chapter has been submitted to ***Scientific Reports*** and is currently under review.

CNTs and graphene that possess graphitic structure perfection, corrosion resistance and electrical conductivity bring tremendous opportunities toward developing advanced ORR catalysts.[189] Several previous studies have documented that both graphene and nanotubes can support catalysts with enhanced activity and durability.[190, 191] On the other hand, they can also work as metal-free catalysts after doping with heteroatoms doping (such as nitrogen, sulfur and boron).[192, 193] Such doped materials can be obtained by either direct synthesis in the presence of appropriate precursors (such as NH_3 for N-doping) or doping of pre-synthesized carbon materials.[194] Even though significant progresses have been achieved, the developed catalysts still suffer from limited activity and efficiency owning to inherent drawbacks such as low surface active site densities and low electrical conductivity.[194] In general, highly conductive CNTs usually have limited surface area with relatively low active catalytic sites density. A possible approach to increase active site density is through harsh oxidizations to introduce defects and functional group onto nanotubes.[195] However, this also leads to loss of structural integrity, stability and conductivity of pristine nanotubes. On the other hand, graphene have high surface area in principle. However, their conductivity is much lower than nanotubes owning to the strong oxidization conditions that they experienced during synthesis.[196] More importantly, when used as powder, graphene sheets tend to restack and form "graphite" structure with substantially decreased surface area.[197] In light of these limitations, one would expect that rational combinations of graphene and nanotubes could form hybrids with much better properties than either of them alone. In fact, several approaches have been developed for making such hybrids.[198, 199] One type of approaches involves physical mixing of pre-synthesized nanotubes and graphene but their inter-connection remain unsatisfactory.[199] Direct growth of nanotubes on graphene yield hybrids with better interaction, however, such methods are either labor intensive or difficult to scale-up.[198] Therefore, further developments in hybrid materials preparation are highly desired and such hybrid could make substantial impacts on the progresses of ORR catalysts.

In this project we developed a unique type of CNTs with strongly attached graphene wings (denoted as winged carbon nanotubes, wNT) that were prepared through selective outer-wall unzipping and exfoliation of ultralong stacked-cup nanotubes under controlled oxidization processes. Such unique wNT have dramatically higher surface area than pristine tubes (480 vs. 40 $m^2\ g^{-1}$) and thus could provide abundant catalytic sites. After doping with nitrogen, the N-wNT exhibited strong activity as metal-free catalyst for catalyzing the ORR in alkaline electrolyte through four-electron pathway with outstanding stability and methanol/CO tolerance owning to their unique carbon structure. In addition to work as metal-free catalyst, these high surface area and conductive N-wNT could also be used as advanced catalyst supports. We also show that N-wNT containing 0.9 at% Fe exhibited catalyst activity outperform commercial Pt-based catalysts (20 wt% Pt supported on Vulcan XC72).

6.2 Experimental section

6.2.1 Material synthesis

Oxidized carbon nanotubes (ox-NT) were prepared using a method adapted from the Hummers' method. Stacked-cup carbon nanotubes (SC-CNT) with average diameter of 100 nm (PR-24-XT-HHT, Pyrograf Products, Inc.) was used as the starting material. Typically, 0.2 g of SC-CNT and 1.0 g of $NaNO_3$ were mixed in 40 ml of concentrated H_2SO_4 in a flask that was continuously stirred in an ice bath. Afterwards $KMnO_4$ (6 g) was added slowly. The mixed solution was stirred in an ice bath for 90 min, then at 35°C for another 60 min. The mixture was then poured slowly into 250 ml of water, followed by addition of 10 ml of 30% H_2O_2 solution. After 10 min of stirring, the products were collected by vacuum filtration using a filter membrane (1.2 μm, Millipore) and washed repeatedly with water until pH is neutral. The collected solid was dispersed in water and vigorously sonicated for 30 min. For comparison, surface functionalized SC-CNT (fCNT) was also prepared by refluxing the pristine materials in 6M HNO_3 for 12 hours.

Nitrogen doping of the ox-NT was achieved by annealing their homogenous mixtures with cyanamide at 900°C.[200] Typically, 30 mg of ox-NT and 400 mg of cyanamide were mixed in 10 ml of water. The mixture was then stirred continuously and heated at 100°C to evaporate water. The resulting solid was annealed in two continuous steps: 550°C for 2 hours and then at 900°C for another 1 hour, both under argon flow (200 sccm). For comparison, both nitrogen doped graphene and physical mixture of graphene and fCNT (1:1 weight ratio) were also prepared under identical conditions. Additionally, wNT with both nitrogen and iron contents were prepared by adding appropriate amount of $Fe(NO_3)_3$ into the precursor before drying. The annealing procedure is identical as described above.

6.2.2 Electrochemical measurements

N-wNT catalyst (6 mg) and 20 μl of 5 wt% Nafion solution were dispersed in 2 ml ethanol and 0.2 ml of water by sonication for > 1 hour to form a homogeneous ink. Cyclic voltammetry and rotating disk disk electrode measurement were conducted with a Bio-logic SP300 Potentiostat using a standard calomel electrode as the reference electrode. The potential was then converted to be in reference with the reversible hydrogen electrode (RHE) using $E_{(RHE)}=E_{(SCE)}+0.998$ V. [195] Typically, 20 μl of the catalyst ink was loaded onto a 5.6 mm glassy carbon disk electrode. 0.1 M KOH was used as the electrolyte solution. Before the start of each measurement, the electrolyte was bubbled with the appropriate gas (O_2 or Ar) for > 10 min and continuous gas flow was maintained during the measurement to ensure gas saturation. A scan rate of 10 mV/s was used for all RDE measurements.

For comparison, commercial 20 wt% platinum on Vulcan carbon black (from E-tek) was also measured. The catalyst ink was prepared by mixing 4 mg of Pt/C and 20 μl of 5 wt% Nafion in 1.0 ml ethanol with the aid of sonication for > 1 hour. Other experimental conditions were same as for the N-wNT catalyst.

6.2.3 Material characterization

Scanning electron microscopy (SEM) images were collected using a FEI XL30 FEGSEM. Transmission electron microscopy (TEM) images were obtained by using a FEI Tecnai G^2 Twin operating at 200 kV. Samples for TEM analysis were prepared by placing a drop of the ethanol dispersion of the sample on a lacey Formvar/carbon copper grid (200 mesh, Ted-Pella). Raman spectra of the powder samples were recorded with a LabRAM HR Raman microscope with a laser excitation wavelength of 633 nm. XPS spectra were acquired using a Kratos Analytical Axis Ultra X-ray Photoelectron Spectrometer.

6.3 Results and discussion

Stacked-cup carbon nanotubes (SC-CNT, also known as herringbone carbon nanofibers) with heat-treatment at 3000°C were selectively used as the starting material due to their outstanding electrical conductivity, good graphitic structure (Figure 6.1) and ultra-long length (50~200 μm, Figure 6.2 a,b) compared with other types of multi-walled nanotubes.[201] More significantly, they are commercially available at lower prices than other nanotubes and hence economically more attractive for large-scale applications

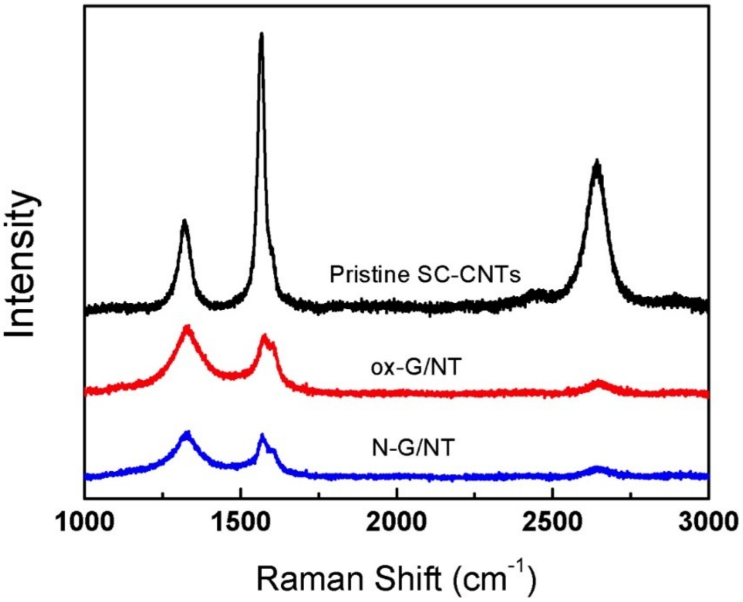

Figure 6.1: Raman spectra of powder materials: pristine SC-CNTs, as-oxidized graphene/nanotube hybrid and nitrogen doped hybrid.

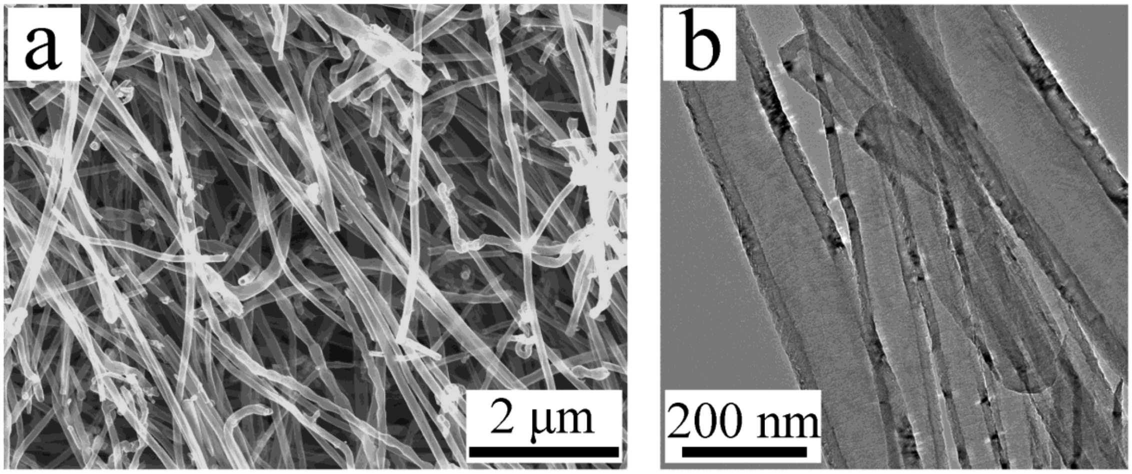

Figure 6.2: (a) SEM and (b) TEM image of pristine SC-CNT.

A high-resolution transmission electron microscopy (TEM) image shown in Figure 6.3 revealed that such nanotube has stacked-cup carbon structure as inner tubular core and a thin layer assembly of concentric cylinders of graphene as external coating.

Because of this unique structure, the external graphene layers were more prone to be oxidized when subjected to the oxidization condition described in the method section due to direct contact with oxidizing chemicals. As a consequence, the external layers of the as-oxidized SC-CNTs (ox-NT) were heavily oxidized, whereas the inner stacked-cup tubular structures remained intact as their d-spacing did not increase obviously (Figure 6.3). The defective nature of the ox-NT is evident from the high D/G ratio in Raman spectroscopy (Figure 6.1).

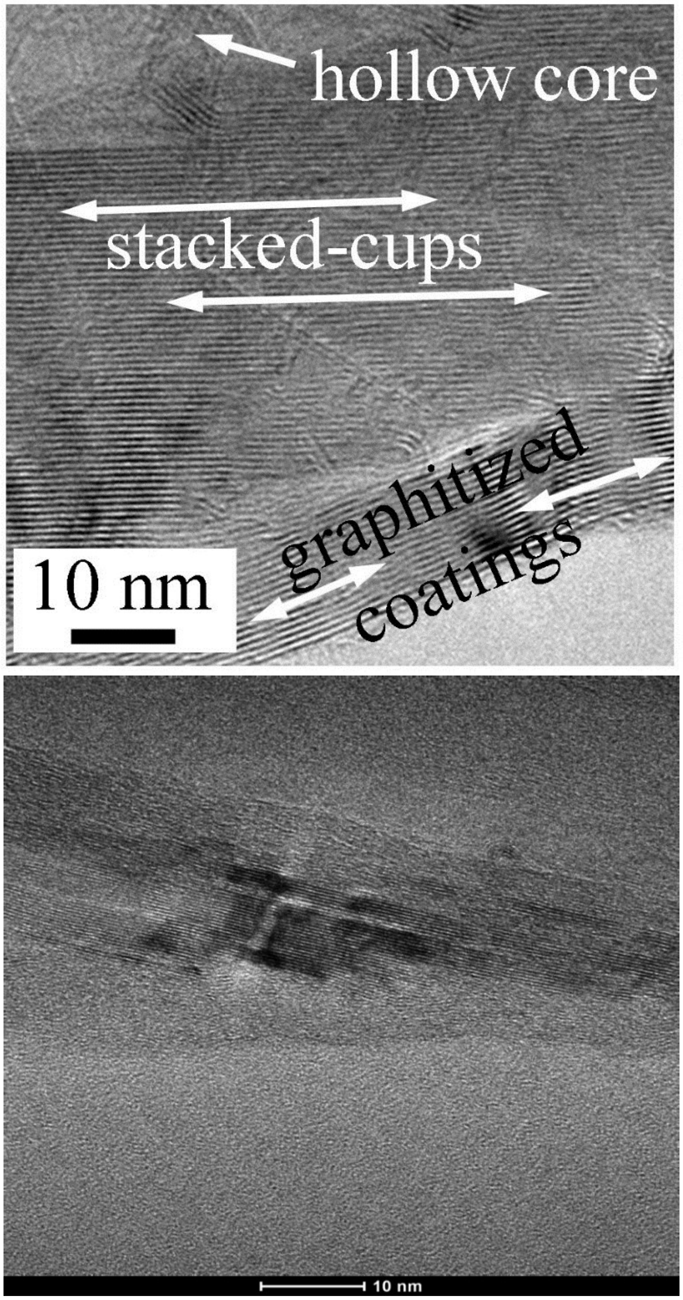

Figure 6.3: High resolution TEM image for (up) pristine SC-CNTs and (down) as-oxidized nanotube, note that while the outer graphene coatings were heavily oxidized, the inner tubular structure was largely preserved.

After a sonication step (30min) that was applied to unzip and exfoliate the heavily oxidized external graphene, we found that their average diameter was substantially increased from 100 nm to 180 nm. More importantly, the ultra-long nature of the initial materials was largely preserved due to, presumably, the intact inner core (Figure 6.2d) and the ox-NT were much longer than oxidized few-walled CNTs prepared under similar conditions (hundreds of nanometers).[195]

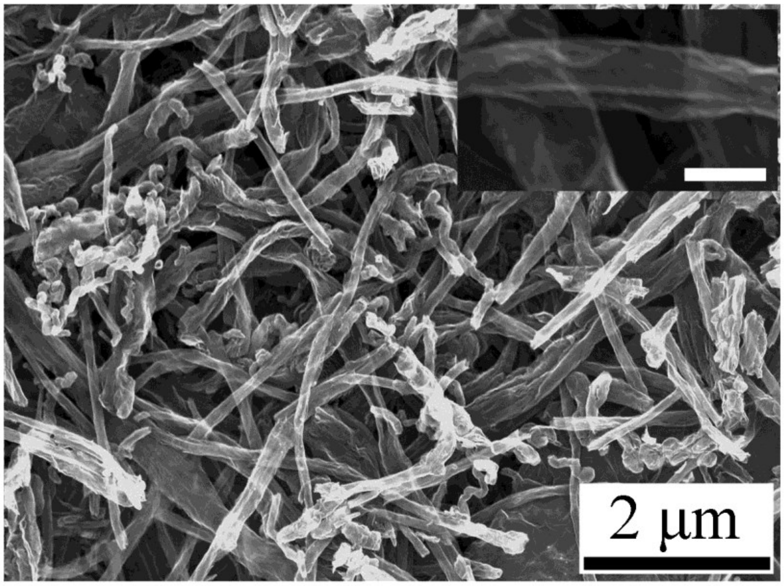

Figure 6.4: SEM image of the exfoliated ox-NT, the scale bar for the inserted SEM image is 200 nm.

A closer examination of the products (Figure 6.5) revealed that the outer layers of the original SC-CNT were successfully exfoliated through the unzipping process as clearly shown in Figure 6.4,[202] forming graphene wings strongly attached to nanotubes.

The TEM image of Figure 6.5 shows a collection of several wNT and all of them exhibit winged structure and the overall yield of the process is high. Additionally, we also found that the graphene wings were strongly attached to the nanotubes as the winged structure was preserved even after a prolonged sonication process (>10 hours).

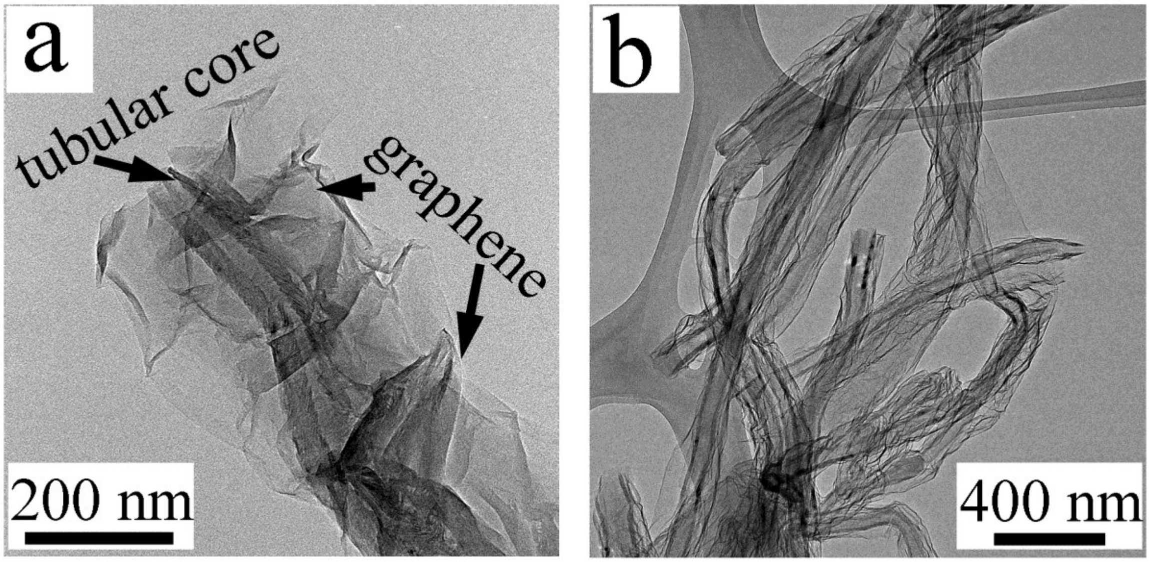

Figure 6.5: TEM images of the winged carbon nanotubes.

Upon unzipping and exfoliation, the specific surface area increased from ~ 40 m^2/g for pristine SC-CNT to ~ 480 m^2/g for wNT. Considering the fact that the solid inner tubular cores of wNT won't contribute much to this measurement, the exfoliated graphene wings should have specific surface area close to the theoretical value of single layer graphene (2630 m^2/g).[203] More significantly, they will not restack owning to the unique core-shell structure. Restacking is a common problem for graphene materials upon drying due to their strong van der Walls interactions and will result in significantly decreased surface area.[204] On the basis of X-ray photoelectron spectroscopy (XPS) analysis (Figure 6.6), a nominal ~30 at% of oxygen was identified in the ox-NT in the form of hybroxyl, carbonyl and carboxyl groups that is indicative of abundant defective and functionalized sites.[179]

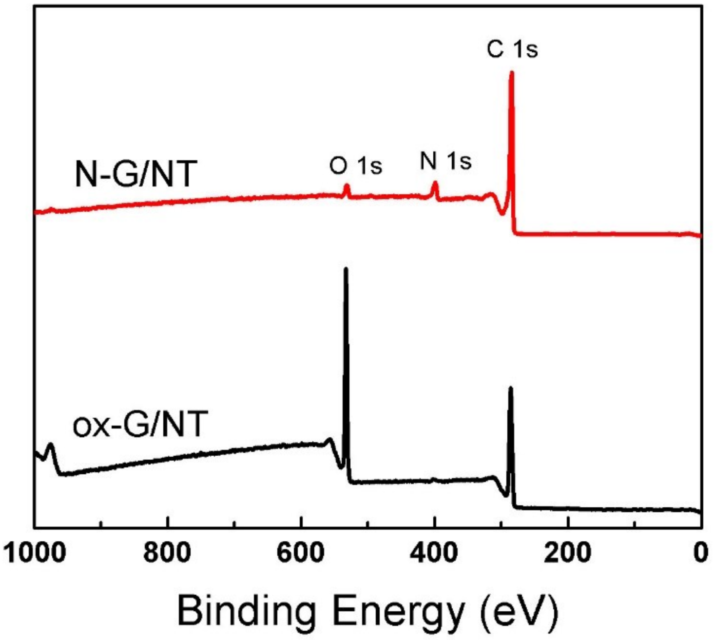

Figure 6.6: Survey XPS spectra for nitrogen doped (N-wNT) and as-oxidized (ox-NT) winged carbon nanotubes.

Subsequently, the ox-NT were doped with nitrogen using a method similarly as described by Müllen et al.[200] In this method, solid and homogeneous mixture of ox-NT and cyanamide was firstly annealed at 550°C under Ar to thermally condense cyanamide and provide polymeric carbon nitride (CN).[205] Afterwards the mixture was heated to 900°C to decompose CN and generate nitrogen doped wNT (N-wNT).[200] The morphology and structure of the N-wNT investigated by TEM (Figure 6.8) revealed that they resemble that of wNT as shown in Figure 6.6, indicating that the doping process did not affect their winged structure.

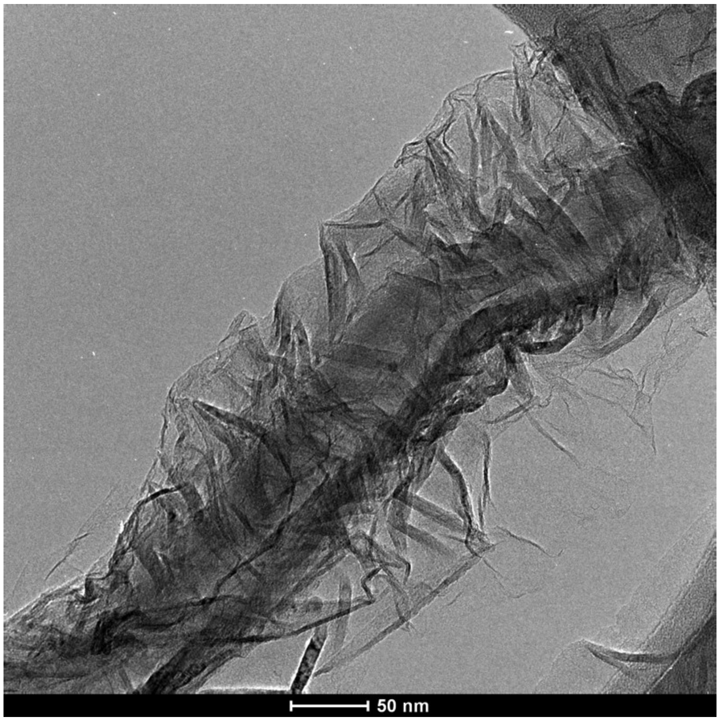

Figure 6.7: TEM image of the nitrogen doped winged nanotubes. The winged structure is preserved during the doping process.

Along with the doping process, most oxygen functionalities were removed with the oxygen level reduced significantly to only ~ 2.6 at%. In the meantime, nitrogen was successfully doped with a nominal concentration of 6.6 at% (Figure 6.6), which is similar with previous studies on N-doped GO.[206] Analysis of N 1s spectra revealed the presence of both pyridinic and graphitic nitrogen, corresponding to binding energies of 398.4 and 401.0 eV, respectively (Figure 6.8). The nitrogen doping was believed to result from reactions of CN with oxygen functionalities and other defects in the heavily oxidized graphene wings of the ox-NT complexes. Noticeably, no metallic species were detected in either ox-NT or N-wNT.

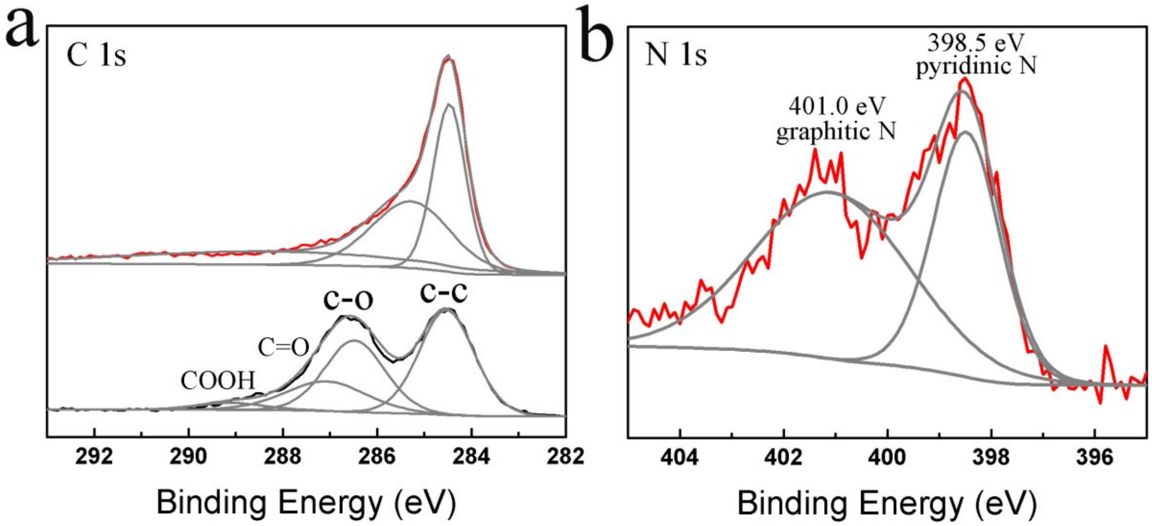

Figure 6.8: Compositional characterization using XPS: (a) C 1s regional spectra of as-synthesized ox-NT (black) and final N-wNT catalyst (red). (b) High-resolution N 1s spectra of N-wNT.

We performed cyclic voltammetry (CV) and rotating disk electrode (RDE) measurements in 0.1M KOH to assess the ORR activity of N-wNT material that had been deposited onto a glassy carbon electrode. The N-wNT catalyst exhibited a symmetrical and rectangular CV curve originated from the double layer capacitance when the electrolyte was saturated with Ar (Figure 6.9). In strong contrast, a pronounced catholic ORR peak with an onset voltage of ~0.91 V versus reversible hydrogen electrode (RHE) was observed in O_2 saturated electrolyte. Noticeably, the ORR peak is much stronger with more positive onset voltage than most of the metal-free catalyst developed,[193, 200, 207] suggesting excellent catalytic activity of the N-doped winged nanotubes.

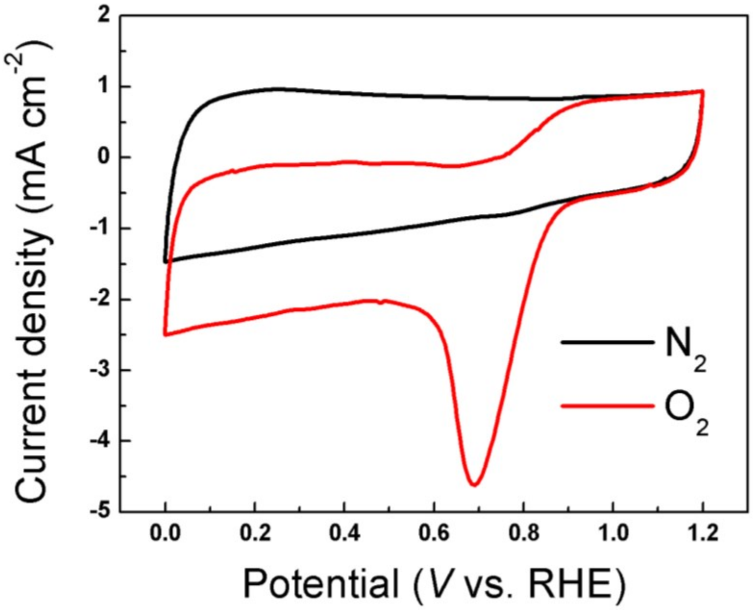

Figure 6.9: CV curves of the N-wNT electrocatalyst acquired at 100 mV/s in O_2 or Ar saturated 0.1M KOH.

The high ORR activity is also evident from its onset potential (~ 0.93 V) and half-wave potential (~0.79 V) in the RDE polarization curve as shown in Figure 6.10. The corresponding Koutecky-Levich plot (J^{-1} vs $\omega^{-1/2}$) obtained on the basis of analyzing the RDE curves of different electrode rotating speeds (in rpm, Figure 6.10) at various potentials exhibited excellent linearity (Figure 6.6c). The average number of electrons transferred per oxygen molecule involved in the ORR can be analyzed on the basis of the Koutecky-Levich equations:[187]

$$\frac{1}{J} = \frac{1}{J_L} + \frac{1}{J_K} = \frac{1}{B\omega^{1/2}} + \frac{1}{J_K}$$

$$B = 0.2nFC_oD_o^{2/3}v^{-1/6}$$

in which J is the measured current density, J_L and J_K are the diffusion- and kinetic-limiting current densities. ω is the linear rotating speed of RDE in rpm. n is the overall number of electrons transferred in the ORR, F is the Faradic constant 96485 C mol^{-1}, D is the diffusion coefficient of O_2 in the electrolyte 1.73×10^{-5} cm^2 s^{-1}, V is the kinematic viscosity of the electrolyte 0.01 cm^{2}s^{-1}, C_o is the concentration of oxygen 1.21×10^{-6} mol L^{-1}. The electron transfer numbers determined were all around 4 at different potentials being examined (Figure 3c, inserted), demonstrated that N-wNT are highly efficient and catalyzing ORR though the four-electrons pathway with oxygen directly reduced to water. The kinetic limiting currents were 12.5 mA cm^{-2} at 0.4 V and 14.2 mA cm^{-2} at 1.0 V, indicating that highly active catalyst. The N-wNT were free from metal species as discussed above, which enables a solid correlation between their core-shell structure characteristics and electrochemical performance.

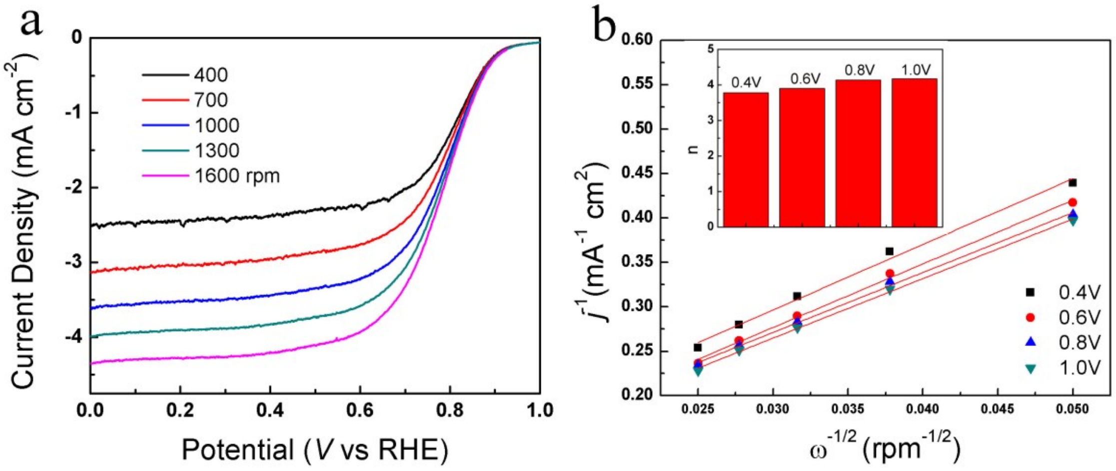

Figure 6.10 (a) Rotating-disk voltammograms in O$_2$-saturated 0.1M KOH at 10 mV/s and different rotating speeds. (b) Koutecky-Levich plots of J^{-1} versus $\omega^{-1/2}$ and number of electrons transferred (inserted image) at different electrode potentials.

The effects of structure and composition on the ORR activity of the catalysts were also studied. Figure 6.11 compares the RDE voltammograms (acquired at 10 mV/s and 1600 rpm in 0.1M O$_2$-saturated KOH) of the N-wNT catalyst with control catalysts including N-doped graphene and N-doped physical mixture of graphene and functionalized nanotube (N-G/fCNT, without strong coupling). As can be seen, both N-graphene (E_o=0.84V) and N-G/fCNT (E_o=0.87V) showed inferior activity compared with N-wNT with more negative onset voltages and lower steady state currents. These results demonstrated the advantages of the winged structures with strongly coupled graphene wings and inner tubes on improved catalytic activities: whereas the doped graphene wings bring catalytic activity with maximized active site density, the inner tubes remain intact and conductive and could facilitate electron transport during electrocatalysis.

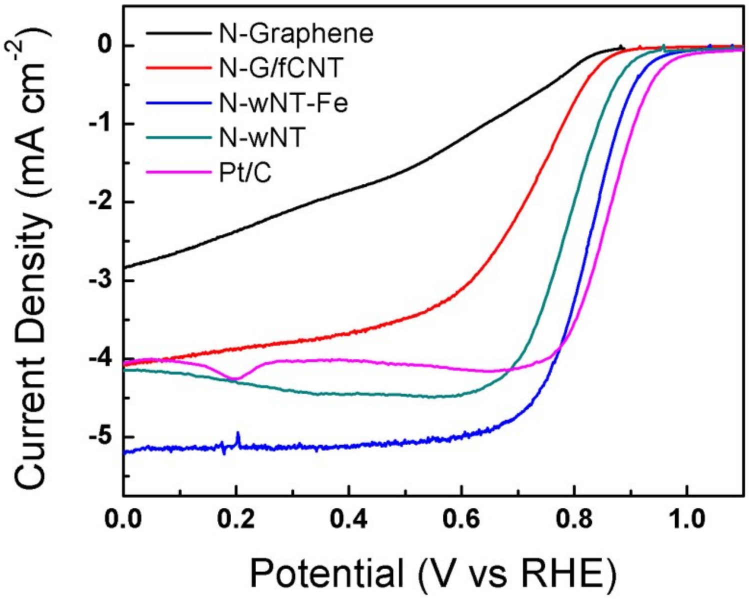

Figure 6.11: Comparison of the RDE voltammograms for catalysts with different structures and compositions as specified (all acquired at 1600 rpm and 10 mV/s)

The results discussed above demonstrated that the N-wNT catalysts have remarkable activity as metal-free electrocatalysts for the ORR. Non-precious metals, such as Fe and Co, have been identified to be able to enhance the activity of ORR catalysts.[200, 208] In this study, Fe was intentionally incorporated with ~0.9 at% to the N-wNT catalyst (Figure 6.7) through an in-situ process. The N-wNT-Fe catalyst exhibited enhanced catalysis activity with onset potential (~0.95V) and half-wave potential ($E_{1/2}$=0.83V) close to that of Pt/C (E_o=0.98V, $E_{1/2}$=0.86V). More significantly, the N-wNT-Fe has higher current density than either N-wNT or Pt/C (Figure 6.6d). These results indicate that the winged CNTs could also be used as high performance ORR catalysts support.

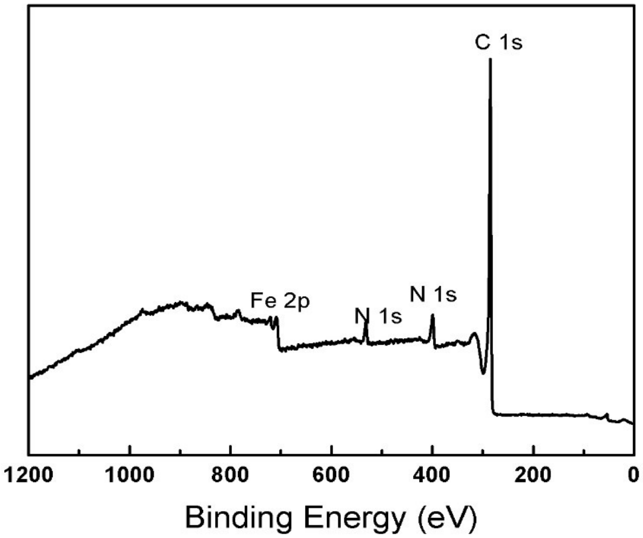

Figure 6.12: XPS Survey spectrum of the N-wNT-Fe catalyst.

The N-wNT catalyst was further tested for possible fuel crossover and poisoning effects in the presence of methanol and CO, respectively. For comparison, the activity of Pt/C was also studied under the same conditions. The strong amperometric response of N-wNT was very stable upon introduction of 1M methanol (Figure 6.8a), indicating that the catalyst has high selectivity towards the ORR against the electrooxidation of methanol. In contrast, more than 40% of the initial electrocatalytic current was lost for Pt/C. The high selectivity could be attribute to the lower ORR potential than that required for oxidization of methanol using the N-wNT catalyst.[185] The effect of CO on the electrocatalytic activity of N-wNT was also tested since CO poisoning is a major concern for noble-metal catalysts. Being nonmetallic, the activity of N-wNT was relatively stable even with 10% (v/v) CO (Figure 6.6b), whereas the Pt/C catalyst was rapidly poisoned with dramatically decreased current density (~40% within 300s).

Hence, it is clear that the N-wNT catalyst have excellent tolerance for both methanol and CO, indicating high selectivity toward catalyzing the ORR.

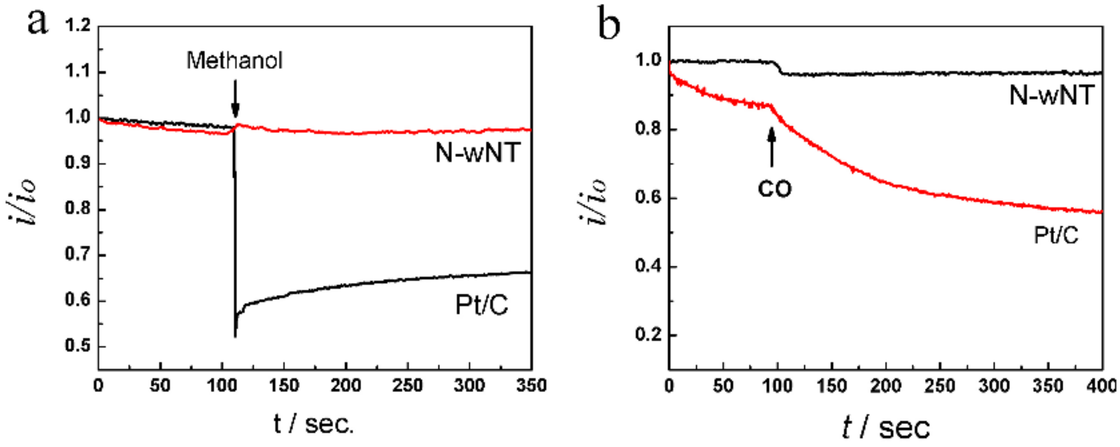

Figure 6.13 Comparion of the tolerance and durability of the N-wNT catalyst with Pt/C: (a) with the presence of 1M methanol (b) 10% (v/v) carbon monoxide.

The long-term stability of the catalyst was also examined and compared with Pt/C by recording the current at 0.5 V and 1600 rpm and the current retentions were compared in Figure 6.6c. The N-wNT catalyst exhibited excellent stability and is better than commercial Pt/C catalyst.

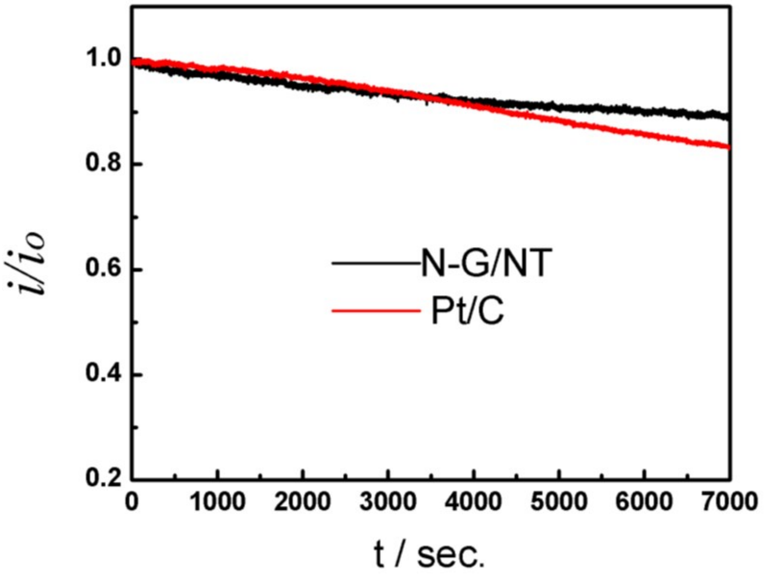

Figure 6.14: Comparison of the durability of the N-wNT catalyst with Pt/C

6.4 Conclusion

In summary, we developed a facile strategy to prepare winged carbon nanotubes with strongly attached graphene wings and demonstrated their promising applications as electrocatalysts. After doping with nitrogen, the wNT exhibited high activity and efficiency, excellent selectivity and superior stability toward catalyzing the ORR through the 4-electron transfer pathway. Such high activity can be attributed to the unique and strongly coupling between graphene and nanotube in the wNT that bring increased surface area, good electrical and mechanical properties and porosity. In addition to their promising applications as metal-free catalyst, the N-wNT can also be used as catalyst support with improved efficiency and durability. Hence, the work described in this work could represent a general approach to highly efficient and durable electrocatalysts for a range of important electrochemical reactions.

References

1. *Basic research needs for electrical energy storage: report of the basic energy sciences workshop on electrical energy storage*; US Deparment of Energy: 2007.

2. Yang, Z. G.; Zhang, J. L.; Kintner-Meyer, M. C. W.; Lu, X. C.; Choi, D. W.; Lemmon, J. P.; Liu, J. *Chem Rev* **2011,** 111, (5), 3577-3613.

3. Dillon, A. C. *Chem Rev* **2010,** 110, (11), 6856-6872.

4. Zhang, L. L.; Zhao, X. S. *Chem Soc Rev* **2009,** 38, (9), 2520-2531.

5. Stamm, K. R.; Clark, F.; Eblacas, P. R. *Public Underst Sci* **2000,** 9, (3), 219-237.

6. Bentley, R. W. *Energ Policy* **2002,** 30, (3), 189-205.

7. Arunachalam, V. S.; Fleischer, E. L. *Mrs Bull* **2008,** 33, (4), 264-276.

8. Khaligh, A.; Li, Z. H. *Ieee T Veh Technol* **2010,** 59, (6), 2806-2814.

9. Kang, B.; Ceder, G. *Nature* **2009,** 458, (7235), 190-193.

10. Winter, M.; Brodd, R. J. *Chem Rev* **2004,** 104, (10), 4245-4269.

11. Kotz, R.; Carlen, M. *Electrochim Acta* **2000,** 45, (15-16), 2483-2498.

12. Frackowiak, E.; Beguin, F. *Carbon* **2002,** 40, (10), 1775-1787.

13. Pumera, M. *Energ Environ Sci* **2011,** 4, (3), 668-674.

14. Reilly, R. M. *J Nucl Med* **2007,** 48, (7), 1039-1042.

15. Iijima, S. *Nature* **1991,** 354, (6348), 56-58.

16. Ando, T. *Npg Asia Mater* **2009,** 1, (1), 17-21.

17. Hou, Y.; Tang, J.; Zhang, H. B.; Qian, C.; Feng, Y. Y.; Liu, J. *Acs Nano* **2009,** 3, (5), 1057-1062.

18. Berber, S.; Kwon, Y. K.; Tomanek, D. *Phys Rev Lett* **2000,** 84, (20), 4613-4616.

19. Yao, Z.; Kane, C. L.; Dekker, C. *Phys Rev Lett* **2000,** 84, (13), 2941-2944.

20. Peng, B.; Locascio, M.; Zapol, P.; Li, S. Y.; Mielke, S. L.; Schatz, G. C.; Espinosa, H. D. *Nat Nanotechnol* **2008,** 3, (10), 626-631.

21. Hong, S.; Myung, S. *Nat Nanotechnol* **2007,** 2, (4), 207-208.

22. Pop, E.; Mann, D.; Wang, Q.; Goodson, K. E.; Dai, H. J. *Nano Lett* **2006,** 6, (1), 96-100.

23. Journet, C.; Maser, W. K.; Bernier, P.; Loiseau, A.; delaChapelle, M. L.; Lefrant, S.; Deniard, P.; Lee, R.; Fischer, J. E. *Nature* **1997,** 388, (6644), 756-758.

24. Scott, C. D.; Arepalli, S.; Nikolaev, P.; Smalley, R. E. *Appl Phys a-Mater* **2001,** 72, (5), 573-580.

25. Liu, J.; Rinzler, A. G.; Dai, H. J.; Hafner, J. H.; Bradley, R. K.; Boul, P. J.; Lu, A.; Iverson, T.; Shelimov, K.; Huffman, C. B.; Rodriguez-Macias, F.; Shon, Y. S.; Lee, T. R.; Colbert, D. T.; Smalley, R. E. *Science* **1998,** 280, (5367), 1253-1256.

26. Yuan, L. M.; Saito, K.; Hu, W. C.; Chen, Z. *Chem Phys Lett* **2001,** 346, (1-2), 23-28.

27. Li, Y. M.; Mann, D.; Rolandi, M.; Kim, W.; Ural, A.; Hung, S.; Javey, A.; Cao, J.; Wang, D. W.; Yenilmez, E.; Wang, Q.; Gibbons, J. F.; Nishi, Y.; Dai, H. J. *Nano Lett* **2004,** 4, (2), 317-321.

28. Terrones, M. *Annu Rev Mater Res* **2003,** 33, 419-501.

29. Joselevich, E.; Dai, H. J.; Liu, J.; Hata, K.; Windle, A. H. *Top Appl Phys* **2008,** 111, 101-164.

30. Hirsch, A. *Angew Chem Int Edit* **2002,** 41, (11), 1853-1859.

31. Zhu, Y. W.; Murali, S.; Cai, W. W.; Li, X. S.; Suk, J. W.; Potts, J. R.; Ruoff, R. S. *Adv Mater* **2010,** 22, (35), 3906-3924.

32. Hummers, W. S.; Offeman, R. E. *J Am Chem Soc* **1958,** 80, (6), 1339-1339.

33. He, H. Y.; Klinowski, J.; Forster, M.; Lerf, A. *Chem Phys Lett* **1998,** 287, (1-2), 53-56.

34. Stankovich, S.; Dikin, D. A.; Piner, R. D.; Kohlhaas, K. A.; Kleinhammes, A.; Jia, Y.; Wu, Y.; Nguyen, S. T.; Ruoff, R. S. *Carbon* **2007,** 45, (7), 1558-1565.

35. Long, J. W.; Belanger, D.; Brousse, T.; Sugimoto, W.; Sassin, M. B.; Crosnier, O. *Mrs Bull* **2011,** 36, (7), 513-522.

36. Conway, B. E., *Electrochemical Supercapacitors: Scientific Fundamentals and Technological Applications*. Springer: 1999.

37. Rightmire, R. 1966.

38. Taberna, P. L.; Chevallier, G.; Simon, P.; Plee, D.; Aubert, T. *Mater Res Bull* **2006,** 41, (3), 478-484.

39. Frackowiak, E.; Metenier, K.; Bertagna, V.; Beguin, F. *Appl Phys Lett* **2000,** 77, (15), 2421-2423.

40. Zhu, Y. W.; Murali, S.; Stoller, M. D.; Ganesh, K. J.; Cai, W. W.; Ferreira, P. J.; Pirkle, A.; Wallace, R. M.; Cychosz, K. A.; Thommes, M.; Su, D.; Stach, E. A.; Ruoff, R. S. *Science* **2011,** 332, (6037), 1537-1541.

41. Niu, C. M.; Sichel, E. K.; Hoch, R.; Moy, D.; Tennent, H. *Appl Phys Lett* **1997,** 70, (11), 1480-1482.

42. Wang, G. P.; Zhang, L.; Zhang, J. J. *Chem Soc Rev* **2012,** 41, (2), 797-828.

43. Wu, Z. S.; Zhou, G. M.; Yin, L. C.; Ren, W.; Li, F.; Cheng, H. M. *Nano Energy* **2012,** 1, (1), 107-131.

44. Choi, D.; Blomgren, G. E.; Kumta, P. N. *Adv Mater* **2006,** 18, (9), 1178-+.

45. Nyholm, L.; Nystrom, G.; Mihranyan, A.; Stromme, M. *Adv Mater* **2011,** 23, (33), 3751-3769.

46. Simon, P.; Gogotsi, Y. *Nat Mater* **2008,** 7, (11), 845-854.

47. Conway, B. E. *J Electrochem Soc* **1991,** 138, (6), 1539-1548.

48. Zheng, J. P.; Cygan, P. J.; Jow, T. R. *J Electrochem Soc* **1995,** 142, (8), 2699-2703.

49. Lee, H. Y.; Goodenough, J. B. *J Solid State Chem* **1999,** 144, (1), 220-223.

50. Xu, C. J.; Kang, F. Y.; Li, B. H.; Du, H. D. *J Mater Res* **2010,** 25, (8), 1421-1432.

51. Wei, W. F.; Cui, X. W.; Chen, W. X.; Ivey, D. G. *Chem Soc Rev* **2011,** 40, (3), 1697-1721.

52. Xu, C. J.; Li, B. H.; Du, H. D.; Kang, F. Y.; Zeng, Y. Q. *J Power Sources* **2008,** 180, (1), 664-670.

53. Ragupathy, P.; Vasan, H. N.; Munichandraiah, N. *J Electrochem Soc* **2008,** 155, (1), A34-A40.

54. Cheng, J.; Cao, G. P.; Yang, Y. S. *J Power Sources* **2006,** 159, (1), 734-741.

55. Cao, C. Y.; Guo, W.; Cui, Z. M.; Song, W. G.; Cai, W. *J Mater Chem* **2011,** 21, (9), 3204-3209.

56. Woo, S. W.; Dokko, K.; Kanamura, K. *J Power Sources* **2008,** 185, (2), 1589-1593.

57. Rolison, D. R.; Long, R. W.; Lytle, J. C.; Fischer, A. E.; Rhodes, C. P.; McEvoy, T. M.; Bourga, M. E.; Lubers, A. M. *Chem Soc Rev* **2009,** 38, (1), 226-252.

58. Hou, Y.; Cheng, Y. W.; Hobson, T.; Liu, J. *Nano Lett* **2010,** 10, (7), 2727-2733.

59. Lu, X.; Zhai, T.; Zhang, X.; Shen, Y.; Yuan, L.; Hu, B.; Gong, L.; Chen, J.; Gao, Y.; Zhou, J.; Tong, Y.; Wang, Z. L. *Adv Mater* **2012,** 24, (7), 938-44.

60. Broughton, J. N.; Brett, M. J. *Electrochim Acta* **2005,** 50, (24), 4814-4819.

61. Wei, W. F.; Cui, X. W.; Chen, W. X.; Ivey, D. G. *J Phys Chem C* **2008,** 112, (38), 15075-15083.

62. Kang, Y. J.; Kim, B.; Chung, H.; Kim, W. *Synthetic Met* **2010,** 160, (23-24), 2510-2514.

63. Chen, W.; Rakhi, R. B.; Hu, L. B.; Xie, X.; Cui, Y.; Alshareef, H. N. *Nano Lett* **2011,** 11, (12), 5165-5172.

64. Hu, L. B.; Chen, W.; Xie, X.; Liu, N. A.; Yang, Y.; Wu, H.; Yao, Y.; Pasta, M.; Alshareef, H. N.; Cui, Y. *Acs Nano* **2011,** 5, (11), 8904-8913.

65. Yu, G. H.; Hu, L. B.; Vosgueritchian, M.; Wang, H. L.; Xie, X.; McDonough, J. R.; Cui, X.; Cui, Y.; Bao, Z. N. *Nano Lett* **2011,** 11, (7), 2905-2911.

66. Bao, L. H.; Li, X. D. *Adv Mater* **2012,** 24, (24), 3246-3252.

67. Izadi-Najafabadi, A.; Yamada, T.; Futaba, D. N.; Yudasaka, M.; Takagi, H.; Hatori, H.; Iijima, S.; Hata, K. *Acs Nano* **2011,** 5, (2), 811-819.

68. Chen, Y. C.; Hsu, Y. K.; Lin, Y. G.; Lin, Y. K.; Horng, Y. Y.; Chen, L. C.; Chen, K. H. *Electrochim Acta* **2011,** 56, (20), 7124-7130.

69. Yuan, L. Y.; Lu, X. H.; Xiao, X.; Zhai, T.; Dai, J. J.; Zhang, F. C.; Hu, B.; Wang, X.; Gong, L.; Chen, J.; Hu, C. G.; Tong, Y. X.; Zhou, J.; Wang, Z. L. *Acs Nano* **2012,** 6, (1), 656-661.

70. Bao, L. H.; Zang, J. F.; Li, X. D. *Nano Lett* **2011,** 11, (3), 1215-1220.

71. Yang, P.; Xiao, X.; Li, Y.; Ding, Y.; Qiang, P.; Tan, X.; Mai, W.; Lin, Z.; Wu, W.; Li, T.; Jin, H.; Liu, P.; Zhou, J.; Wong, C. P.; Wang, Z. L. *Acs Nano* **2013,** 7, (3), 2617-26.

72. Chou, S. L.; Wang, J. Z.; Chew, S. Y.; Liu, H. K.; Dou, S. X. *Electrochem Commun* **2008,** 10, (11), 1724-1727.

73. He, Y.; Chen, W.; Li, X.; Zhang, Z.; Fu, J.; Zhao, C.; Xie, E. *Acs Nano* **2013,** 7, (1), 174-182.

74. Li, Z. P.; Mi, Y. J.; Liu, X. H.; Liu, S.; Yang, S. R.; Wang, J. Q. *J Mater Chem* **2011,** 21, (38), 14706-14711.

75. Gogotsi, Y.; Simon, P. *Science* **2011,** 334, (6058), 917-918.

76. Cheng, Y. W.; Lu, S. T.; Zhang, H. B.; Varanasi, C. V.; Liu, J. *Nano Lett* **2012,** 12, (8), 4206-4211.

77. Yuan, C. Z.; Hou, L. R.; Li, D. K.; Shen, L. F.; Zhang, F.; Zhang, X. G. *Electrochim Acta* **2011,** 56, (19), 6683-6687.

78. Boukhalfa, S.; Evanoff, K.; Yushin, G. *Energ Environ Sci* **2012,** 5, (5), 6872-6879.

79. Chou, S. L.; Wang, J. Z.; Liu, H. K.; Dou, S. X. *J Electrochem Soc* **2008,** 155, (12), A926-A929.

80. Perera, S. D.; Patel, B.; Nijem, N.; Roodenko, K.; Seitz, O.; Ferraris, J. P.; Chabal, Y. J.; Balkus, K. J. *Adv Energy Mater* **2011,** 1, (5), 936-945.

81. Zhang, X. J.; Shi, W. H.; Zhu, J. X.; Kharistal, D. J.; Zhao, W. Y.; Lalia, B. S.; Hng, H. H.; Yan, Q. Y. *Acs Nano* **2011,** 5, (3), 2013-2019.

82. Chen, P. C.; Shen, G. Z.; Shi, Y.; Chen, H. T.; Zhou, C. W. *Acs Nano* **2010,** 4, (8), 4403-4411.

83. Wu, Z. S.; Ren, W. C.; Wang, D. W.; Li, F.; Liu, B. L.; Cheng, H. M. *Acs Nano* **2010,** 4, (10), 5835-5842.

84. Shao, Y. L.; Wang, H. Z.; Zhang, Q. H.; Li, Y. G. *J Mater Chem C* **2013,** 1, (6), 1245-1251.

85. Lu, X. H.; Yu, M. H.; Wang, G. M.; Zhai, T.; Xie, S. L.; Ling, Y. C.; Tong, Y. X.; Li, Y. *Adv Mater* **2013,** 25, (2), 267-272.

86. Choi, B. G.; Chang, S. J.; Kang, H. W.; Park, C. P.; Kim, H. J.; Hong, W. H.; Lee, S.; Huh, Y. S. *Nanoscale* **2012,** 4, (16), 4983-4988.

87. Belanger, D.; Brousse, T.; Long, J. W. *Electrochem. Soc. Interf.* **2008**, (17), 49-52.

88. Toupin, M.; Brousse, T.; Belanger, D. *Chem Mater* **2004,** 16, (16), 3184-3190.

89. Pang, S. C.; Anderson, M. A.; Chapman, T. W. *J Electrochem Soc* **2000,** 147, (2), 444-450.

90. Broughton, J. N.; Brett, M. J. *Electrochim Acta* **2004,** 49, (25), 4439-4446.

91. Lang, X.; Hirata, A.; Fujita, T.; Chen, M. *Nature Nanotechnology* **2011**.

92. Zhang, H.; Cao, G. P.; Wang, Z. Y.; Yang, Y. S.; Shi, Z. J.; Gu, Z. N. *Nano Lett* **2008,** 8, (9), 2664-2668.

93. Kim, J.-H.; Lee, K. H.; Overzet, L. J.; Lee, G. S. *Nano Lett* **2011,** 11, (7), 2611-7.

94. Fischer, A. E.; Pettigrew, K. A.; Rolison, D. R.; Stroud, R. M.; Long, J. W. *Nano Lett* **2007,** 7, (2), 281-286.

95. Zhang, L. L.; Wei, T. X.; Wang, W. J.; Zhao, X. S. *Micropor Mesopor Mat* **2009,** 123, (1-3), 260-267.

96. Dong, X. P.; Shen, W. H.; Gu, J. L.; Xiong, L. M.; Zhu, Y. F.; Li, Z.; Shi, J. L. *Journal of Physical Chemistry B* **2006,** 110, (12), 6015-6019.

97. Yan, J.; Fan, Z. J.; Wei, T.; Qian, W. Z.; Zhang, M. L.; Wei, F. *Carbon* **2010,** 48, (13), 3825-3833.

98. Chen, S.; Zhu, J. W.; Wu, X. D.; Han, Q. F.; Wang, X. *Acs Nano* **2010,** 4, (5), 2822-2830.

99. Zhao, J. P.; Pei, S. F.; Ren, W. C.; Gao, L. B.; Cheng, H. M. *Acs Nano* **2010,** 4, (9), 5245-5252.

100. Li, D.; Muller, M. B.; Gilje, S.; Kaner, R. B.; Wallace, G. G. *Nat Nanotechnol* **2008,** 3, (2), 101-105.

101. Qian, C.; Qi, H.; Gao, B.; Cheng, Y.; Qiu, Q.; Qin, L. C.; Zhou, O.; Liu, J. *Journal of Nanoscience and Nanotechnology* **2006,** 6, (5), 1346-1349.

102. Toupin, M.; Brousse, T.; Belanger, D. *Chem Mater* **2002,** 14, (9), 3946-3952.

103. Moon, I. K.; Lee, J.; Ruoff, R. S.; Lee, H. *Nature Communications* **2010,** 1, -.

104. Chigane, M.; Ishikawa, M. *J Electrochem Soc* **2000,** 147, (6), 2246-2251.

105. Wang, J. Z.; Zhong, C.; Chou, S. L.; Liu, H. K. *Electrochem Commun* **2010,** 12, (11), 1467-1470.

106. Liu, J. F.; Luo, D. C.; Zhang, G. X.; Sun, X. M. *J Phys Chem C* **2011,** 115, (23), 11327-11335.

107. Belanger, D.; Brousse, T.; Long, J. W. *The Electrochemical Society Interface* **2008,** 17, 49-52.

108. Lang, X. Y.; Hirata, A.; Fujita, T.; Chen, M. W. *Nat Nanotechnol* **2011,** 6, (4), 232-236.

109. Kim, J. H.; Lee, K. H.; Overzet, L. J.; Lee, G. S. *Nano Lett* **2011,** 11, (7), 2611-2617.

110. Subramanian, V.; Zhu, H. W.; Wei, B. Q. *J Power Sources* **2006,** 159, (1), 361-364.

111. Chou, S. L.; Wang, J. Z.; Chew, S. Y.; Liu, H. K.; Dou, S. X. *Electrochem Commun* **2008,** 10, (11), 1724-1727.

112. El-Kady, M. F.; Strong, V.; Dubin, S.; Kaner, R. B. *Science* **2012,** 335, (6074), 1326-1330.

113. Hu, L. B.; Chen, W.; Xie, X.; Liu, N. A.; Yang, Y.; Wu, H.; Yao, Y.; Pasta, M.; Alshareef, H. N.; Cui, Y. *Acs Nano* **2011,** 5, (11), 8904-8913.

114. Yu, G. H.; Hu, L. B.; Liu, N. A.; Wang, H. L.; Vosgueritchian, M.; Yang, Y.; Cui, Y.; Bao, Z. A. *Nano Lett* **2011,** 11, (10), 4438-4442.

115. Yu, G. H.; Hu, L. B.; Vosgueritchian, M.; Wang, H. L.; Xie, X.; McDonough, J. R.; Cui, X.; Cui, Y.; Bao, Z. N. *Nano Lett* **2011,** 11, (7), 2905-2911.

116. Wu, Z.-S.; Zhou, G.; Yin, L.-C.; Ren, W.; Li, F.; Cheng, H. M. *Nano Energy* **2012,** 1, (1), 107-131.

117. Hou, Y.; Cheng, Y. W.; Hobson, T.; Liu, J. *Nano Lett* **2010,** 10, (7), 2727-2733.

118. Zhang, J. T.; Jiang, J. W.; Zhao, X. S. *J Phys Chem C* **2011,** 115, (14), 6448-6454.

119. Yan, J.; Fan, Z. J.; Wei, T.; Qian, W. Z.; Zhang, M. L.; Wei, F. *Carbon* **2010,** 48, (13), 3825-3833.

120. Li, Z. P.; Mi, Y. J.; Liu, X. H.; Liu, S.; Yang, S. R.; Wang, J. Q. *J Mater Chem* **2011,** 21, (38), 14706-14711.

121. Qiu, L.; Yang, X.; Gou, X.; Yang, W.; Ma, Z. F.; Wallace, G. G.; Li, D. *Chemistry - A European Journal* **2010,** 16, (35), 10653-10658.

122. Niu, Z. Q.; Zhou, W. Y.; Chen, J.; Feng, G. X.; Li, H.; Ma, W. J.; Li, J. Z.; Dong, H. B.; Ren, Y.; Zhao, D. A.; Xie, S. S. *Energ Environ Sci* **2011,** 4, (4), 1440-1446.

123. Futaba, D. N.; Hata, K.; Yamada, T.; Hiraoka, T.; Hayamizu, Y.; Kakudate, Y.; Tanaike, O.; Hatori, H.; Yumura, M.; Iijima, S. *Nat Mater* **2006,** 5, (12), 987-994.

124. Bao, L. H.; Zang, J. F.; Li, X. D. *Nano Lett* **2011,** 11, (3), 1215-1220.

125. Kang, Y. J.; Kim, B.; Chung, H.; Kim, W. *Synthetic Met* **2010,** 160, (23-24), 2510-2514.

126. Fan, Z. J.; Yan, J.; Wei, T.; Zhi, L. J.; Ning, G. Q.; Li, T. Y.; Wei, F. *Adv Funct Mater* **2011,** 21, (12), 2366-2375.

127. Cottineau, T.; Toupin, M.; Delahaye, T.; Brousse, T.; Belanger, D. *Appl Phys a-Mater* **2006,** 82, (4), 599-606.

128. Demarconnay, L.; Raymundo-Pinero, E.; Beguin, F. *J Power Sources* **2011,** 196, (1), 580-586.

129. Brousse, T.; Taberna, P. L.; Crosnier, O.; Dugas, R.; Guillemet, P.; Scudeller, Y.; Zhou, Y.; Favier, F.; Belanger, D.; Simon, P. *J Power Sources* **2007,** 173, (1), 633-641.

130. Khomenko, V.; Raymundo-Pinero, E.; Frackowiak, E.; Beguin, F. *Appl Phys a-Mater* **2006,** 82, (4), 567-573.

131. Wang, H. L.; Liang, Y. Y.; Mirfakhrai, T.; Chen, Z.; Casalongue, H. S.; Dai, H. J. *Nano Res* **2011,** 4, (8), 729-736.

132. Lang, J. W.; Kong, L. B.; Liu, M.; Luo, Y. C.; Kang, L. *J Solid State Electr* **2010,** 14, (8), 1533-1539.

133. Brousse, T.; Toupin, M.; Belanger, D. *J Electrochem Soc* **2004,** 151, (4), A614-A622.

134. Qu, Q. T.; Shi, Y.; Tian, S.; Chen, Y. H.; Wu, Y. P.; Holze, R. *J Power Sources* **2009,** 194, (2), 1222-1225.

135. Kim, J. H.; Lee, K. H.; Overzet, L. J.; Lee, G. S. *Nano Lett* **2011,** 11, (7), 2611-2617.

136. Hu, L. B.; Wu, H.; La Mantia, F.; Yang, Y. A.; Cui, Y. *Acs Nano* **2010,** 4, (10), 5843-5848.

137. Kaempgen, M.; Chan, C. K.; Ma, J.; Cui, Y.; Gruner, G. *Nano Lett* **2009,** 9, (5), 1872-1876.

138. Jia, X. L.; Chen, Z.; Suwarnasarn, A.; Rice, L.; Wang, X. L.; Sohn, H.; Zhang, Q.; Wu, B. M.; Wei, F.; Lu, Y. F. *Energ Environ Sci* **2012,** 5, (5), 6845-6849.

139. Wang, D. W.; Li, F.; Zhao, J. P.; Ren, W. C.; Chen, Z. G.; Tan, J.; Wu, Z. S.; Gentle, I.; Lu, G. Q.; Cheng, H. M. *Acs Nano* **2009,** 3, (7), 1745-1752.

140. Brozena, A. H.; Moskowitz, J.; Shao, B. Y.; Deng, S. L.; Liao, H. W.; Gaskell, K. J.; Wang, Y. H. *J Am Chem Soc* **2010,** 132, (11), 3932-3938.

141. Portet, C.; Taberna, P. L.; Simon, P.; Flahaut, E. *J Power Sources* **2005,** 139, (1-2), 371-378.

142. Fan, Z. J.; Yan, J.; Wei, T.; Zhi, L. J.; Ning, G. Q.; Li, T. Y.; Wei, F. *Adv Funct Mater* **2011,** 21, (12), 2366-2375.

143. Obreja, V. V. N. *Physica E* **2008,** 40, (7), 2596-2605.

144. Qu, Q. T.; Zhang, P.; Wang, B.; Chen, Y. H.; Tian, S.; Wu, Y. P.; Holze, R. *J Phys Chem C* **2009,** 113, (31), 14020-14027.

145. Liu, C.; Li, F.; Ma, L. P.; Cheng, H. M. *Adv Mater* **2010,** 22, (8), E28-+.

146. Hu, W. K.; Noreus, D. *Chem Mater* **2003,** 15, (4), 974-978.

147. Oliva, P.; Leonardi, J.; Laurent, J. F.; Delmas, C.; Braconnier, J. J.; Figlarz, M.; Fievet, F.; Deguibert, A. *J Power Sources* **1982,** 8, (2-3), 229-255.

148. Motori, A.; Sandrolini, F.; Davolio, G. *J Power Sources* **1994,** 48, (3), 361-370.

149. Wang, H. L.; Casalongue, H. S.; Liang, Y. Y.; Dai, H. J. *J Am Chem Soc* **2010,** 132, (21), 7472-7477.

150. Wang, Y. G.; Yu, L.; Xia, Y. Y. *J Electrochem Soc* **2006,** 153, (4), A743-A748.

151. Park, J. H.; Park, O. O.; Shin, K. H.; Jin, C. S.; Kim, J. H. *Electrochem Solid St* **2002,** 5, (2), H7-H10.

152. Yang, G. W.; Xu, C. L.; Li, H. L. *Chem Commun* **2008**, (48), 6537-6539.

153. Lu, Z. Y.; Chang, Z.; Zhu, W.; Sun, X. M. *Chem Commun* **2011,** 47, (34), 9651-9653.

154. Xing, W.; Qiao, S. Z.; Wu, X. Z.; Gao, X. L.; Zhou, J.; Zhuo, S. P.; Hartono, S. B.; Hulicova-Jurcakova, D. *J Power Sources* **2011,** 196, (8), 4123-4127.

155. Delmas, C.; Faure, C.; Borthomieu, Y. *Mat Sci Eng B-Solid* **1992,** 13, (2), 89-96.

156. Su, L. H.; Gong, L. Y.; Gao, J. L. *J Power Sources* **2012,** 209, 141-146.

157. Wang, H.; Xiang, X.; Li, F. *J Mater Chem* **2010,** 20, (19), 3944-3952.

158. Demourguesguerlou, L.; Delmas, C. *J Power Sources* **1993,** 45, (3), 281-289.

159. GuerlouDemourgues, L.; Delmas, C. *J Electrochem Soc* **1996,** 143, (2), 561-566.

160. Salunkhe, R. R.; Jang, K.; Lee, S. W.; Ahn, H. *Rsc Adv* **2012,** 2, (8), 3190-3193.

161. Hu, Z. A.; Xie, Y. L.; Wang, Y. M.; Wu, H. Y.; Yang, Y. Y.; Zhang, Z. Y. *Electrochim Acta* **2009,** 54, (10), 2737-2741.

162. Liu, X. H.; Ma, R. Z.; Bando, Y.; Sasaki, T. *Adv Mater* **2012,** 24, (16), 2148-2153.

163. Yan, T.; Li, Z.; Li, R.; Ning, Q.; Kong, H.; Niu, Y.; Liu, J. *J Mater Chem* **2012,** 22, (22), 23587.

164. Wang, Y. S.; Yang, S. Y.; Li, S. M.; Tien, H. W.; Hsiao, S. T.; Liao, W. H.; Liu, C. H.; Chang, K. H.; Ma, C. C. M.; Hu, C. C. *Electrochim Acta* **2013,** 87, 261-269.

165. Yang, S. Y.; Chang, K. H.; Lee, Y. F.; Ma, C. C. M.; Hu, C. C. *Electrochem Commun* **2010,** 12, (9), 1206-1209.

166. Li, S. M.; Wang, Y. S.; Yang, S. Y.; Liu, C. H.; Chang, K. H.; Tien, H. W.; Wen, N. T.; Ma, C. C. M.; Hu, C. C. *J Power Sources* **2013,** 225, 347-355.

167. Zhong, J. H.; Wang, A. L.; Li, G. R.; Wang, J. W.; Ou, Y. N.; Tong, Y. X. *J Mater Chem* **2012,** 22, (12), 5656-5665.

168. Kamath, P. V.; Dixit, M.; Indira, L.; Shukla, A. K.; Kumar, V. G.; Munichandraiah, N. *J Electrochem Soc* **1994,** 141, (11), 2956-2959.

169. Gupta, V.; Kusahara, T.; Toyama, H.; Gupta, S.; Miura, N. *Electrochem Commun* **2007,** 9, (9), 2315-2319.

170. Moon, I. K.; Lee, J.; Ruoff, R. S.; Lee, H. *Nat Commun* **2010,** 1.

171. Gupta, V.; Gupta, S.; Miura, N. *J Power Sources* **2008,** 175, (1), 680-685.

172. Jiang, H.; Lee, P. S.; Li, C. Z. *Energ Environ Sci* **2013,** 6, (1), 41-53.

173. Cheng, Y. W.; Zhang, H. B.; Lu, S. T.; Varanasi, C. V.; Liu, J. *Nanoscale* **2013,** 5, (5), 1067-1073.

174. Armstrong, R. D.; Charles, E. A. *J Power Sources* **1989,** 25, (2), 89-97.

175. Wu, M. S.; Huang, K. C. *Chem Commun* **2011,** 47, (44), 12122-12124.

176. Hu, C. C.; Chang, K. H.; Lin, M. C.; Wu, Y. T. *Nano Lett* **2006,** 6, (12), 2690-2695.

177. Hu, C. C.; Chang, K. H.; Hsu, T. Y. *J Electrochem Soc* **2008,** 155, (8), F196-F200.

178. Yan, J.; Fan, Z. J.; Sun, W.; Ning, G. Q.; Wei, T.; Zhang, Q.; Zhang, R. F.; Zhi, L. J.; Wei, F. *Adv Funct Mater* **2012,** 22, (12), 2632-2641.

179. Xiao, L. F.; Cao, Y. L.; Xiao, J.; Schwenzer, B.; Engelhard, M. H.; Saraf, L. V.; Nie, Z. M.; Exarhos, G. J.; Liu, J. *Advanced Materials* **2012,** 24, (9), 1176-1181.

180. Bruce, P. G.; Freunberger, S. A.; Hardwick, L. J.; Tarascon, J. M. *Nat Mater* **2012,** 11, (1), 19-29.

181. Wang, B. *J Power Sources* **2005,** 152, (1), 1-15.

182. Gewirth, A. A.; Thorum, M. S. *Inorg Chem* **2010,** 49, (8), 3557-3566.

183. Guo, S. J.; Sun, S. H. *J Am Chem Soc* **2012,** 134, (5), 2492-2495.

184. Zhang, J.; Sasaki, K.; Sutter, E.; Adzic, R. R. *Science* **2007,** 315, (5809), 220-222.

185. Gong, K. P.; Du, F.; Xia, Z. H.; Durstock, M.; Dai, L. M. *Science* **2009,** 323, (5915), 760-764.

186. Liang, Y. Y.; Li, Y. G.; Wang, H. L.; Zhou, J. G.; Wang, J.; Regier, T.; Dai, H. J. *Nat Mater* **2011,** 10, (10), 780-786.

187. Wang, H. L.; Liang, Y. Y.; Li, Y. G.; Dai, H. J. *Angew Chem Int Edit* **2011,** 50, (46), 10969-10972.

188. Sharma, S.; Pollet, B. G. *J Power Sources* **2012,** 208, 96-119.

189. Zhou, Y. K.; Neyerlin, K.; Olson, T. S.; Pylypenko, S.; Bult, J.; Dinh, H. N.; Gennett, T.; Shao, Z. P.; O'Hayre, R. *Energ Environ Sci* **2010,** 3, (10), 1437-1446.

190. Kou, R.; Shao, Y. Y.; Wang, D. H.; Engelhard, M. H.; Kwak, J. H.; Wang, J.; Viswanathan, V. V.; Wang, C. M.; Lin, Y. H.; Wang, Y.; Aksay, I. A.; Liu, J. *Electrochem Commun* **2009,** 11, (5), 954-957.

191. Wang, X.; Li, W. Z.; Chen, Z. W.; Waje, M.; Yan, Y. S. *J Power Sources* **2006,** 158, (1), 154-159.

192. Pan, D.; Ombaba, M.; Zhou, Z. Y.; Liu, Y.; Chen, S. W.; Lu, J. *Acs Nano* **2012,** 6, (12), 10720-10726.

193. Qu, L. T.; Liu, Y.; Baek, J. B.; Dai, L. M. *Acs Nano* **2010,** 4, (3), 1321-1326.

194. Zheng, Y.; Jiao, Y.; Jaroniec, M.; Jin, Y. G.; Qiao, S. Z. *Small* **2012,** 8, (23), 3550-3566.

195. Li, Y. G.; Zhou, W.; Wang, H. L.; Xie, L. M.; Liang, Y. Y.; Wei, F.; Idrobo, J. C.; Pennycook, S. J.; Dai, H. J. *Nat Nanotechnol* **2012,** 7, (6), 394-400.

196. Compton, O. C.; Nguyen, S. T. *Small* **2010,** 6, (6), 711-723.

197. Pumera, M. *Chem Soc Rev* **2010,** 39, (11), 4146-4157.

198. Zhang, L. L.; Xiong, Z. G.; Zhao, X. S. *Acs Nano* **2010,** 4, (11), 7030-7036.

199. Jin, Z. P.; Nie, H. G.; Yang, Z.; Zhang, J.; Liu, Z.; Xu, X. J.; Huang, S. M. *Nanoscale* **2012,** 4, (20), 6455-6460.

200. Parvez, K.; Yang, S. B.; Hernandez, Y.; Winter, A.; Turchanin, A.; Feng, X. L.; Mullen, K. *Acs Nano* **2012,** 6, (11), 9541-9550.

201. Ozkan, T.; Naraghi, M.; Chasiotis, I. *Carbon* **2010,** 48, (1), 239-244.

202. Higginbotham, A. L.; Kosynkin, D. V.; Sinitskii, A.; Sun, Z. Z.; Tour, J. M. *Acs Nano* **2010,** 4, (4), 2059-2069.

203. Park, S.; Ruoff, R. S. *Nat Nanotechnol* **2009,** 4, (4), 217-224.

204. Wang, Z. J.; Zhou, X. Z.; Zhang, J.; Boey, F.; Zhang, H. *J Phys Chem C* **2009,** 113, (32), 14071-14075.

205. Wang, X. C.; Maeda, K.; Thomas, A.; Takanabe, K.; Xin, G.; Carlsson, J. M.; Domen, K.; Antonietti, M. *Nat Mater* **2009,** 8, (1), 76-80.

206. Lai, L. F.; Potts, J. R.; Zhan, D.; Wang, L.; Poh, C. K.; Tang, C. H.; Gong, H.; Shen, Z. X.; Jianyi, L. Y.; Ruoff, R. S. *Energ Environ Sci* **2012,** 5, (7), 7936-7942.

207. Lin, Z. Y.; Song, M. K.; Ding, Y.; Liu, Y.; Liu, M. L.; Wong, C. P. *Phys Chem Chem Phys* **2012,** 14, (10), 3381-3387.

208. Liang, Y. Y.; Wang, H. L.; Diao, P.; Chang, W.; Hong, G. S.; Li, Y. G.; Gong, M.; Xie, L. M.; Zhou, J. G.; Wang, J.; Regier, T. Z.; Wei, F.; Dai, H. J. *J Am Chem Soc* **2012,** 134, (38), 15849-15857.

Biography

Place and Date of Birth

Dongying, Shandong Province, People's Republic of China

Oct. 12th, 1984

Education

2008~2013 Ph.D. (Chemistry)

Duke University, Durham, NC United States

2003~2008 B. S. (Chemistry, Major)

B. Eng. (Chemical Engineering, Major)

Shandong University, Jinan, People's Republic of China

Publications

1. **Cheng, Y.**; Zhang, H.; Varanasi, C. and Liu, J. "Highly Efficient Oxygen Reduction Electrocatalysts based on Winged Carbon Nanotubes" Submitted to ***Scientific Reports***
2. **Cheng, Y**. and Liu, J. "Carbon Nanomaterials for Flexible Energy Storage" ***Material Research Letters***, 2013, 1-18
3. Lu, S.; **Cheng, Y.**; Wu, X. and Liu, J. "Significantly Improved Long-Cycle Stability in High-Rate Li-S Batteries Enabled by Coaxial Graphene Wrapping Over Sulfur-Coated Carbon Nanofibers" ***Nano Letters***, 2013, 13(6), 2485-2489
4. **Cheng, Y.**; Zhang, H. Varanasi, C. and Liu, J. "Co-Ni Double Hydroxide Grown on Graphene as High Performance Supercapacitor Materials" Submitted to ***Energy & Environmental Sciences***
5. **Cheng, Y.**; Zhang, H.; Lu, S.; Varanasi, C. and Liu, J. "Flexible Asymmetric Supercapacitors with High Energy and High Power Density in Aqueous Electrolytes" ***Nanoscale***, 2013, 5, 1067-1973.

6. Aruguete D.; Kim, B.; Hochella M. F.; Ma, Y.; **Cheng, Y.**; Hoegh, A.; Liu, J. and Pruden A. "Antimicrobial nanotechnology: its potential for the effective management of microbial drug resistance and implications for research needs in microbial nanotoxicology" ***Environ. Sci.: Processes Impacts***, 2013, 15, 93-102.
7. Li, B.; **Cheng, Y.;** Liu, J.; Yi, C.; Brown, A.; Yuan, H.; Vol-Dinh, T.; Fisher, M. and Warren, W. "Quantitative Nonlinear Optical Imaging of Graphene Using Shaped Femtosecond Laser Pulses" ***Nano Letters*** 2012, 12(11), 5936-5940
8. Lin, S.; Huang, R.; **Cheng, Y.;** Liu, J.; Lau, B. and Wiesner, M. "Silver Nanoparticle-Alginate Composite Beads for Point-of-Use Drinking Water Disinfection" ***Water Research***, 2013, 47(12), 3959-3965
9. **Cheng, Y**.; Lu, S.; Zhang, H.; Varanasi, C. and Liu, J. "Synergistic Effects from Graphene and Carbon Nanotubes Enable Flexible and Robust Electrodes for High-Performance Supercapacitors" ***Nano Letters,*** 2012, 12(8), 4206-4211
10. Yang, S.; Cai, Y.; **Cheng, Y.**; Varanasi, C. and Liu, J. "Monolithic co-Aerogels of Carbon/Titanium Dioxide as Three Dimensional Nanostructured Electrodes for Energy Storage" ***Journal of Power Sources***, 2012, 218, 140-147
11. **Cheng, Y.;** Zhang, H.; Cordova, I. and Liu, J. "Comparing Graphene and Carbon Nanotubes as Nanoscale Current Collectors in MnO_2-based Supercapacitors" Accepted by ***Journal of Nano Energy and Power Research*** 2012
12. Lin, S.; **Cheng, Y.**, Liu, J. and Wiesner, M. "Polymeric Coatings on Silver Nanoparticles Hinder Autoaggregation but Enhance Attachment to Uncoated Surfaces" ***Langmuir,*** **2012**, *28(9)*, 4178-4186
13. Cho, J.; Lin, Q.; Yang, S.; Simmons, J.; **Cheng, Y.**; Lin, E.; Yang, J.; Foreman, J.; Everitt, H.; Yang, W.; Kim, J. and Liu, J "Sulfur-doped Zinc Oxide (ZnO) Nanostars: Synthesis and Simulation of Growth Mechanism" ***Nano Research***, 2012, *5(1)*: 20~26
14. Ma, R.; Levard, C.; Marinakos, S.; **Cheng, Y.**; Liu, J.; Michel, F.; Brown, G. and Lowry, G. "Size-Controlled Dissolution of Organic-Coated Silver Nanoparticles" ***Environmental Science & Technology*** 2012, *46 (2)*, 752–759
15. Lin, S.; **Cheng, Y.**; Bobcombe, Y.; Jones, K.; Liu, J. and Wiesner, M. "Deposition of Silver Nanoparticles in Geochemically Heterogeneous Porous Media: predicting affinity from surface composition analysis" ***Environmental Science & Technology*** **2011,** *45(12)*, 5209-5215
16. **Cheng, Y.;** Yin, L.; Lin, S.; Wiesner, M.; Bernhardt, E. and Liu, J. "Toxicity Reduction of Polymer-Stablized Silver Nanoparticles Suspensions by Sunlight" ***Journal of Physical Chemistry C*** 2011, *115*, 4425-4432
17. Yin, L.; **Cheng, Y.**; Espinasse, B.; Colman, B.; Auffan, M.; Wiesner, M.; Rose, J.; Liu, J. and Bernhardt, E. "More Than the Ions: The Effects of Silver Nanoparticles on Lolium Multiflorum" ***Environmental Science & Technology*** **2011**, *45*, 2360-2367

18. Hou, Y.; **Cheng, Y.**; Hobson, T. and Liu, J. "Design and Synthesis of Hierarchical MnO_2 Nanospheres/carbon nanotubes/conducting Polymer Ternary Composite for High Performance Electrochemical Electrodes" ***Nano Letter***, 2010, *10*, 2727-2733
19. Feng, Y.; Ju, X.; Feng, W.; Zhang, H.; **Cheng, Y.;** Liu, J.; Fujii, A.; Ozaki, M.; Yoshiho, K. "Organic Solar Cells Using Few-walled Carbon Nanotubes Electrode Controlled by the Balance Between Sheet Resistance and the Transparency", ***Applied Physics Letters*** 2009, 94, 123302

Proceedings

"One-pot Synthesis of Functionalized Few-walled Carbon Nanotubes/MnO_2 Composite for High Performance Electrochemical Supercapacitors, Yingwen Cheng, Jie Liu etc. ***Materials Challenges in Alternative and Renewable Energy*** 2012

Presentations

1. "Flexible and Robust Electrodes for High-performance Supercapacitors Enabled by Synergistic Effects from Graphene and Carbon Nanotubes" MRS Spring Meeting , San Francisco, CA Apr. 2013 (Poster Presentation)
2. "High Performance Supercapacitors Using MnO_2 and Carbon Nanomaterials" CEINT Internal Meeting. Durham, NC Mar. 2012 (Oral Presentation)
3. "Graphene oxide: synthesis, characterization and applications" International Conference on the Environmental Implications of NanoTechnology & EPA Nano Grantees Meetings, Durham, NC May 2011 (Poster Presentation)
4. "Toxicity Reduction of Polymer stabilized silver nanoparticles by sunlight" CEINT Internal Scientific Meeting, Durham, NC Apr. 2010 (Poster Presentation)
5. 'Stability of silver nanoparticles under the irradiation of sunlight.' International Conference on the Environmental Implications of NanoTechnology, Washington, DC Sep. 2009 (Oral Presentation)
6. 'Stability of silver nanoparticles under the irradiation of sunlight' CEINT Brown Bag Lunch Seminar, Duke University, Durham, NC Sep. 2009 (Oral Presentation)